DYNAMICS OF OCEAN CIRCULATION AND AIR-SEA INTERACTION IN THE SOUTHEAST INDIAN OCEAN AND THEIR IMPACT ON NINGALOO NIÑO

A Dissertation

by

XUE FENG

BS, Lanzhou University, 2010
MS, Institute of Oceanology, Chinese Academy of Sciences, 2013

Submitted in Partial Fulfillment of the Requirements for the Degree of

DOCTOR OF PHILOSOPHY

in

COASTAL AND MARINE SYSTEM SCIENCE

Texas A&M University-Corpus Christi
Corpus Christi, Texas

August 2022

August 2022

DYNAMICS OF OCEAN CIRCULATION AND AIR-SEA INTERACTION IN THE SOUTHEAST INDIAN OCEAN AND THEIR IMPACT ON NINGALOO NIÑO

A Dissertation

by

XUE FENG

This dissertation meets the standards for scope and quality of
Texas A&M University-Corpus Christi and is hereby approved.

Toshiaki Shinoda, PhD
Chair

Darek Bogucki, PhD
Committee Member

Chuntao Liu, PhD
Committee Member

Feiqin Xie, PhD
Committee Member

Lei Jin, PhD
Graduate Faculty Representative

August 2022

ABSTRACT

Extreme ocean warmings associated with the Ningaloo Niño have had significant impacts on regional climate and the health of the marine ecosystem in the Southeast Indian Ocean. The generation and development of the Ningaloo Niño are caused by a combination of atmospheric forcing and oceanic processes, including air-sea heat fluxes and the heat transport associated with the Leeuwin Current (LC). In addition, the large-scale climate variability in the tropics can also affect the Ningaloo Niño via atmosphere and ocean teleconnections. In this dissertation, the variability of the Southeast Indian Ocean, including the air-sea flux and LC variability, is investigated systematically using observations, reanalysis, and numerical model experiments to advance our understanding of the driving mechanism of the Ningaloo Niño. Firstly, the air-sea heat flux variability during the Ningaloo Niño is analyzed using six major air-sea heat flux datasets. One of the major sources of uncertainties in the latent heat flux climatology is the bulk flux algorithm. Over the life cycle of Ningaloo Niño, the anomalous latent heat flux is dominant in the net surface heat flux variations, and the uncertainties in latent heat flux anomaly largely depend on the phase of the Ningaloo Niño. During the developing and peak phase, the contribution of air-sea heat flux to the surface warming has large uncertainties, which are primarily caused by the differences in the sea surface temperature. However, during the decay phase, large negative latent heat flux anomalies (cooling the ocean) are found in all datasets, indicating the important role of latent heat flux in damping anomalous warming during the recovery phase. Secondly, the sensitivity of model resolution on the climatology and variability of the LC is evaluated in an eddy-permitting and eddy-resolving Ocean General Circulation Model (OGCM). The magnitude and structure of the mean LC are more realistic in the high-

resolution (eddy-resolving, 1/12°) OGCM experiment. During the 2010-2011 Ningaloo Niño, the high-resolution experiment simulates a stronger LC, which leads to a warmer ocean temperature off the west coast of Australia. Lastly, the effect of the continental shelf and slope on the LC and Ningaloo Niño are investigated using a series of high-resolution Indo-Pacific OGCM experiments. The "*control*" experiment uses a realistic bottom topography along the west coast of Australia, whereas the sensitivity ("*no-shelf*") experiment uses a modified topography with no continental shelf and slope near the coast. The LC in the *no-shelf* experiment is located closer to the coast, and the strength is decreased by about 28% compared to the control experiment. During the 2010-2011 Ningaloo Niño, stronger enhancements of the LC are detected in the *control* experiment, which lead to a 26% increase in the upper 50 m ocean temperature. The analysis of ocean dynamical processes indicates that the shelf-slope topography can effectively trap the positive sea level anomaly at the coast and suppress the Rossby wave radiation from the coast, thereby maintaining a stronger LC.

ACKNOWLEDGEMENTS

First of all, I would like to thank my advisor Dr. Toshiaki Shinoda for the guidance and support. He offered great help with my initial application for the PhD program and shared his insights and expertise with me over the past several years. Our regular meetings were always productive, during which he provided concrete feedback on my research. I am also grateful for his help with ocean modeling and scientific writing.

In addition, I would like to thank my advising committee Dr. Darek Bogucki, Dr. Chuntao Liu, and Dr. Feiqin Xie for their valuable comments and suggestions to improve the quality of this dissertation. And special thanks to Dr. Weiqing Han for the collaboration and helpful discussions on Chapter 4.

I would also like to thank all my colleagues at TAMUCC for making this journey enjoyable. In particular, thanks are due to Dr. Yanjuan Guo, Dr. Suyang Pei, and Mariana C. Nieva Tamasiunas for helping me refine my problem-solving and research management skills.

Finally, I would like to thank my parents, who give me the freedom to pursue my goal on the other side of the planet from where they live. I know it was hard for them, particularly during the past two years. And to my sister's family: thank you all for being a great source of support and encouragement.

This research was supported by NSF grant OCE-1658218, NASA grant NNX17AH25G, NOAA grants NA15OAR431074 and NA17OAR4310256, and DOD Grant W911NF-20-1-0309. Computing resources were provided by the Climate Simulation Laboratory at NCAR's Computational and Information Systems Laboratory, sponsored by NSF, and the HPC systems at the Texas A&M University, College Station and Corpus Christi.

TABLE OF CONTENTS

Page

LIST OF FIGURES

Page

LIST OF TABLES

Page

CHAPTER I: INTRODUCTION

The southeast Indian Ocean (SEIO) experienced a rapid warming during the past decades (Han et al. 2014). Overlaid with the warming trend, the region is also strongly affected by prolonged marine heatwave events (Pearce et al. 2011). In the austral summer of 2011, an extreme marine heatwave occurred off the west coast of Australia. In February 2011, the monthly mean sea surface temperature (SST) anomaly exceeded 3°C for a vast area offshore of Western Australia, and the peak SST anomaly in some areas reached 5°C (Feng et al. 2013). After the occurrence of the extreme 2011 marine heatwave event, historical warming (cooling) events that are phase-locked to austral summer are detected in the SEIO (e.g., Marshall et al. 2015; Kataoka et al. 2014; Feng et al. 2015). Such interannual variability associated with the warm/cold events is dubbed "Ningaloo Niño/Niña" and is identified as the major climate variability in the SEIO (Feng et al. 2013; Kataoka et al. 2017; Zhang et al. 2018). During the Ningaloo Niño years, the warm sea surface temperature (SST) has caused excessive rainfall over Australia (Kataoka et al. 2014; Tozuka et al. 2014) and severe impacts on the coastal marine ecosystem (Pearce and Feng 2013; Wernberg et al. 2013; Caputi et al. 2014). Because of the significant environmental and economic impacts of the Ningaloo Niño, the climate research community has been paying increasing attention to the accurate prediction of Ningaloo Niño in recent years. Accordingly, understanding the physical mechanism of the Ningaloo Niño is important for the further improvement of its prediction by climate models. Since the primary driver of the 2010-2011 Ningaloo Niño event is the anomalous heat transport produced by the strong Leeuwin Current (Feng et al. 2013; Benthuysen et al. 2014a; Marshall et al. 2015), the characteristics, variability, and dynamics of Leeuwin Current are first described in the following

sections. Then the recent progress in understanding the Ningaloo Niño is discussed. Finally, the objectives of the study described in this dissertation are presented.

1.1 The Leeuwin Current

The SEIO circulation is dominated by the near-surface poleward Leeuwin Current and the deeper equatorward Leeuwin Undercurrent (Thompson 1984; Smith et al. 1991). The Leeuwin Current flows southward along the shelf break of the western Australian coast (22-34°S) with a depth of approximately 200-300 m, against the prevailing southerly wind direction. The formation mechanism of the Leeuwin Current is the large-scale meridional buoyancy gradient, which is manifested by the poleward decrease of surface dynamic height (e.g., Godfrey and Ridgway 1985). The buoyancy gradient also drives eastward geostrophic currents in the interior south Indian Ocean, which merge into the Leeuwin Current upon reaching the Australian coast, overcoming the upwelling caused by the southerly wind, and becoming an important subtropical source of the Leeuwin Current (Weaver and Middleton 1989, 1990; Furue et al. 2017). Besides the subtropical source, the Leeuwin Current has a tropical origin with fresh and warm water primarily from the tropical inflows including the Indonesian Throughflow (ITF) and Eastern Gyre Current (EGC) (Domingues et al. 2007).

The Leeuwin Current has a prominent seasonal cycle, with its volume transport largest in austral autumn/winter and smallest in austral summer (Smith et al 1991; Feng et al. 2003; Furue et al. 2017). On the interannual timescale, the LC is influenced by the large-scale climate variability in the equatorial Pacific Ocean. In particular, interannual signals associated with ENSO could propagate along the west coast of Australia and modulate the strength of the Leeuwin Current. During La Niña years, the sea level near the coast is higher than normal and the Leeuwin Current is stronger due to the large cross-shore pressure gradient. At 32°S, the mean

Leeuwin Current transport during La Niña years is 4.2 Sv, and during El Niño years the transport drops to 3.0 Sv (Feng et al. 2003).

Feng et al. (2003) demonstrated that both the annual and interannual variability of the Leeuwin Current is coastally trapped. However, Rossby waves can be generated equatorward of the critical latitudes and the westward propagation of Rossby waves could radiate the high coastal sea level offshore, thus prohibiting the existence of a strong Leeuwin Current. McCreary et al. (1986) and Kundu and McCreary (1986) suggest that the vertical mixing could damp the Rossby waves, and a large mixing coefficient is necessary for the existence of the Leeuwin Current in their analytical model. By including an idealized shelf profile in the analytical model, Weaver and Middleton (1989, 1990) demonstrated that the sloping bottom topography provides a trapping mechanism for the strong Leeuwin Current by suppressing the Rossby wave radiation, and thus the Leeuwin Current can develop without strong vertical mixing. More recently, Furue et al. (2013) and Benthuysen et al. (2014b) examined the influence of the continental shelf and slope on the Leeuwin Current by using an improved analytical model and an idealized numerical model. They concluded that the topographic beta effect plays a key role in the Leeuwin Current dynamics and the existence of a continental shelf-slope is important for generating a realistic Leeuwin Current. However, because their model used simplified shelf profiles and idealized atmosphere forcing, the influence of the topography on the observed Leeuwin Current strength and variability remains unclear.

1.2 Mechanisms of Ningaloo Niño development

The extreme ocean warming during the summer of 2011 is primarily caused by the anomalous heat advection of the Leeuwin Current, which transports warm tropical water southward along the Western Australian coast. The 2010-2011 Ningaloo Niño also co-occurred

with the strongest La Niña in the past century. The Leeuwin Current during this event also has the strongest transport in the historical record (Feng et al. 2013; Benthuysen et al. 2014a; Zinke et al. 2015). Previous studies showed that the easterly wind anomalies in the Pacific associated with the 2010-2011 La Niña affect the Leeuwin Current through oceanic and atmospheric teleconnections (e.g., Tozuka et al. 2014; Kataoka et al. 2014; Zhang et al. 2018; Zhang and Han 2018; Kusunoki et al. 2020). For example, negative surface pressure anomalies in response to Pacific forcing are observed in the southeast IO. As a result, the cyclonic wind anomalies associated with the low-pressure system reduce the southerly wind in the coastal region and thus enhance the Leeuwin Current. On the other hand, Fremantle Sea Level anomalies, which is a proxy of Leeuwin Current strength, are highly correlated with the sea level and easterly wind anomalies in the tropical western Pacific at a lag of one month, revealing the important role of remote forcing on the Leeuwin Current through oceanic teleconnection.

The Ningaloo Niño could also develop during El Niño years, indicating that the intrinsic air-sea feedback processes in the southeast Indian Ocean are also important (Kataoka et al 2018). In the coastal regions, the initial SST anomaly forces northerly wind anomalies along the coast (Matsuno-Gill type response). The reduction of southerly wind could enhance the Leeuwin Current and reduce evaporative cooling, thereby further enhancing the SST warming (Kataoka et al. 2014, 2018).

The contribution of surface heat fluxes during the developing and peak phase of the Ningaloo Niño varies substantially between different studies. For example, Benthuysen et al. (2014a) indicated that reduced latent and sensible heat fluxes around the peak phase account for 1/3 of the warming during the 2010-2011 event in addition to the heat advection produced by the strengthening of Leeuwin Current. On the other hand, a composite analysis of multiple Ningaloo

Niño events indicated that the initial offshore warming is primarily caused by anomalous latent heat flux (Marshall et al., 2015). Recently, Kataoka et al. (2017) calculated the mixed layer temperature balance associated with Ningaloo Niño events and indicated the significant role of shortwave radiation due to the warming produced by the climatological surface heat flux enhanced by the shallow mixed-layer depth (MLD) anomaly during the onset. Moreover, Xu et al. (2018) compared the difference in SST warming patterns between the 2012-2013 event with the 2010-2011 event and found that the difference in the relative importance of surface heat fluxes and heat advection between the two events is mostly responsible for the different spatial distribution of the warming. The different conclusions could partly be due to the different sources of surface heat flux datasets, which include various satellite observations, reanalysis products, and model simulations. It is therefore imperative to systematically analyze the air-sea heat flux variability associated with the Ningaloo Niño using multiple datasets and determine the uncertainties on the role of air-sea heat fluxes.

In contrast to the uncertainties on the role of air-sea heat fluxes, most of the Ningaloo Niño events are accompanied by an enhanced Leeuwin Current, especially during the peak phase of Ningaloo Niño. Although the important role of the local and remote forcing in the development of anomalous ocean warming has been demonstrated in previous studies, the physical and dynamical processes responsible for the enhancement of the Leeuwin Current are still unclear. Besides, many modeling studies of the Ningaloo Niño rely on the low-resolution ocean model which cannot adequately resolve the Leeuwin Current. Godfrey and Weaver (1991) demonstrated that the horizontal resolution of the model could influence the modeled Leeuwin Current strength, and the current becomes stronger with the increased resolution. A recent modeling study also highlighted a realistic Leeuwin Current simulated in the high-resolution

ocean general circulation model (OGCM) (Furue 2019). Thus, it is necessary to assess the sensitivity of the simulated Leeuwin Current variability and the associated SST variations to the model resolution. The use of a high-resolution OGCM will also allow us to examine the key oceanic processes during the Ningaloo Niño, and thus further improve our understanding of the driving mechanisms of the Ningaloo Niño.

1.3 Objectives and Outline

This study aims to improve our understanding of the generation and decay mechanisms of the Ningaloo Niño through the analysis of observational datasets, reanalysis, and a series of numerical model experiments.

Specific objectives in this study are:

- To determine the role of air-sea heat fluxes during the life cycle of the Ningaloo Niño
- To identify the uncertainties of the air-sea heat fluxes from multiple datasets and determine the source of uncertainties
- To determine the model resolution on the simulated climatology and variability of the Leeuwin Current
- To quantify the effect of topography on the Leeuwin Current and the Ningaloo Niño

The results of the dissertation research are organized into three chapters. Chapter 2 describes the air-sea heat flux variability in the SEIO using six major air-sea heat flux products. A composite analysis is conducted to investigate the role of air-sea heat flux in different phases of the Ningaloo Niño and the sensitivity calculation using the COARE3.5 bulk algorithm is carried out to identify the major source of the uncertainties in the latent heat flux. Chapter 3 provides the climatology, seasonal and interannual variability of the Leeuwin Current simulated by an eddy-permitting and eddy-resolving Indo-Pacific basin OGCM. The degree to which the

model resolution affects the simulated Leeuwin Current and SST is demonstrated. Chapter 4 uses a set of eddy-resolving Indo-Pacific basin OGCM to isolate and quantify the effect of the continental shelf and slope on the Leeuwin Current and Ningaloo Niño. Finally, Chapter 5 provides a summary of the key results of this dissertation research.

CHAPTER II: AIR-SEA HEAT FLUX VARIABILITY IN THE SOUTHEAST INDIAN OCEAN AND ITS RELATION WITH NINGALOO NIÑO

2.1 Introduction

The southeast Indian Ocean (IO) is a region where extreme climate variability and unique ocean circulation are observed. During 2010-2011, an extreme marine heatwave associated with ocean warming occurred off the west coast of Australia. This extreme warming event is termed "Ningaloo Niño" (Feng et al. 2013). The 2010-2011 Ningaloo Niño event was associated with anomalous ocean circulations in the southeast IO. For example, there was an unseasonable surge of the Leeuwin Current, which flows southward against prevailing southerly winds along the west coast of Australia, bringing warm waters from the tropics. These extreme oceanic conditions have a substantial impact on the marine ecosystem and regional climate variability (Pearce and Feng 2013; Wernberg et al. 2013; Caputi et al. 2014; Kataoka et al. 2014; Tozuka et al. 2014).

In the southeast IO near the west coast of Australia, relatively large annual mean surface heat fluxes (cooling the ocean) with the strong seasonal cycle are observed (Feng et al. 2003, 2008). For the annual mean, a large amount of heat loss of the ocean occurs at the air-sea interface in a broad area off the west coast of Australia. The majority of the heat loss is caused by a large evaporative cooling due to warm SSTs in the region of the Leeuwin Current. The annual cycle of net surface heat flux is dominated by shortwave radiation and latent heat flux. During the austral winter, shortwave radiation is weak, but the latent heat flux (cooling) is large due to a stronger Leeuwin Current (and thus warm SSTs) and low near-surface specific humidity associated with the cold air temperature. During the austral summer, shortwave radiation is

strong, and the latent heat flux is small due to a weaker Leeuwin Current (Feng et al., 2003, 2008) and higher near-surface specific humidity associated with the warmer air temperature.

In addition to the strong seasonal cycle of air-sea heat fluxes, significant interannual variations of surface heat fluxes are found in this region including those associated with the Ningaloo Niño. Some of the previous studies suggest that the SST warming during the Ningaloo Niño is caused by the heat advection by the strengthening of the Leeuwin Current especially for the 2010-2011 event, whereas air-sea heat fluxes also contribute to the warming (Feng et al. 2013; Zhang et al. 2018). However, the relative importance of heat advection by the Leeuwin Current and surface heat fluxes on the development of the Ningaloo Niño varies substantially between different studies. For example, Benthuysen et al. (2014a) indicated that reduced latent and sensible heat fluxes around the peak phase account for 1/3 of the warming during the 2010/2011 event in addition to the heat advection produced by the strengthening of Leeuwin Current. On the other hand, a composite analysis of multiple Ningaloo Niño events indicated that the initial offshore warming is primarily caused by the anomalous latent heat flux (Marshall et al. 2015). Kataoka et al. (2014) classified the Ningaloo Niño into locally and non-locally amplified modes based on the local wind anomalies and suggested that the reduction of latent heat flux enhances offshore warming during the development and coastal warming during the peak in both modes. Recently, Kataoka et al. (2017) calculated the mixed layer temperature balance associated with Ningaloo Niño events and found that shortwave radiation contributes to the coastal warming in both locally and non-locally amplified modes due to the warming produced by the climatological surface heat flux enhanced by the shallow mixed-layer depth (MLD) anomaly during the onset. Moreover, Xu et al. (2018) compared the difference in SST warming patterns between the 2012/2013 event with the 2010/2011 event and found that the difference in

the relative importance of surface heat fluxes and heat advection between the two events is mostly responsible for the different spatial distribution of the warming.

As described above, a variety of different conclusions on the role of surface heat fluxes in the warming during the Ningaloo Niño have been obtained in previous studies. These differences could partly be due to the different sources of surface flux datasets, which include various satellite observations, reanalysis products, and model simulations. The systematic analysis of air-sea heat flux variability associated with the Ningaloo Niño using multiple datasets is thus necessary to reconcile previous studies and determine the uncertainties on the role of air-sea fluxes.

While most of the previous studies focus on processes during the onset and development (warming period) of the Ningaloo Niño, processes that control the cooling during the recovery phase have received little attention. A recent study by Kataoka et al. (2017) discussed processes during both the development and demise of the Ningaloo Niño and suggested that the mixed layer temperature is influenced by not only heat flux anomalies but also MLD anomalies which change the heat capacity. They concluded that the net effect of latent heat flux is not as important as earlier studies suggested during the recovery phase because of the anomalously deep mixed layers and thus a large heat capacity. In addition, the significant role of sensible heat flux for the locally-amplified mode is suggested. However, these conclusions are based on the analysis of a single numerical model simulation, and it is possible that different results could be obtained using different datasets. Accordingly, it is necessary to examine the processes during the recovery phase using multiple datasets, and such analyses will provide better insights into the role of air-sea fluxes during the recovery phase.

In addition to the large influence of surface heat fluxes on SST and the upper ocean during the Ningaloo Niño, air-sea heat fluxes influence the atmospheric conditions and the large-scale atmospheric circulations, and in turn they can feedback on SSTs. Various feedback mechanisms between the atmosphere and ocean associated with the Ningaloo Niño have been suggested in recent years. For example, Tozuka and Oettli (2018) showed that during the Ningaloo Niño, positive SST anomalies increase the formation of clouds and thus decrease the shortwave radiation, which could weaken the initial warming. Zhang and Han (2018) found that SST anomalies in the southeast IO associated with the Ningaloo Niño lead to the enhancement of western Pacific trade winds and the cooling in the central Pacific. The enhanced trade winds could strengthen the ITF and the cooling anomalies in the central Pacific could induce cyclonic wind anomalies in the southeast IO, both of which would amplify the initial warming of Ningaloo Niño. As changes in air-sea fluxes in the southeast IO are essential components of these feedback mechanisms, assessing the uncertainties of surface fluxes using multiple datasets is necessary for further exploring these air-sea interaction processes.

The uncertainties of air-sea heat fluxes arise from the errors in bulk atmospheric variables and SST, which are derived from reanalysis products and satellite observations, and the use of different bulk flux algorithms (Brunke et al. 2002; Wu et al. 2006; Kubota et al. 2008; Valdivieso et al. 2017). In the area off the west coast of Australia, the uncertainties and thus the difference between the datasets could be very large because of the large variability of SST and associated atmospheric variables caused by Leeuwin Current variations. Hence a thorough description of air-sea fluxes in this region using multiple datasets and their comparisons are crucial for the investigation of climate variability in this region including the Ningaloo Niño.

The purpose of this study is to investigate the air-sea heat fluxes associated with the development and decay of Ningaloo Niño and to identify the major sources of uncertainties in the interannual variability using multiple datasets. In particular, the air-sea heat flux variations during the decay phase of the Ningaloo Niño are emphasized. The rest of this paper is organized as follows. Section 2.2 describes the data and method used in this study. In Section 2.3, climatological air-sea fluxes from different datasets are compared, and the effect of latent heat flux variability on the Ningaloo Niño is studied based on the composite analysis. A discussion and summary are presented in Sections 2.4 and 2.5.

2.2 Data and method

2.2.1 Reanalysis

Daily short and longwave radiation, latent and sensible heat fluxes from five major reanalysis products are used in this study. These are the National Center for Environmental Prediction-National Centers for Atmospheric Research (NCEP/NCAR) reanalysis-1 (NCEP1; Kalnay et al. 1996), the NCEP-Department of Energy (NCEP/DOE) reanalysis (NCEP2; Kanamitsu et al. 2002), the European Centre for Medium-Range Weather Forecasts (ECMWF) Interim reanalysis (ERA-Interim; Dee et al. 2011), NASA's Modern-Era Retrospective analysis for Research and Applications, Version 2 reanalysis (MERRA-2; Gelaro et al. 2017), and NCEP Climate Forecast System Reanalysis (CFSR; Saha et al. 2014, 2010). NCEP1 and NCEP2 are available on the T62 Gaussian grid with a spatial resolution of about 1.875°×1.875°. CFSR reanalysis is based on a coupled ocean-atmosphere-land data assimilation system that consists of an atmospheric component at a resolution of T382 (38 km) and an ocean component at a resolution of 0.5° beyond the tropics. ERA-Interim data is on 0.75°×0.75° grid, and MERRA2 uses an approximate resolution of 0.5°×0.625°. The data for the period 1985-2016 are analyzed

during which all these datasets are available. To investigate the effect of MLD variation on SSTs (Kataoka et al. 2017), MLD obtained from 1/12° Hybrid Coordinate Ocean Model (HYCOM) reanalysis (Metzger et al. 2014) for 1994-2015 is used.

2.2.2 OAFlux

We also used daily gridded (1°×1°) bulk flux state variables (i.e. wind speed, air and sea surface temperature, and humidity) from WHOI Objectively Analyzed Ocean-Atmosphere Flux (OAFlux) product (Yu et al. 2008) to calculate the latent heat flux using the state-of-the-art COARE3.5 bulk algorithm (Fairall et al. 2003). The state variables provided by OAFlux blended observational and reanalysis data from various sources based on an objective analysis to obtain an optimal estimate of the atmospheric and oceanic conditions. The daily state variables for the period 1985-2016 are used in the analysis. The latent heat flux estimates calculated here are well correlated with those from the gridded flux provided by OAFlux (r = 0.997) but have a Root Mean Square Error (RMSE) of 7.8 W m^{-2}. This difference is primarily caused by the lack of SST correction associated with the cool skin and warm layer in our calculation, and the difference due to the use of different versions of bulk formula (COARE3.5 and COARE3.0) is very small (RMSE:0.6 W m^{-2}). Note that the RMSE between latent heat flux estimates using COARE3.5 and those provided by OAFlux is much smaller (2.1 W m^{-2}) during DJF when Ningaloo Niño develops, and thus the effect of the cool skin and warm layer is very small during this season.

2.2.3 Satellite and buoy observations

Monthly satellite-derived radiation fluxes from Clouds and Earth's Radiant Energy Systems (CERES; Kato et al., 2018) for the period 2000-2016 are used. Surface fluxes and bulk flux state variables from the Research Moored Array for African-Asian-Australian Monsoon Analysis and Prediction (RAMA) at 25°S, 100°E (McPhaden et al. 2009) from September 2012

to 2014 are also used for the comparison with gridded flux data products. Note the surface air-sea fluxes from RAMA are estimated using COARE3.0b.

Besides flux datasets, we also use daily high-resolution SST products obtained from National Oceanic and Atmospheric Administration (NOAA) Optimum Interpolation Sea Surface Temperature based on Advanced Very High Resolution Radiometer (AVHRR) observations (OISST; Banzon et al., 2016; Reynolds et al., 2007; 0.25°×0.25°; 1985-2016) and Multi-scale Ultra-high Resolution (MUR) Sea Surface Temperature (SST) analysis produced at Jet Propulsion Laboratory (Chin et al., 2017; 0.01°×0.01°; 2002-2016).

2.3 Results

2.3.1 Climatology

Before examining the air-sea flux variations associated with the Ningaloo Niño, climatological air-sea fluxes over the box region (110°E-116°E, 22°S-32°S) and their uncertainties are investigated by comparing those from different datasets (Figure 2.1a, Table 2.1). The daily products as listed in Section 2.2 are averaged monthly to get the monthly climatological data. The seasonal cycle of latent heat flux from all products is similar, in which large (small) latent heat release in the austral winter (summer) is found. However, remarkable quantitative differences are found especially in summer (Figure 2.1a), during which the maximum difference can be as large as ~80 W m^{-2}.

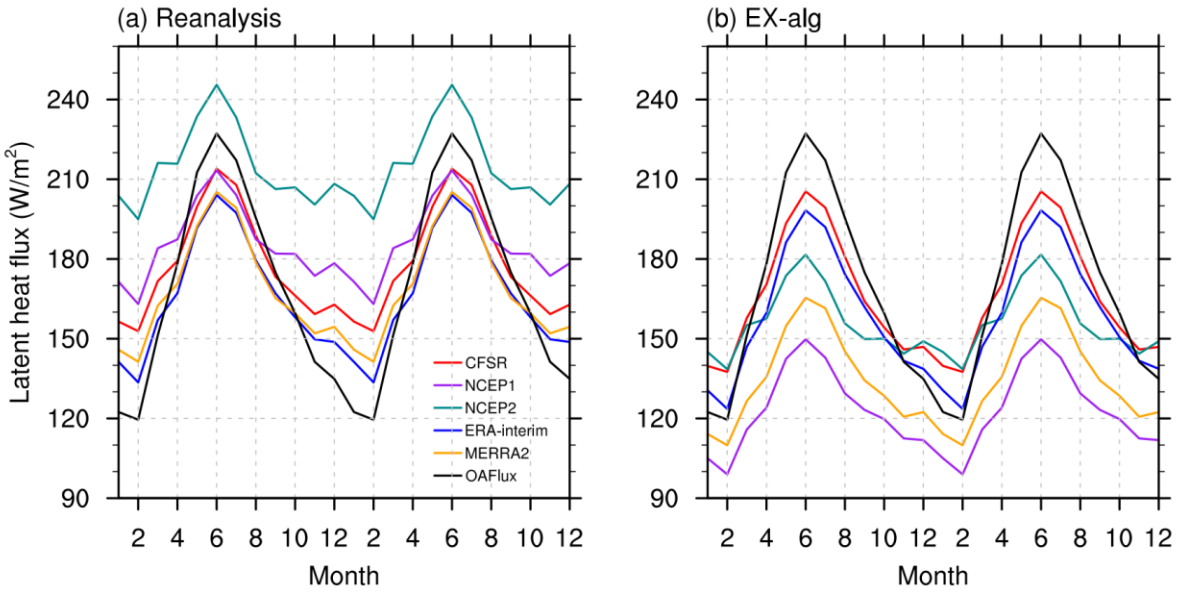

Figure 2.1. Climatological seasonal cycle of latent heat flux calculated for the area around the west coast of Australia (110°E-116°E, 22°S-32°S) from (a) reanalysis products, (b) sensitivity calculations using COARE3.5 algorithm (EX-alg). Positive values indicate the flux from the ocean to the atmosphere.

To further quantify the uncertainties, mean absolute deviation (MAD) defined as $MAD = \frac{\sum_{i=1}^{n} |X_i - \bar{X}|}{n}$, where X_i is surface heat flux from reanalysis, $\bar{X}$ is the mean value of all datasets, and n is the number of datasets, is calculated (Table 2.1, first row). Since MAD measures the magnitude of inter-data spread, the difference in uncertainties between the datasets could be determined quantitatively by calculating MAD. While large uncertainties are found in all seasons, the uncertainty is particularly large during summer with the MAD of 19.4 W m^{-2} when the difference between the highest and lowest latent heat flux exceeds 80 W m^{-2}.

Table 2.1. Mean absolute deviation of annual and seasonal mean latent heat flux calculated from reanalysis, EX-alg, EX-wspd, EX-sst, EX-qa. Units are in W m^{-2}.

	Annual mean	DJF	MAM	JJA	SON
reanalysis	13.3	19.4	13.0	10.2	14.0
EX-alg	15.0	11.7	16.5	21.5	13.4
EX-wspd	7.7	6.0	8.6	10.1	6.7
EX-sst	1.5	1.3	1.6	2.2	1.1
EX-qa	9.3	9.0	9.9	11.8	9.4

Uncertainties of latent heat fluxes could partly be due to the use of different bulk flux algorithms. To evaluate the uncertainties caused by the use of different bulk flux algorithms, we recalculated the daily latent heat flux by using the COARE3.5 flux algorithm and the state variables from each reanalysis product with daily temporal resolution (referred to as EX-alg, where "EX" and "alg" stand for "experiment" and "algorithm"). Figure 2.1b shows the climatological seasonal cycle of latent heat flux from EX-alg. The difference between the values in Figure 2.1b and Figure 2.1a is a measure of uncertainty caused by the use of different algorithms. Based on the comparison, the algorithms used in reanalysis products tend to produce higher values than COARE3.5. For example, the difference is ~60 W m^{-2} for NCEP1 and NCEP2, ~30 W m^{-2} for MERRA2, and ~10 W m^{-2} for ERA-Interim and CFSR. Higher values of latent heat flux in reanalysis data have been documented in previous studies at various locations (e.g., Kubota et al., 2008; Zhang et al., 2016). For example, Kubota et al. (2008) evaluated the latent heat flux from NCEP1 and NCEP2 by comparing with the measurement at the Kuroshio Extension Observatory site. Both datasets overestimated the latent heat flux with a bias of 41 W m^{-2} and 62 W m^{-2}. They suggest that this bias is primarily caused by the use of different algorithms. The major difference between bulk flux algorithms is how the transfer coefficients vary with wind speeds, atmospheric stability, and other physical processes that influence the

transfer of heat and moisture at the sea surface. Yet the further details of why the algorithms used in reanalysis tend to produce higher values are still unknown. The MAD of algorithm-caused uncertainty is 21.3, 25.0, 26.0, and 22.5 W m^{-2} during DJF, MAM, JJA, and SON, respectively, showing a weak seasonal variation. This is because the uncertainty depends on both the magnitude of latent heat flux (larger in winter) and wind speed (smaller in winter). Further details of the seasonal dependence are discussed in the appendix.

The shortwave radiation also reveals a strong seasonal variation (Figure 2.2b). Similar to latent heat flux, large uncertainties are found in summer. Assuming the satellite derived estimate (CERES) is more accurate than reanalysis products, the estimate of NCEP1 has the largest bias (~80 W m^{-2}) in summer and estimates in other datasets have smaller biases of ~20 W m^{-2}. Shortwave radiation and latent heat flux are dominant components of the seasonal variations of net surface heat flux. Considerable net surface heat flux differences between the datasets are found during summer when the Ningaloo Niño develops (Figure 2.2a). Most of the differences arise from latent heat flux and shortwave radiation as discussed above. The contribution of the difference in longwave radiation and sensible heat flux between the different datasets is minimal.

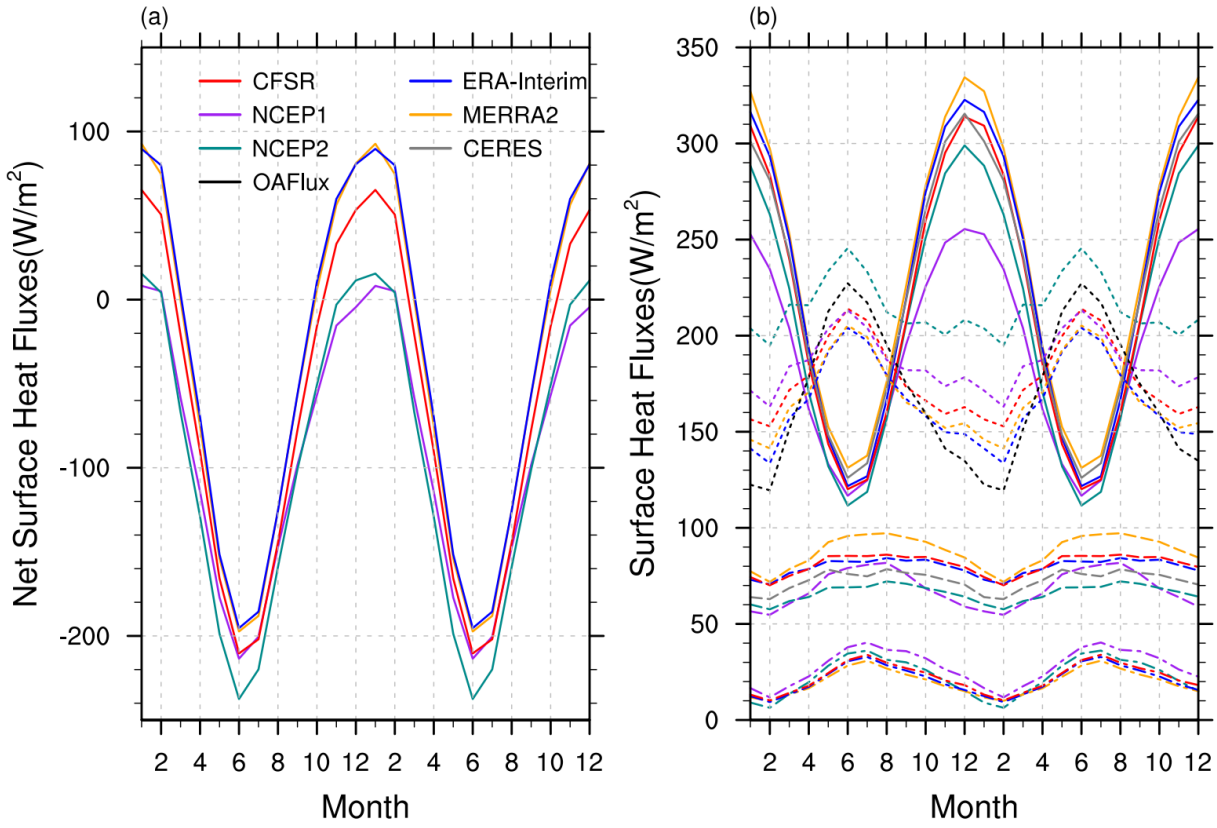

Figure 2.2. (a) Climatological seasonal cycle of the net surface heat flux calculated for the area around the west coast of Australia (110°E-116°E, 22°S-32°S). (b) Same as in (a), but for net shortwave radiation (solid line), net longwave radiation (dashed line), latent heat flux (dotted line) and sensible heat flux (dot-dashed line). Colors indicate different datasets. Positive values indicate the flux into the ocean (atmosphere) for net surface heat flux and shortwave radiation (longwave radiation, latent and sensible heat flux).

Figure 2.3 compares the monthly surface heat flux from reanalysis products with the RAMA buoy at 100°E, 25°S for the two-year period during which buoy measurements are available. The variations of latent heat flux from OAFlux and shortwave radiation from CERES agree well with those from the RAMA buoy. Large differences in shortwave radiation between

the datasets are found during the austral summer. Both NCEP1 and CFSR greatly underestimate the net shortwave radiation. The seasonal variations of latent and sensible heat flux at the buoy site are weaker, and the mean value is smaller than those near the west coast of Australia due to the weaker influence of the Leeuwin Current at this location. An overestimate of 10-50 W m^{-2} in latent heat flux from reanalysis products is found throughout the analysis period, suggesting that these differences are partly due to the use of different bulk flux algorithms. The use of COARE3.5 improves the latent heat flux for most of the datasets (Figure 2.4a). MAD decreases from 11.5 to 7.5 W m^{-2} for CFSR, 25.3 to 13.7 W m^{-2} for NCEP2, 24.7 to 23.4 W m^{-2} for ERA-Interim, and 15.9 to 13.2 W m^{-2} for MERRA2, but it increases from 17.7 to 28.2 W m^{-2} for NCEP1 due to large errors in the specific humidity and wind speed (Figure 2.4b and c).

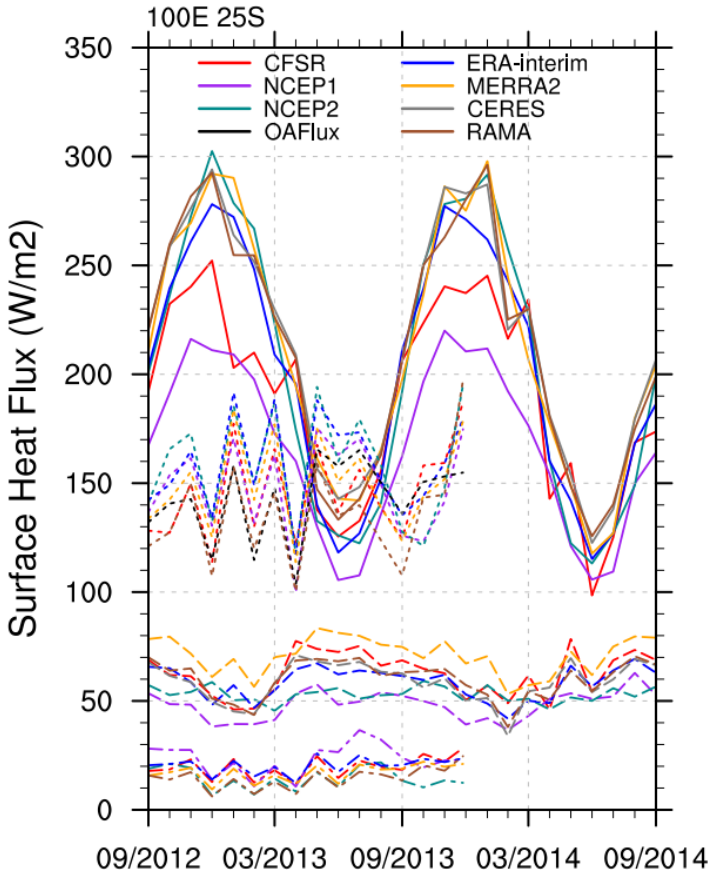

Figure 2.3. Comparison of monthly mean surface heat fluxes from reanalysis products with those from RAMA buoy observations at 100°E, 25°S: net shortwave radiation (solid line), net longwave radiation (dashed line), latent heat flux (dotted line), and sensible heat flux (dot-dashed line). Positive values indicate the flux into the ocean (atmosphere) for shortwave radiation (longwave radiation, latent and sensible heat flux).

While the use of different bulk flux algorithms causes significant differences in estimated fluxes, large differences still exist when using the same algorithm (Figure 2.1b, Figure 2.4a), indicating that the difference in bulk variables largely influences the estimates of latent heat flux. To evaluate the uncertainties caused by each bulk variable, we calculated the daily latent heat flux using COARE3.5 for three different cases, in which bulk variables are (1) surface wind

speed only from each reanalysis and other variables from OAFlux (EX-wspd), (2) SST only from each reanalysis and other variables from OAFlux (EX-sst), (3) air humidity only from each reanalysis and other variables from OAFlux (EX-qa). The uncertainties caused only by windspeed, SST and air humidity can be estimated from EX-wspd, EX-sst, and EX-qa, respectively. Both surface wind speed and humidity largely contribute to the difference between the datasets, whereas the contribution of SST is much smaller (Figure 2.5). The MAD of annual mean latent flux is 7.7 W m^{-2} and 9.3 W m^{-2} for EX-wspd and EX-qa, and that of EX-sst is 1.5 W m^{-2} (Table 2.1). All latent heat fluxes calculated with reanalysis state variables are underestimated in EX-wspd and EX-qa during winter, but not during summer. The MAD during winter is also larger than in summer in EX-wspd and EX-qa.

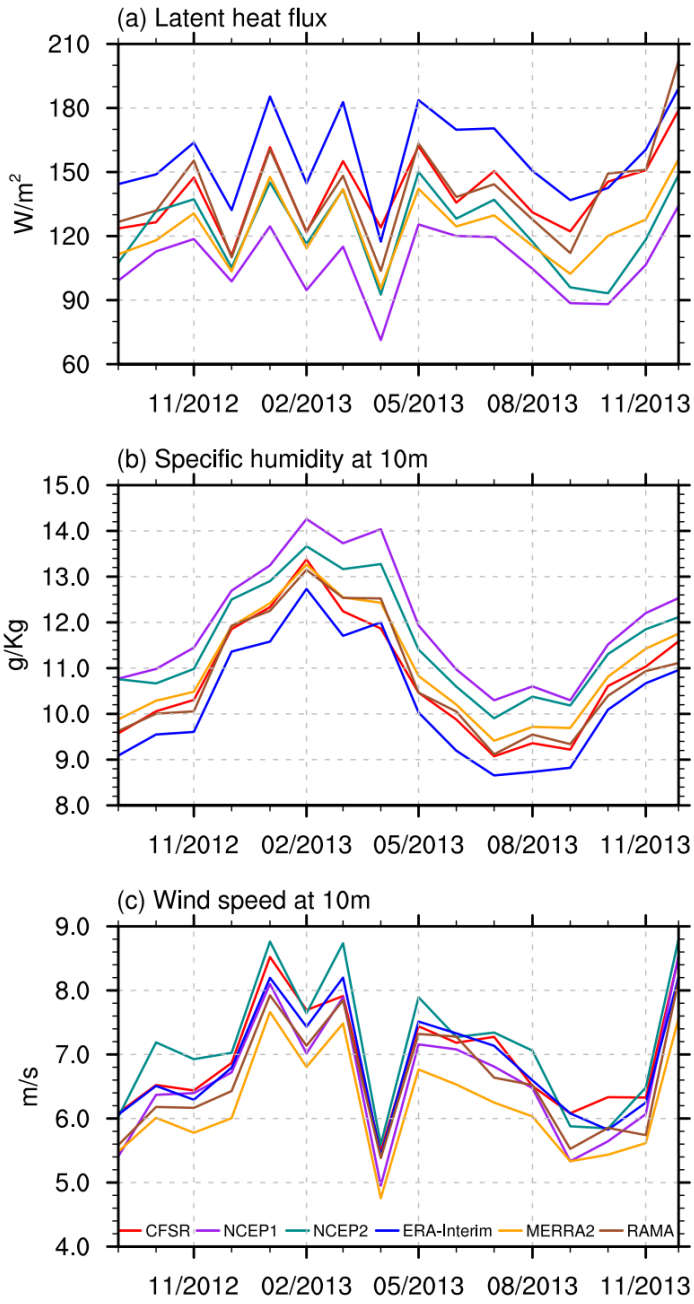

Figure 2.4. (a) Comparison of monthly mean latent heat flux from EX-alg with those from the RAMA buoy at 100°E, 25°S. The positive values indicate the flux from the ocean to the atmosphere. (b) Comparison of Specific humidity at 10 m from reanalysis with those from RAMA buoy at the same location. (c) Same as in (b), but for wind speed at 10 m.

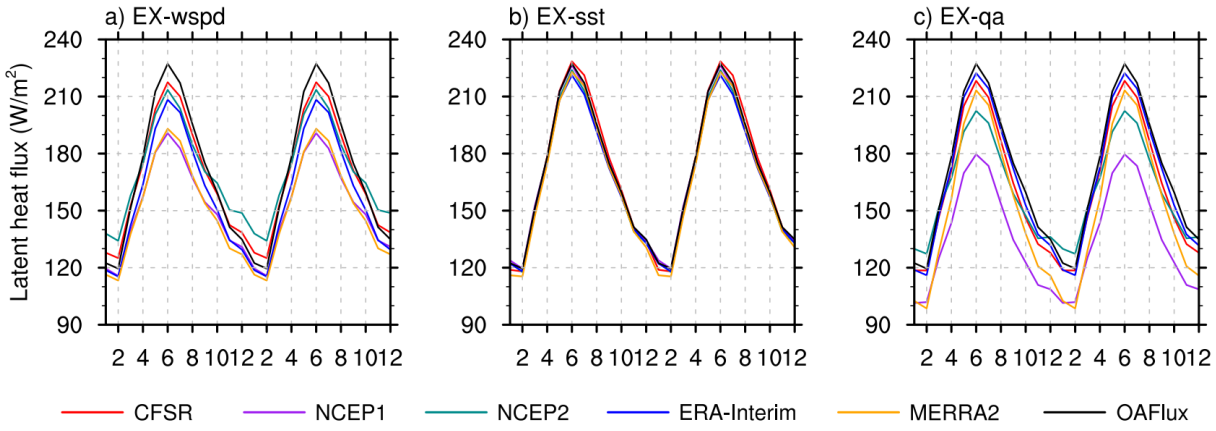

Figure 2.5. Climatological seasonal cycle of latent heat flux (into the atmosphere) over the region (110°E-116°E, 22°S-32°S) from (a) EX-wspd, (b) EX-sst, (c) EX-qa.

2.3.2 Air-sea fluxes associated with Ningaloo Niño

In the previous subsection, large uncertainties of air-sea fluxes are identified in the climatological seasonal cycle. In this subsection, surface heat fluxes associated with the Ningaloo Niño, which is the major interannual variability in this region, are investigated and their uncertainties are determined using the same datasets.

Ningaloo Niño events are identified based on the Ningaloo Niño Index (NNI) defined as the average of SST anomalies over the region 110°E-116°E, 22°S-32°S (Marshall et al., 2015). Years when the DJF averaged NNI is above one standard deviation are defined as the Ningaloo Niño years. For the entire period of the analysis, 6 events are identified: 1988/89, 1996/97, 1999/2000, 2010/11, 2011/12, 2012/13 (Figure 2.6). The composite time series of surface heat flux anomalies, which cover the period of onset, development, and recovery of the events, are constructed by averaging all 6 events. Month 0 in the composite is defined as the month of the maximum positive SST anomaly in the region used for the NNI calculation.

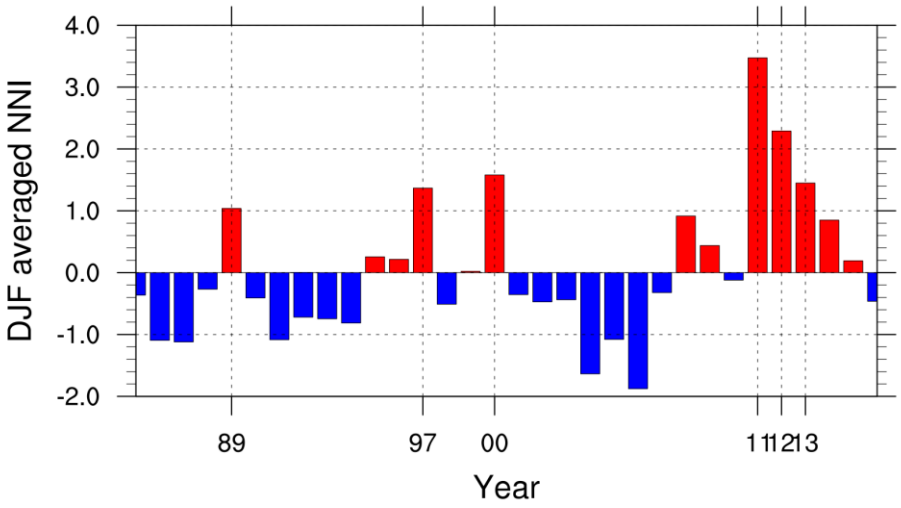

Figure 2.6. DJF averaged Normalized Ningaloo Niño Index calculated from the NOAA 1/4° daily Optimum Interpolation Sea Surface Temperature. The year shown on the horizontal axis corresponds to the year of January and February.

Despite the large uncertainties in climatology, anomaly fields show much smaller differences between the datasets. However, these uncertainties are still significant because they are in the same order as the amplitude of the anomaly particularly during the warming period. In addition, the sign of the latent heat flux anomalies varies between the datasets during the developing phase of Ningaloo Niño, suggesting the opposite role of latent heat flux. Large variations associated with the Ningaloo Niño are detected in all datasets (Figure 2.7). For instance, during the developing phase, a significant increase in net surface heat flux is found from month -3 to -2 and month -1 to 0. Then the anomalous surface heat flux decreases sharply from month 0 to month +1, resulting in substantial cooling during the recovery phase (Figure 2.7a). The sharp decrease (cooling) in the recovery phase is seen clearly in all datasets and it is dominated by the latent heat flux anomaly fluctuation (Figure 2.7b-e). Similar variations are found for the composite using turbulent heat fluxes from OAFlux and shortwave and longwave

radiation from CERES (not shown), but only the last three events are used for this composite because of the shorter period the CERES data cover.

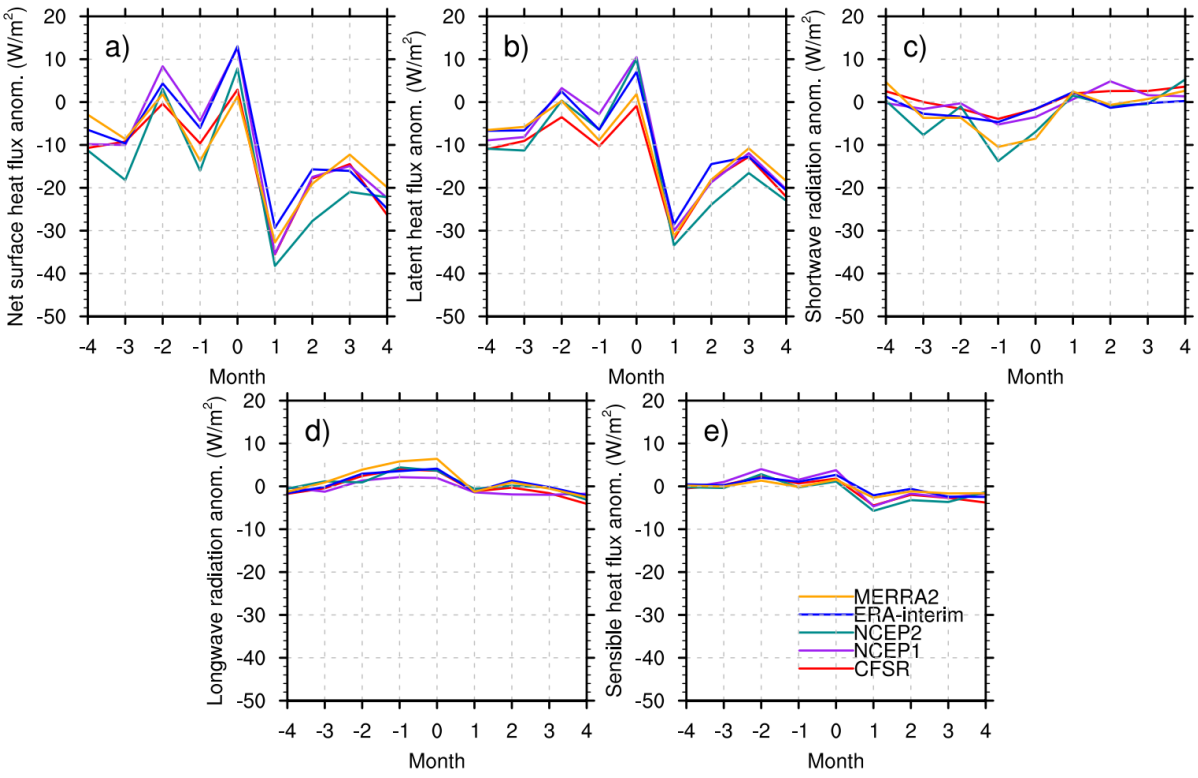

Figure 2.7. Composites of the monthly mean net surface heat flux, latent heat flux, shortwave radiation, longwave radiation, and sensible heat flux anomalies over the region (110°E-116°E, 22°S-32°S) for Ningaloo Niño years. The sign of the longwave radiation, latent and sensible heat flux has been adjusted so that positive values indicate the warming of the ocean. Month 0 is the month of the maximum positive SST anomaly.

To further examine how the fluctuation of the latent heat flux associated with the Ningaloo Niño event occurs, spatial patterns of surface wind anomalies are compared with those of climatological surface winds (Figure 2.8). During December-April, climatological

southeasterly winds prevail around the west coast of Australia. When the Ningaloo Niño is fully developed at month 0, the northerly wind anomalies reach the peak, which largely decreases the climatological southeasterly and thus reduces the wind speed. Such reduction of wind speed is also found in month -2 although it is much weaker. The latent heat flux anomalies from some of the datasets are positive during the development and peak phases due to the weakening of surface winds described above, which are consistent with the windspeed-evaporation-SST (WES) feedback mechanism suggested in previous studies (e.g., Marshall et al., 2015; Nicholls, 1979). However, the positive latent heat flux anomalies are not found in some of the datasets during this period.

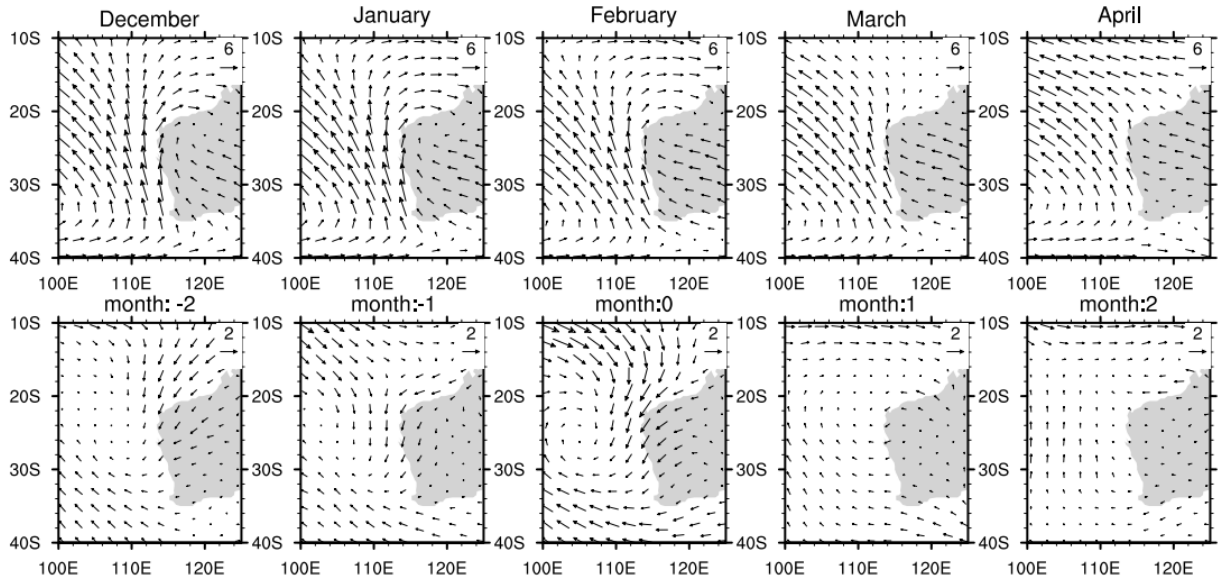

Figure 2.8. Upper panels: Climatological monthly surface winds. Lower panels: Composite of surface wind anomalies (m s^{-1}) for Ningaloo Niño years. Surface winds from ERA-Interim are used for the analysis.

During month +1 soon after the peak, the wind anomaly rapidly changes to weak southerly, resulting in an increase of wind speed by 1 m/s. Since SSTs recover much slower and thus they are still anomalously high in month +1 (Figure 2.9e), the evaporative cooling (negative latent heat flux anomaly) is rapidly enhanced, which contributes to the SST cooling. By month +2, evaporative cooling is reduced because of the decrease of SST although wind speed similar to month +1 is maintained. The variation of latent heat flux anomaly including the rapid increase of negative anomalies in month +1 is found in all datasets. The cooling anomalies in longwave radiation and sensible heat flux, which are associated with high SSTs, are found (Figure 2.7d, e), but their contributions to SST recovery are much smaller than those of latent heat flux.

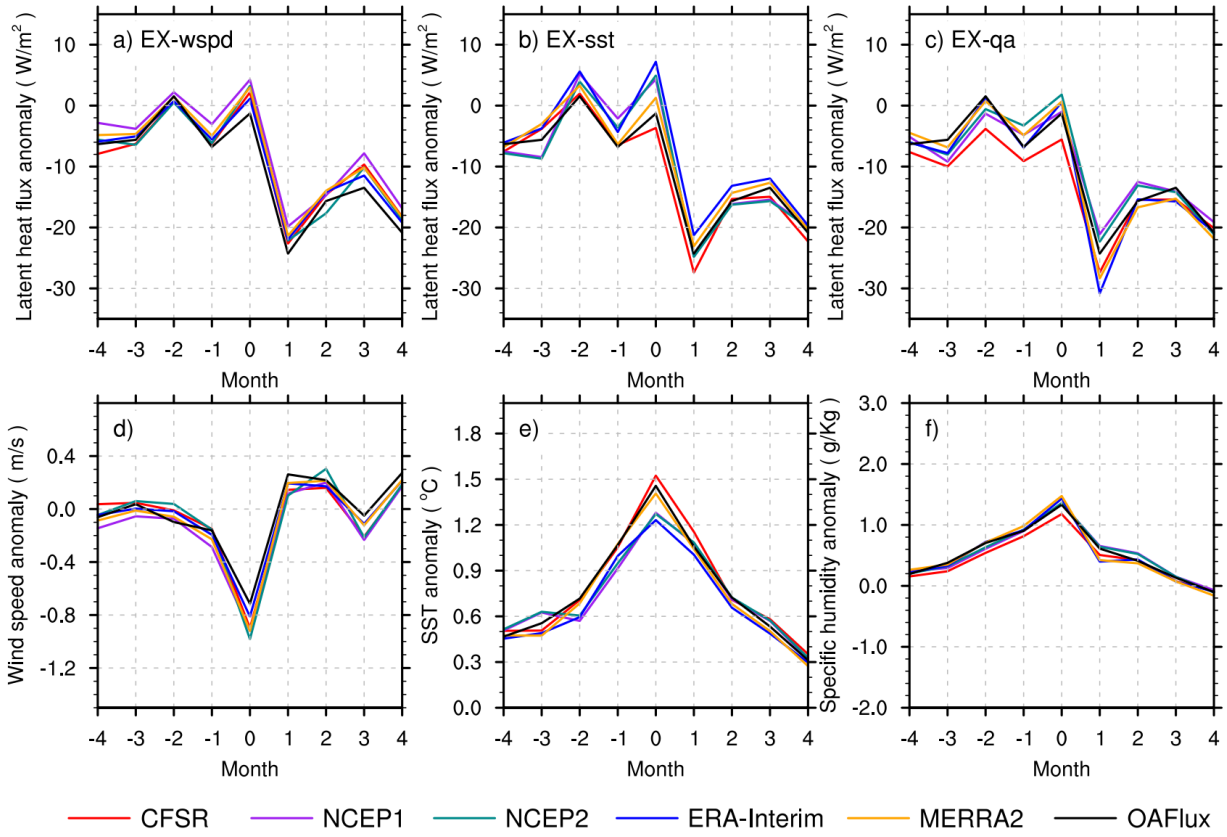

Figure 2.9. The top row: The composites of monthly heat flux anomalies over the region (110°E-116°E, 22°S-32°S) from (a) EX-wspd, (b) EX-sst and (c) EX-qa. Positive values indicate the warming of the ocean. The bottom row: The wind speed anomalies (d), SST anomalies (e), and specific humidity anomalies (f) from the reanalysis datasets.

In contrast to the recovery phase, the variation of latent heat flux and its contribution to SST growth during the developing phase show disagreement between the datasets. NCEP1 shows warming anomalies during month -2 to 0, while others reveal cooling anomalies (CFSR, MERRA2) or alternate between cooling and warming (NCEP2, ERA-Interim). It is not clear whether the latent heat flux anomaly significantly contributes to the SST warming during the Ningaloo Niño onset. These results are consistent with those of previous studies, which used

different surface heat flux products and concluded different roles of surface heat fluxes during the onset and development phases (e.g., Feng et al., 2013; Kataoka et al., 2017; Marshall et al., 2015).

The major sources of the uncertainty during the onset period are further investigated based on the additional analysis using EX-wspd, EX-sst and EX-qa described in Section 2.3.1. Composites of latent heat flux anomalies from EX-wspd, EX-sst, and EX-qa are displayed in Figure 2.9. The mean of the difference between the maximum and minimum latent heat flux anomaly during the entire period of composite is 4.1, 4.7, and 5.0 W m^{-2} for EX-wspd, EX-sst, and EX-qa, respectively. This suggests that air specific humidity errors could cause larger uncertainties of latent heat flux anomalies, which is similar to the results from the analysis of climatological latent heat flux. However, the largest differences between the datasets during the peak phase are found in EX-sst (Figure 2.9b), which is 10.9 W m^{-2}, and the sign of latent heat flux anomaly also shows a disagreement between the datasets. While a significant difference (7.4 W m^{-2}) is also found in EX-qa in month 0, the sign of the latent heat flux anomaly is the same in most datasets. This result indicates that the uncertainties in SST significantly contribute to the errors in latent heat flux during this period. Since the SST is highest at the peak month, the latent heat flux is most sensitive to changes in SSTs during this period. In other words, even small errors in SST could impact the latent heat flux significantly during the onset and peak periods.

The SST difference between the datasets is largest in the peak period (month 0) (Figure 2.9e). While SSTs used in the flux products are based on similar satellite observations, their spatial resolutions could influence the accuracy since SST in this region is largely affected by Leeuwin Current variability (Huang and Feng 2015). Such SST differences caused by the resolution are demonstrated for the 2010-2011 Ningaloo Niño case. The monthly latent heat flux

and SST anomaly during the event are shown in Figure 2.10. To exclude the latent heat flux uncertainties caused by algorithm, wind speed, and humidity, we use fluxes from EX-sst instead of the original reanalysis. In addition to SST products used in the original EX-sst, high resolution OISST and MUR are also included in this case study.

The peak of this Ningaloo Niño occurred in February 2011. From November 2010 to February 2011, warm SST anomalies were built up near the west coast of Australia (Figure 2.10b). During this time, significant positive latent heat flux anomalies (10-30 W m^{-2}, positive value denote heat going into the ocean) are evident in NCEP1, NCEP2, ERA-Interim, and MERRA2, suggesting that air-sea fluxes may contribute to the SST warming. In contrast, CFSR, OAFlux, MUR, and OISST show very small positive anomalies into the ocean, or even negative anomalies in December 2010 and January 2011 (Figure 2.10a, Figure 2.12). These differences are caused by warmer area average SSTs for the relatively high-resolution SST products (MUR, OISST) (Figure 2.10b).

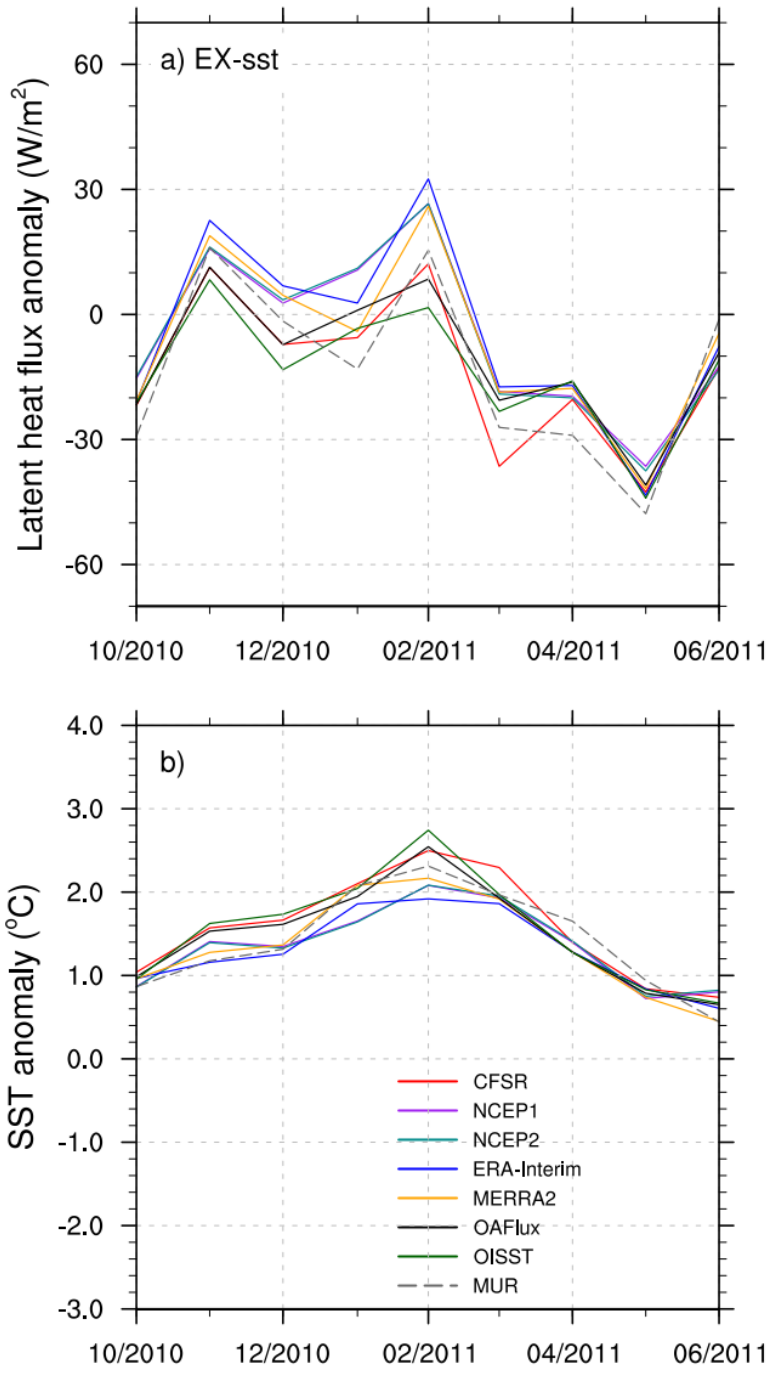

Figure 2.10. (a) Monthly mean latent heat flux anomalies over the region (110°E-116°E, 22°S-32°S) for the 2010/2011 Ningaloo Niño event from EX-sst. Positive values indicate the warming of the ocean. (b) The corresponding SST anomalies from reanalysis products and satellite observations.

Figure 2.11 shows SST maps from different datasets during the peak period of the 2010-2011 Ningaloo Niño event. The southward extension of warm waters carried by the Leeuwin Current is evident clearly in the high-resolution data (MUR and OISST), while it is not well represented in the low-resolution data. Accordingly, higher area average SSTs and thus higher evaporative cooling are found in the case of high-resolution SSTs (Figure 2.12). The results demonstrate that it is crucial to resolve SST changes caused by Leeuwin Current variability adequately for the latent heat flux estimates especially during the peak period of Ningaloo Niño.

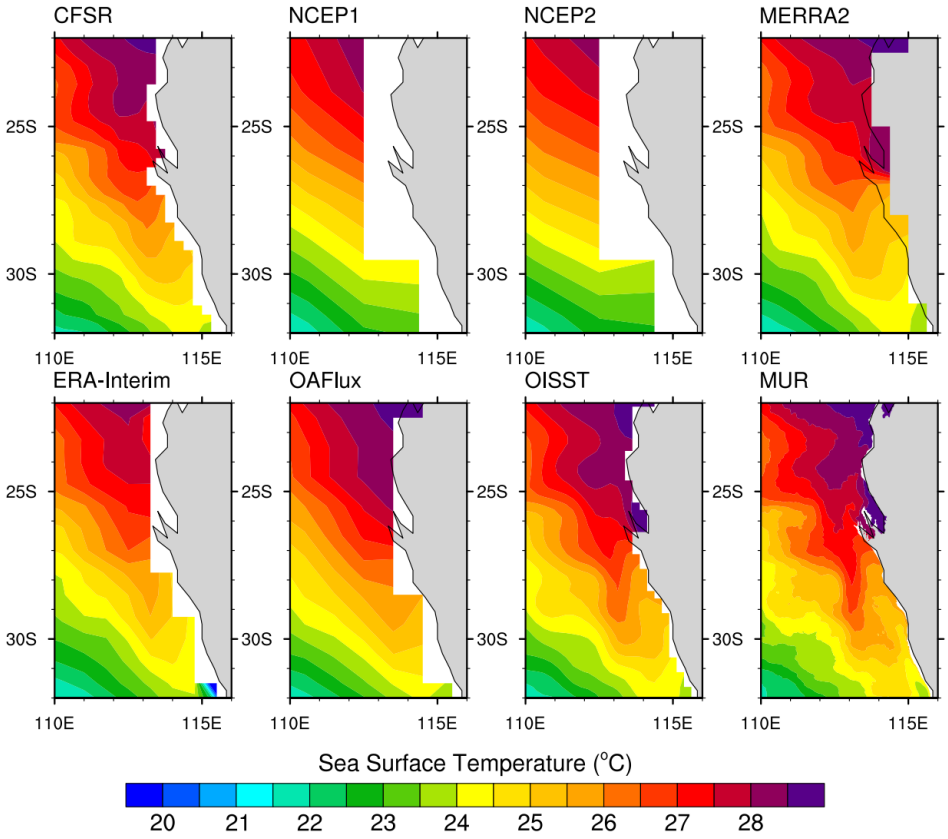

Figure 2.11. Mean SST of January and February 2011 over the west coast of Australia from different SST datasets.

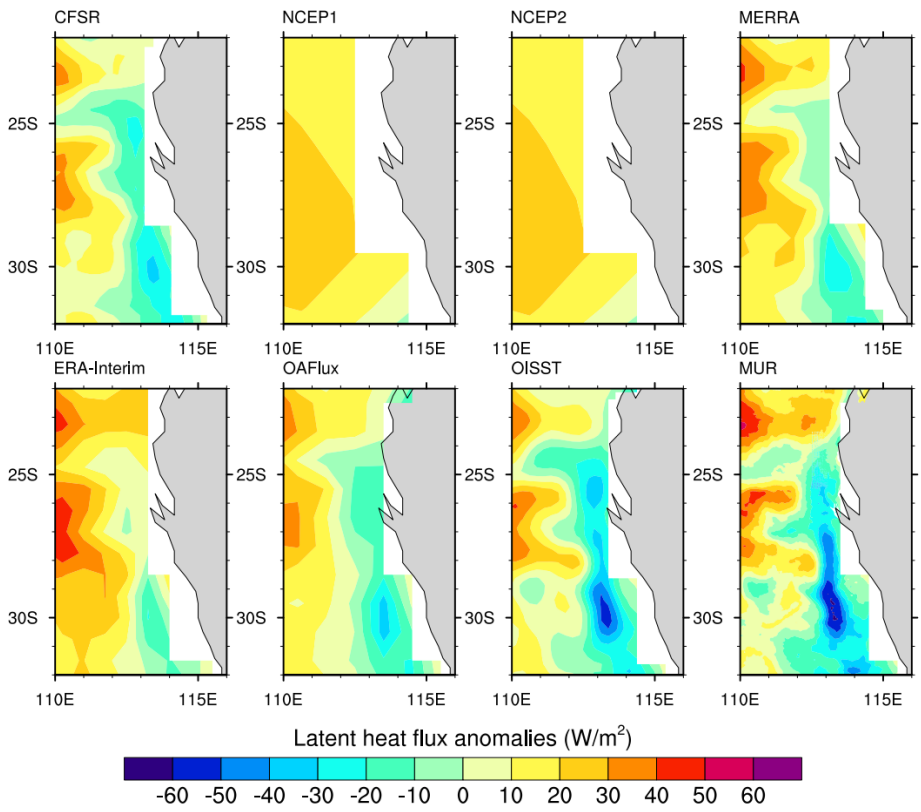

Figure 2.12. Mean latent heat flux anomalies of January-February 2011 over the west coast of Australia from EX-sst. Positive values indicate the warming of the ocean.

2.4 Discussion

The results in the previous section demonstrate that large negative surface heat flux anomalies are found during the decay periods of the Ningaloo Niño in all datasets, and that the latent heat flux anomaly is the dominant component. Such large latent heat fluxes (evaporation) could significantly impact the atmospheric conditions and circulation.

In addition to the air-sea flux anomalies, MLD changes associated with the Ningaloo Niño could influence the SST evolution (Kataoka et al. 2017). Kataoka et al. (2017) suggested that the cooling due to latent heat flux anomalies during the decay period could be largely

reduced by MLD variability, and the sensible heat flux significantly contributes to the SST cooling for some events.

To further investigate the relative importance of latent and sensible heat fluxes for the SST variations during the decay phase, these flux terms in the following mixed layer heat budget equation are calculated (Equation 7 in Kataoka et al. 2017):

$$\left(\frac{Q}{\rho c_p h}\right)' = \frac{Q'}{\rho c_p \overline{h}} - \frac{\overline{Q}}{\rho c_p \overline{h}} \frac{h'}{\overline{h}} + Res \tag{2.1}$$

where Q is the surface heat flux, ρ is seawater density, c_p is the specific heat of seawater, and h is the MLD. An overbar represents monthly climatology and a prime represents anomaly. The first term on the RHS represents the contribution of the surface heat flux anomaly, and the second term represents the contribution of MLD variability through the change of the mixed layer heat capacity. The MLD is derived from the HYCOM reanalysis which is defined as the smaller depth at which the temperature is decreased by 0.2 °C or the salinity is increased by 0.03 psu from the surface values. The seasonal variation of MLD from the HYCOM reanalysis agrees well with observations (e.g., CARS, Supplementary Figure S1). The composite latent and sensible heat flux anomalies, which include the effect of MLD changes, are shown in Figure 2.13, and the composites of the first and second term on the RHS of equation (1) are shown in Figure 2.14. Significant contributions of MLD changes are evident (Figure 2.13, Figure 2.14). For example, the weak cooling (negative anomaly) is found during the onset and peak phase in the latent heat flux term (Figure 2.13) in all datasets whereas the weak warming is found in some datasets when the effect of MLD change is not included (Figure 2.7). The contribution of the MLD change (second term) is relatively large during the onset and peak phase as the first term is small. Yet the latent heat flux term is still dominant and contributes to the cooling during the

decay period much more than the sensible heat flux term. The variation of latent heat flux in Figure 2.13 is similar to that of non-locally amplified Ningaloo Niño in Kataoka et al. (2017). It should be noted that there are no significant differences between locally and non-locally amplified modes in the analysis of this study.

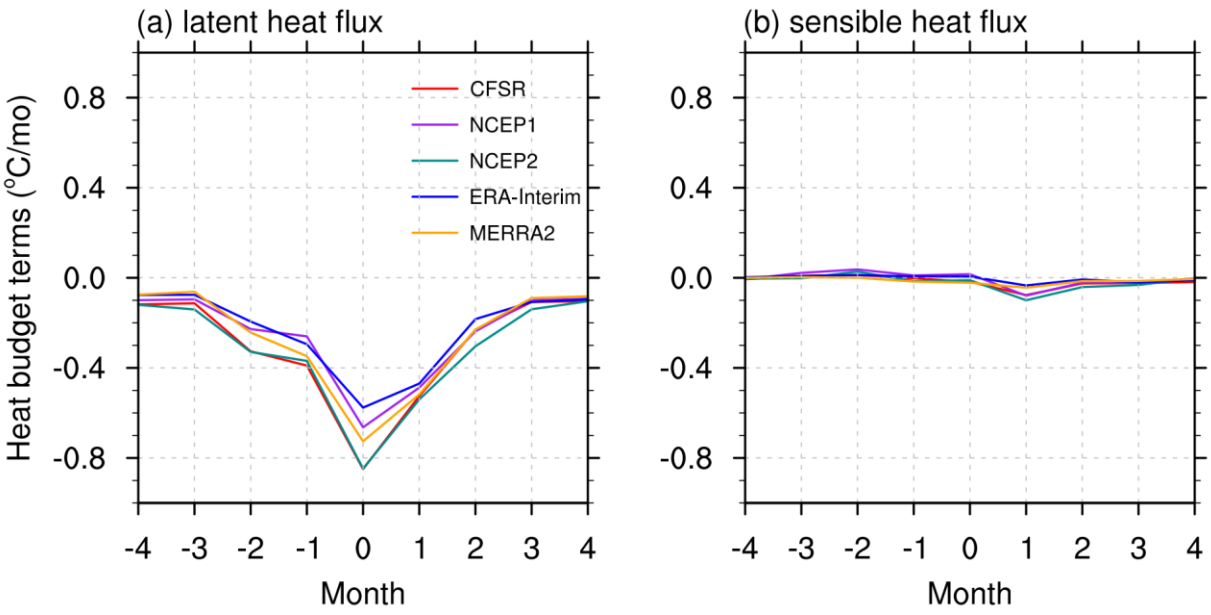

Figure 2.13. Composites of monthly mean heat flux anomaly term in the mixed layer heat budget equation over the region (110°E-116°E, 22°S-32°S): (a) latent heat flux term, (b) sensible heat flux term.

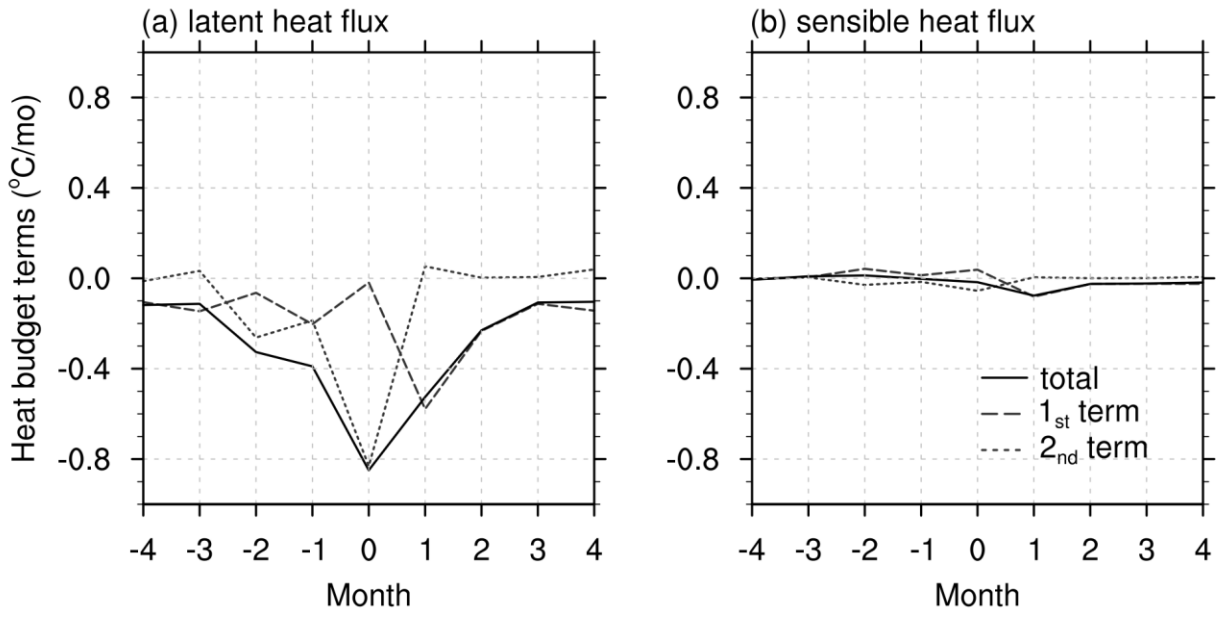

Figure 2.14. Composite monthly mean heat flux anomaly terms calculated from the mixed layer heat budget equation for the region (110°E-116°E, 22°S-32°S). The first and second terms on the RHS of equation (1) are compared. Only the results from CFSR are shown. The first term represents a temperature tendency produced by the flux anomaly with the climatological MLD, and the second term represents a temperature tendency produced by climatological fluxes and the MLD anomaly.

Although the reason for the differences between the results of this study and Kataoka et al. (2017) is unknown, it is likely that different sources of the data including air-sea fluxes and MLD are primarily responsible for the differences. In particular, the interannual variation of MLD could be largely model dependent. Thus, further studies which focus on the interannual variability of upper ocean structures including the MLD are necessary.

While earlier studies suggest that a reduction of latent heat flux partially contributes to SST anomalies at the peak of Ningaloo Niño, an opposite conclusion could be obtained when

taking into account of MLD variation. Figure 2.13 shows that the latent heat flux damps SST anomalies in all stages of Ningaloo Niño and the cooling reach the maximum during the peak. At the peak phase, large differences in latent heat flux anomaly between the datasets and thus large uncertainties are found. Again, these uncertainties are likely to be related to the resolution of SST.

In addition to the influence of air-sea fluxes on the upper ocean temperature, these heat and moisture fluxes directly affect the atmosphere. In particular, the latent heat fluxes (evaporation) could largely contribute to moisture budget changes in the atmosphere during the period of Ningaloo Niño and thus air-sea interaction. A recent modeling study demonstrates that the Ningaloo Niño could develop without ENSO, and the intrinsic air-sea interaction alone may induce atmospheric cyclonic circulation anomalies and a stronger Leeuwin Current (Kataoka et al. 2018). As the present study suggests the importance of the resolution of SST for the latent heat flux estimates off the west coast of Australia, coupled model simulations using the high-resolution ocean component would be useful to investigate the feedbacks between the atmosphere and ocean that control the development of Ningaloo Niño.

2.5 Summary

This study investigates the air-sea flux variability off the west coast of Australia using multiple datasets and satellite observations. We found large uncertainties in climatological net surface heat fluxes. The uncertainties result primarily from latent heat flux and shortwave radiation. The possible causes of the uncertainty for latent heat flux are investigated with additional calculations which isolate the effects of wind speed, SST, humidity, and bulk flux algorithm. The results of these calculations suggest that the use of different bulk flux algorithms

largely contributes to the uncertainties. The bulk atmospheric variables also significantly contribute to the uncertainties.

The role of air-sea fluxes in the development and decay of Ningaloo Niño is investigated based on the composite analyses over the life cycle of Ningaloo Niño. Large differences in air-sea flux anomaly fields associated with the Ningaloo Niño between the datasets are evident although they are smaller than the differences in climatological air-sea flux. Large negative air-sea heat flux anomalies (cooling the ocean) in the recovery phase are found in all datasets, and the anomalous latent heat flux is the dominant component. This suggests that the latent heat flux plays an important role in damping the positive SST anomalies during the recovery stage. The composite evolution of surface winds suggests that WES feedback is responsible for the variations of latent heat flux. Since SSTs recover much more slowly than surface winds after the peak of SST warming, large evaporative cooling is favored under the condition of strong winds and warm SST especially during the early stage of the recovery phase. Then the evaporative cooling is reduced as the SST gradually recovers.

During the developing phase, however, the contributions of air-sea heat flux have large uncertainties. Sensitivity calculations show that the differences in SST anomaly between the datasets largely contribute to the uncertainties. Large uncertainties around the period of SST peak are partly due to the warmer SST than other periods, since the small errors in SST could generate large latent heat flux changes. Also, SST anomalies are directly related to the strengthening of the Leeuwin Current, and thus the resolution of SST datasets significantly affects the SST anomalies. A case study of the 2010-2011 Ningaloo Niño event demonstrates a close relationship between the SST anomaly and the resolution of the datasets. The southward extension of warm waters transported by the Leeuwin Current can be adequately resolved only

by high-resolution SST datasets. As a result, a relatively cold SST and thus smaller evaporative cooling are estimated using the low-resolution SST datasets.

CHAPTER III: THE LEEUWIN CURRENT IN AN EDDY-PERMITTING AND EDDY-RESOLVING OGCM

3.1 Introduction

The Leeuwin Current (LC) is the dominant near-surface current in the southeast Indian Ocean, which flows poleward along the west coast of Australia from 22°S (North West Cape) to 34°S (Cape Leeuwin), then eastward into the Great Australian Bight with a total distance of 5500 km (Cresswell and Golding 1980; Ridgway and Condie 2004). The LC is energetic and often appears as a meandering flow. Observations indicate that the LC has a mean speed of about 30 cm s^{-1} and its width is less than 100 km (Cresswell and Golding 1980; Smith et al. 1991). The LC carries warm tropical waters southward, because of the warm current the sea surface temperature (SST) is significantly warmer near the west coast of Australia than in other eastern boundary regions in the Atlantic Ocean and Pacific Ocean at similar latitudes (Feng et al. 2003).

The LC has a strong seasonal variation with a maximum poleward transport of ~ 5 Sv (1 Sv$\equiv 1\times10^6$ m^3 s^{-1}) in May-July (Cresswell and Golding, 1980, Smith et al., 1991, Feng et al., 2003). The local wind variations influence the annual cycle of the LC. The LC strengthens in late autumn and early winter when the southeasterly wind is weak (McCreary et al. 1986; Smith et al. 1991). Godfrey and Ridgway (1985) argued that the seasonal enhancement of the LC is due to the geostrophic adjustment to the increased cross-shelf sea level gradient. Ridgway and Godfrey (2015) further demonstrated that the higher sea level at the coast during austral autumn/winter is associated with the annual propagating waves originating from the Gulf of Carpentaria and forced by monsoon winds.

On interannual timescales, the LC variability is influenced by the ENSO in the Pacific Ocean. During La Niña years, the LC is strong with a mean transport of 4.2 Sv at 32°S, and

during El Niño years, the LC is weaker with a decreased meridional transport of 3.0 Sv (Feng et al. 2003). In 2010-2011, a strong La Niña developed in the equatorial Pacific Ocean, resulting in strong LC intensification along the west coast of Australia. The surge of the LC caused extreme upper-ocean warming in the coastal regions near Western Australia for several months, which is associated with increased rainfall, widespread fish fatality, and coral bleaching (Pearce et al. 2011). This warming event was named “Ningaloo Niño” (Feng et al. 2013).

Because of the significant societal and economic impacts of the Ningaloo Niño, evaluating the ability of numerical models to simulate such events is critical for the prediction of future Ningaloo Niño. Marshall et al. (2015) conducted a heat budget analysis using a high- and low-resolution ocean reanalysis and found that the anomalous poleward heat advection associated with the strengthening of LC plays a dominant role in the 2010-2011 Ningaloo Niño event. However, because the variability of the LC was not well captured in the low-resolution reanalysis, inconsistencies were detected in the amplitude of the heating during the developing and peak phase compared with a high-resolution ocean reanalysis dataset. Figure 3.1 compares the annual mean LC at 32°S derived from recently released three ocean reanalysis products, which are the European Centre for Medium-Range Weather Forecasts (ECMWF) Ocean Reanalysis System 4 (ORAS4; Balmaseda et al. 2013) with a horizontal resolution of 1° in the extratropics, the Estimating the Circulation and Climate of the Ocean, version 4, release 4 (ECCOV4r4; Forget et al. 2015) with a grid spacing of approximately 100 km at midlatitudes, and the Simple Ocean Data Assimilation, version 3 (SODA3; Carton et al. 2018) with a finer 1/4° eddy-permitting horizontal resolution. Compared with observations, a better representation of the LC is found in SODA3, whereas the magnitude of LC in ORAS4 and ECCOV4r4 is

significantly underestimated, suggesting that the horizontal resolution of ocean models may have a considerable impact on the strength and structure of the simulated LC.

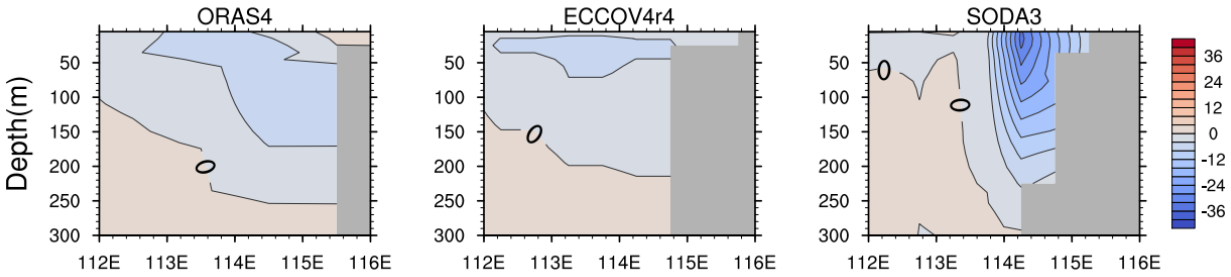

Figure 3.1. Zonal sections of the climatological mean meridional velocity (cm s^{-1}) along 32°S averaged over 2008-2015 from reanalysis datasets: (left) ORAS4, (middle) ECCOV4r4, (right) SODA3.

Previous studies have employed various numerical models to investigate the generation mechanism of the Ningaloo Niño, including the air-sea coupling process and remote forcing through the atmosphere and ocean teleconnection. However, many of the studies relied on either eddy-permitting, basin-scale ocean models or eddy-resolving, regional ocean models in which the boundary conditions are derived from relatively low horizontal resolution ocean reanalysis (e.g., Kataoka et al. 2017; Zhang et al. 2018; Kusunoki et al. 2020). Because the use of low-resolution OGCM or ocean reanalysis may induce significant errors in the LC variability during Ningaloo Niño, it is necessary to evaluate the influence of model resolution on the LC to improve our understanding of key processes associated with the Ningaloo Niño.

In this study, two OGCM experiments with different horizontal resolutions are conducted to investigate the sensitivity of the LC to the ocean model resolution. The OGCM is configured for the Indo-Pacific domain to take into account the remote influence of ENSO. Model outputs

from the two experiments are analyzed to investigate LC climatology and variability during the 2010-2011 Ningaloo Niño.

3.2. OGCM experiments

The ocean model used in this study is the Hybrid Coordinate Ocean Model (HYCOM 2.2.98; Bleck 2002). HYCOM is a primitive equation OGCM with hybrid vertical coordinates, which are isopycnal coordinates in the open, stratified ocean, terrain-following (sigma) coordinates in the shelf region, and z-level coordinates in the upper-ocean mixed layer. The model is configured with 40 vertical layers, among which 14 layers are set to hybrid z-sigma layers to better resolve the shelf and mixed layer processes and the layer thickness gradually increases from 1 m (top layer) to 8 m (layer 14). The bathymetry is adapted from 30 second General Bathymetric Chart of the Oceans (GEBCO; Weatherall et al. 2015). The model domain covers the Indo-Pacific basin from 10ºN to 55ºS and 10ºE to 67ºW. Two model experiments with different horizontal resolutions are conducted to isolate the impact of the resolution on the simulated LC. The eddy-permitting model experiment has a grid spacing of 1/4° (hereafter refer to as EXP-L) and the eddy-resolving model experiment has a grid spacing of 1/12° (hereafter refer to as EXP-H).

The K profile Parameterization (KPP; Large et al. 1994) is used as the vertical mixing scheme, and the CORE v2 bulk flux algorithm (Large and Yeager 2004) is used to calculate the surface heat fluxes. The air temperature (T_a) and specific humidity (q_a) at 2 m used in the bulk flux algorithm are calculated from the model SST using the following empirical formula:

$$T_a = SST - \Delta T$$
$$q_a = Rh * q_s(T_a) \quad (3.1)$$

where ΔT is the difference between SST and T_a, Rh is relativity humidity, and $q_s(T_a)$ is the saturation specific humidity at T_a. Monthly climatological values of ΔT and Rh at each location are estimated using SST, T_a and Rh from the WHOI Objectively Analyzed Ocean-Atmosphere Flux (OAFlux) product (Yu et al. 2008) for the period 1985-2016. More discussions on the selection of input atmospheric variables for the bulk algorithm can be found in Chapter 4. In addition, relaxation boundary conditions are used at the north, south, and west boundaries. A sponge layer with 20 grid points is used, in which the model temperature and salinity are relaxed to the Polar science center Hydrographic Climatology (PHC) 3.0 (Steele et al. 2001).

The model has been spun up from a motionless state for 20 years with the climatological temperature and salinity from PHC3.0. Then models with different resolutions (EXP-L and EXP-H) are integrated from 2002 to 2015 using daily surface forcing fields from EAR5 reanalysis (Hersbach et al. 2018). The outputs for 2004-2015 from EXP-L and EXP-H are used in the following analysis.

3.3 Results

In this section, the simulated LC from EXP-L and EXP-H are compared, and the impact of the model resolution on the LC annual mean state and its variability during the 2010-2011 Ningaloo Niño are investigated. Because the heat advection by the LC plays a dominant role in the 2010-2011 Ningaloo Niño, the differences in upper ocean temperature between EXP-L and EXP-H, which mainly arise from the difference in the simulated LC, are also examined.

3.3.1 The mean current

Because the strongest LC lies within the upper 50 m, Figure 3.2 compared the upper 50 m averaged current from EXP-L and EXP-H for the region off Western Australia. Figure 3.2a shows that the spatial structure of the LC is represented reasonably well in the eddy permitting

EXP-L, with the LC being located along the west coast of Australia south of 22°S and stronger towards the south coast. Compared with EXP-L, significant improvements in the LC simulation are found in EXP-H including a more realistic LC speed and better spatial structure (Figure 3.2b). The LC in EXP-H is stronger than in EXP-L for almost the entire Australian west coast. In the middle part of the west coast around 30°S, EXP-H can maintain an LC speed of ~20 cm s^{-1}, which is consistent with observations (Furue et al. 2017). However, the magnitude of LC in EXP-L is underestimated partly because the low-resolution model cannot resolve the narrow width of the LC. Furthermore, the zonal scale of LC is well simulated in EXP-H, and a seasonally reversing coastal current is distinguishable over the continental shelf. In EXP-L, the LC is wider, and the shelf current is difficult to identify.

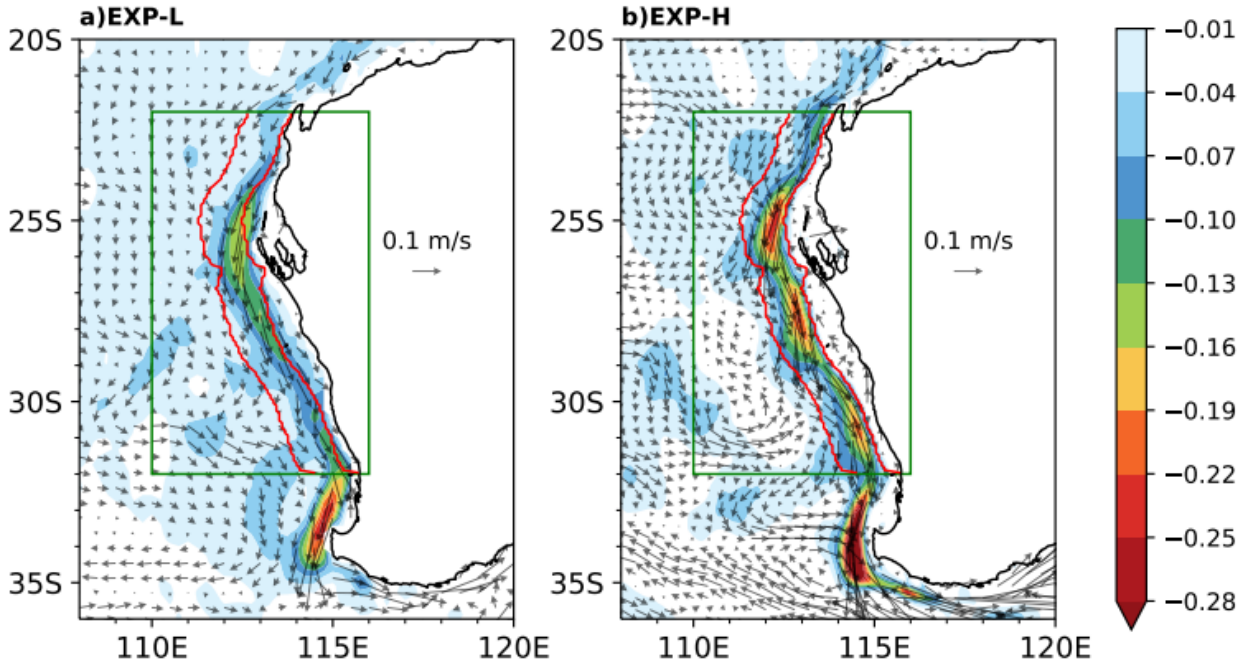

Figure 3.2. Mean current averaged for the upper 50 m and 2004-2015: (a) EXP-L, (b) EXP-H. The meridional velocity is shaded. The green box indicates the NNI region, the red lines indicate the outline of the LC defined in section 3.3.2.

The difference in LC magnitude between EXP-L and EXP-H varies with latitudes (Figure 3.2). To quantify the difference and further evaluate the vertical structure of LC at different latitudes, zonal sections of the meridional velocity at 22°S, 26°S, 30°S, and 34°S are compared in Figure 3.3. In both experiments, the LC deepens from 22°S to 34°S and an intensification of the LC near the shelf break is observed at 26°S and 34°S. While the intensification at the shelf break is also found at 30°S in EXP-H, it does not exist in EXP-L because the 1/4° grid spacing cannot resolve the continental shelf and slope. In addition, large differences in the core velocity (maximum southward velocity) are evident. Table 3.1 lists the core velocity of the LC from the model and from previous observational studies, in which geostrophic velocities are calculated from the historical hydrographic measurements. It shows that the core velocity of the LC in EXP-H is more realistic than in EXP-L and the magnitude of the LC in EXP-H is 1.7, 1.1, 1.6, and 1.9 times stronger at 22°S, 26°S, 30°S, and 34°S than in EXP-L.

Table 3.1. Core velocity (cm s^{-1}) of the mean LC at 22°S, 26°S, 30°S, and 34°S from EXP-L, EXP-H, and observations.

Latitude	*EXP-L (1/4 deg)*	*EXP-H (1/12 deg)*	*Observations**
22°S	7.9	13.8	10
26°S	17.0	19.3	>16
30°S	11.0	17.6	>20
34°S	23.2	43.9	>20

*Observations are extracted from Furue et al. (2017) and Furue (2019).

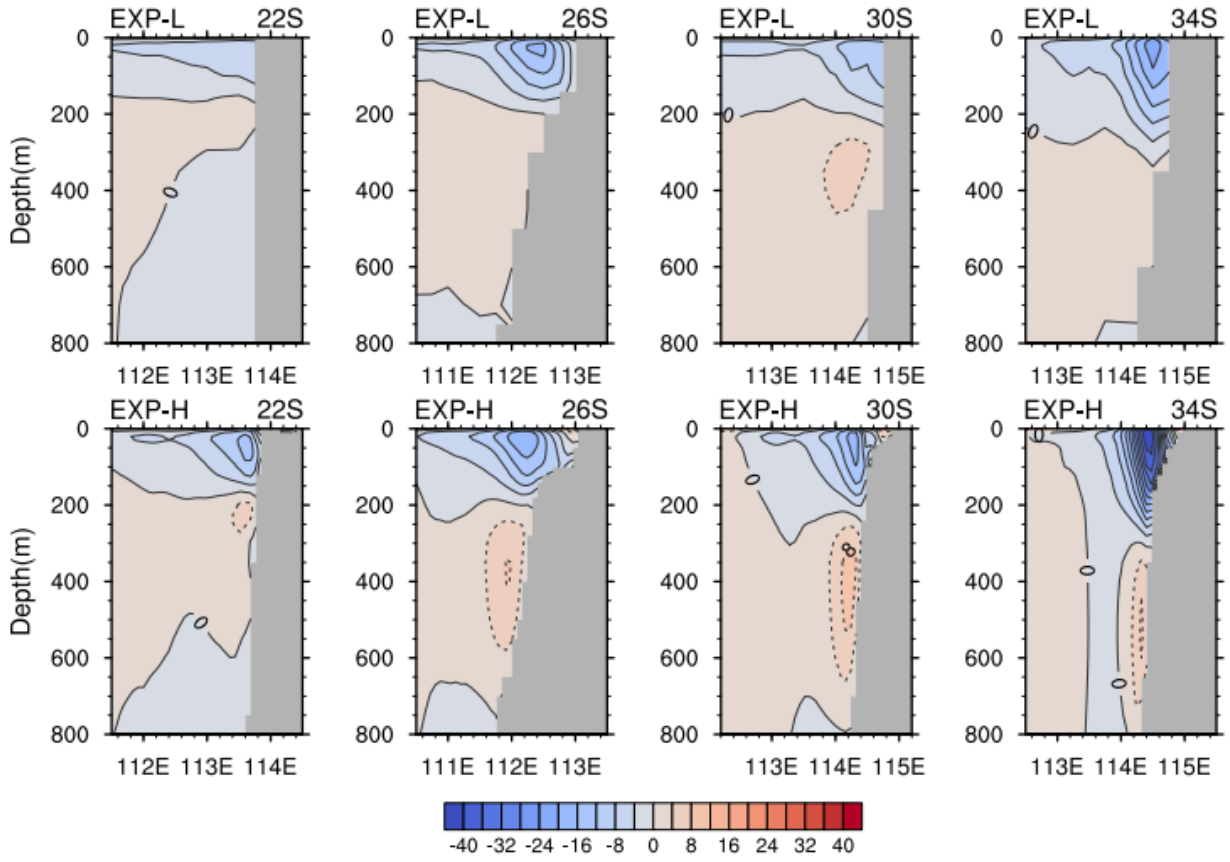

Figure 3.3. Zonal sections of the mean meridional velocity averaged over 2004-2015 (cm s^{-1}) at 22°S, 26°S, 30°S, and 34°S: (upper) EXP-L, (lower) EXP-H. The contour interval is 4 cm s^{-1}.

3.3.2 The seasonal variability

Figure 3.4 shows the seasonally averaged upper 50 m horizontal velocity from EXP-L. A stronger LC exists in late austral autumn and early winter (Figure 3.4b), and a weaker current in the austral spring and summer months (Figure 3.4d), which is consistent with observations (e.g., Feng et al. 2003, Furue et al. 2007). A similar annual cycle of the LC is also found in EXP-H (Figure 3.5), but a larger southward velocity along the LC axis is evident in EXP-H in all seasons, suggesting the significant impact of the horizontal resolution on the LC throughout the year.

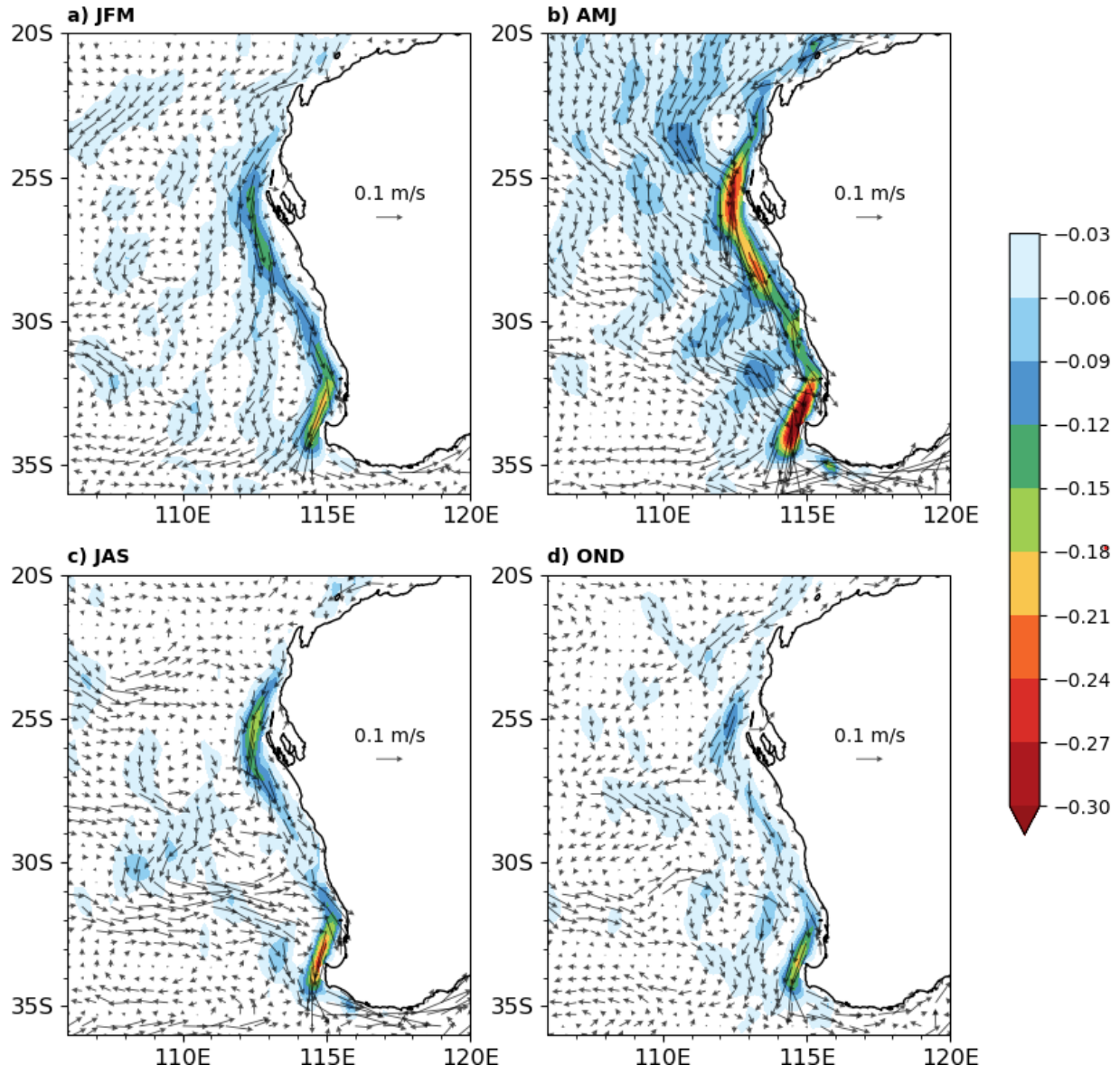

Figure 3.4. The upper 50 m mean velocity from EXP-L for (a) JFM, (b) AMJ, (c) JAS, and (d) OND.

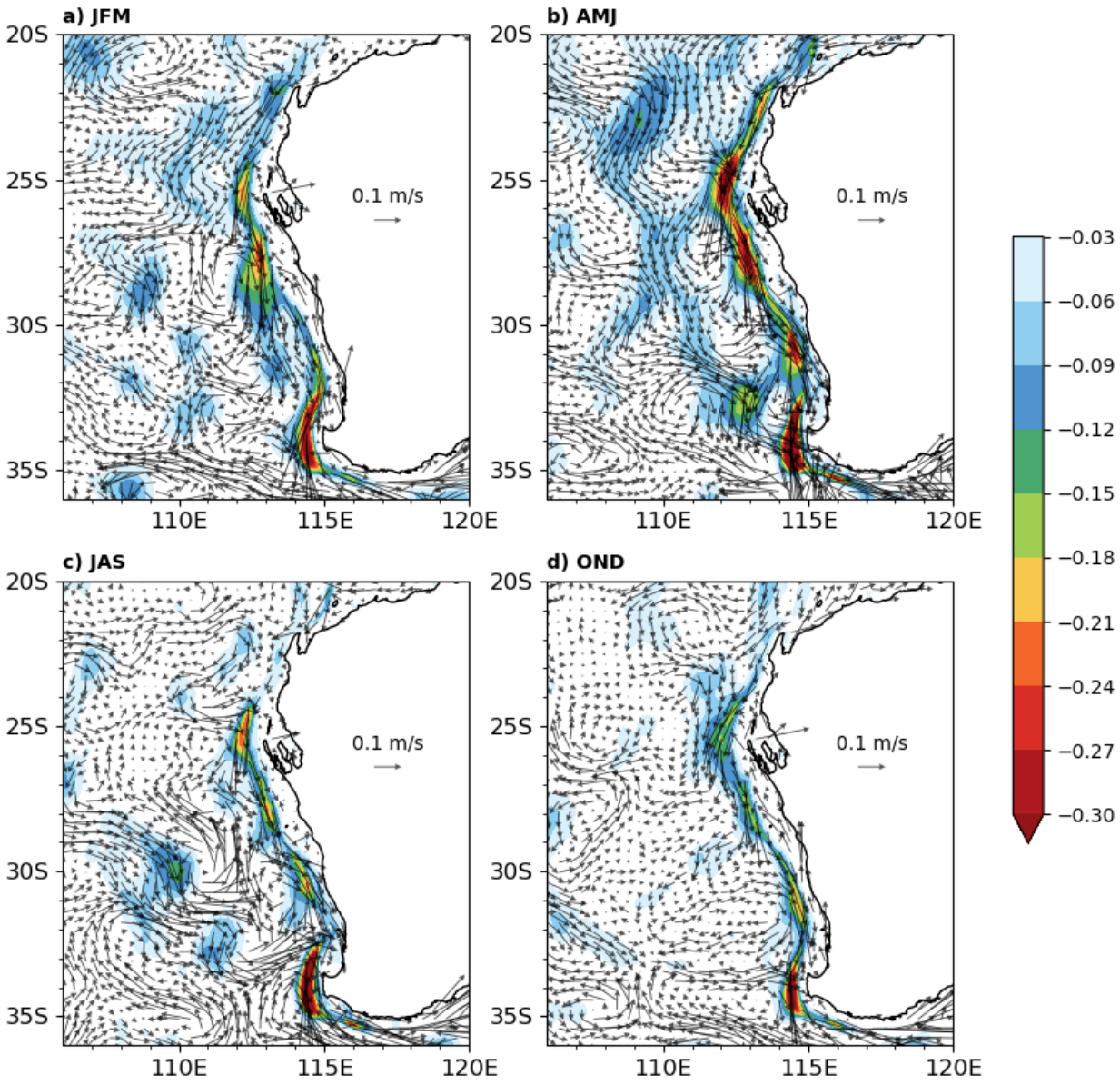

Figure 3.5. The upper 50 m mean velocity from EXP-H for (a) JFM, (b) AMJ, (c) JAS, and (d) OND.

To further evaluate the simulated LC in EXP-L and EXP-H, the volume transports of LC are compared in Figure 3.6. The transport is calculated by integrating the meridional velocity vertically from the surface to 300 m and zonally from the west boundary x_w to the east boundary x_e of the LC. The boundary of the LC is defined in two methods. In the first method (M1), x_w is

fixed to 110°E and x_e is the west coast of Australia (green line in Figure 3.2). The defined region is much wider than the LC width and may contain offshore recirculation. However, because the LC often deviates from its climatological axis, using a wider region is necessary. In the second method (M2), x_e is defined as the nearest longitudes of 120 m isobath, and x_w is 1.2° west of x_e, so that this region contains the LC only (red lines in Figure 3.2). The transport is calculated along each latitude from 22°S to 32°S, and then it is averaged over the latitude.

To compare with the observations, the LC transport at 32° (M1) is also shown in Figure 3.6. In EXP-L, the LC reaches its maximum southward transport of ~5.5 Sv at 32°S in May, which agrees well with previous observational studies (e.g., Feng et al. 2003; Furue et al. 2017). At the same latitude, EXP-H shows stronger LC transport in May-July than EXP-L, but weaker transport in April, September, and November. By taking the latitudinal average, the transport using M1 (red lines in Figure 3.6) does not show a significant difference between EXP-L and EXP-H, although larger transports are evident in EXP-H using M2 (blue lines in Figure 3.6), suggesting that the offshore recirculation may have compensated the stronger nearshore southward transport in EXP-H.

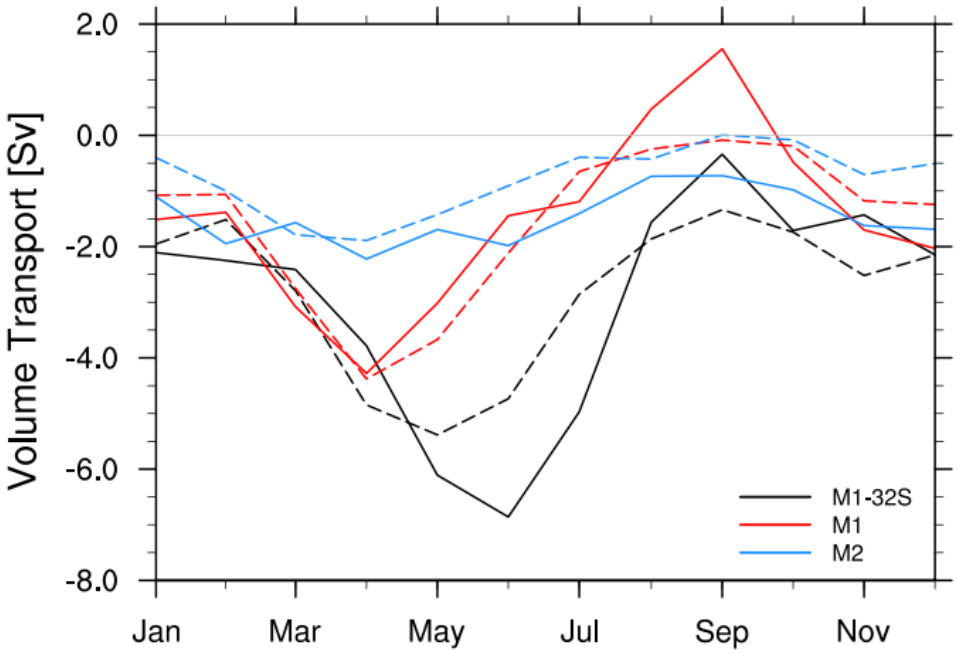

Figure 3.6. Annual cycle of the LC transport (Sv) from EXP-L (dashed lines) and EXP-H (solid lines). Negative values indicate southward transport. Black lines indicate the transport at 32°S across the LC section defined in M1. Red and blue lines are similar to the black line, but the transport is calculated across the LC section defined in M1 and M2 and averaged from 22°S to 32°S.

3.3.3 Impact of resolution on the 2010-2011 Ningaloo Niño

To evaluate the model performance in simulating the LC variability, the Fremantle Sea Level, which is an index for the strength of the LC, is obtained from the University of Hawaii Sea Level Center, and it is compared with model outputs. Figure 3.7 shows that the Fremantle Sea Level anomaly from EXP-L and EXP-H is well correlated with the tide gauge data with a correlation coefficient of 0.86 and 0.9, indicating the LC variability can be represented well in both experiments.

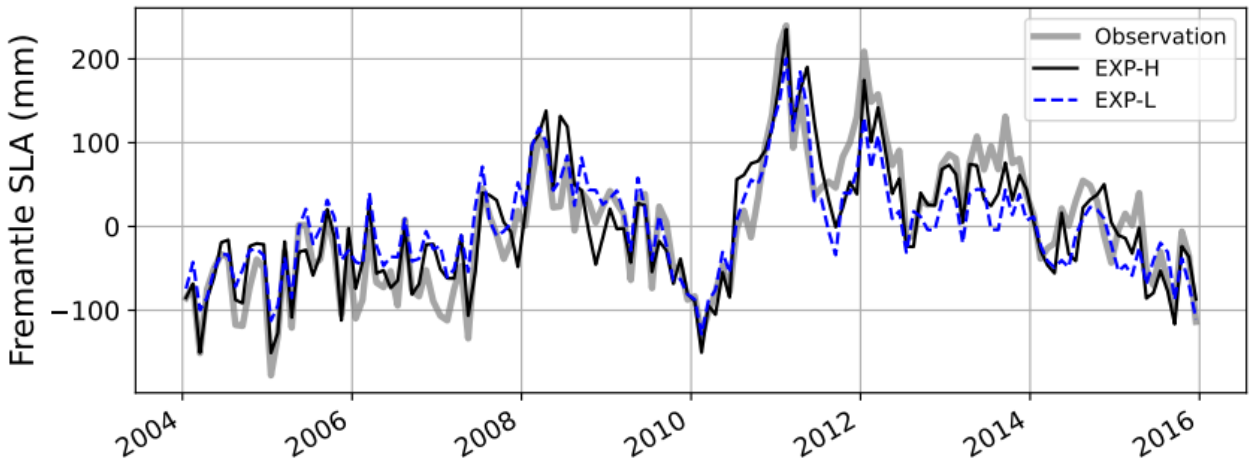

Figure 3.7. Monthly Fremantle Sea Level from EXP-L (blue dashed line), EXP-H (black solid line), and the observation (gray solid line).

To investigate the impact of model resolution on the LC variability during the extreme Ningaloo Niño event in 2010-2011, the upper 50 m meridional velocity averaged for the NNI region is shown in Figure 3.8. In EXP-L, the LC is enhanced rapidly from mid-2010 to September 2010. Since then, the southward velocity anomaly remains positive with small fluctuations until March 2011, after which the magnitude of anomalous velocity gradually decreases. Compared to EXP-L, substantial increases in the velocity anomaly are found in EXP-H, particularly around September 2010.

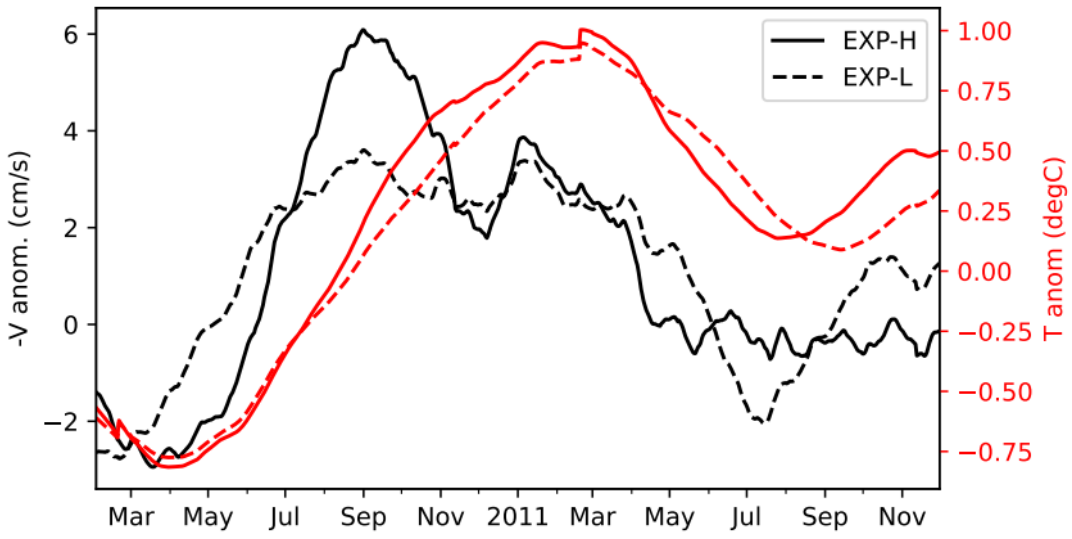

Figure 3.8. Upper 50m meridional velocity anomaly and temperature anomaly averaged for the NNI region (22-32°S,110-116°E). The data have been smoothed with a 100-day running mean filter.

Because the anomalous heat advection by the surge of LC plays an important role in the evolution of the 2010-2011 Ningaloo Niño, the increase in ocean model resolution could influence the development of upper ocean warming by changing the LC variability. The map of monthly SST anomaly from August 2010 to May 2011 is shown in Figure 3.9. In EXP-H, a warm SST anomaly has spread over a large region off the west coast of Australia in September 2010, while it is weaker and confined to an elongated area near the coast in EXP-L. In the peak phase, the positive SST anomaly from both experiments is largely trapped near the coast, and a smaller SST anomaly is found in EXP-L.

The time series of the upper 50 m ocean temperature anomaly from EXP-L and EXP-H shows that the warming anomaly begins to develop in July 2010 and peaks in late February and early March of 2011 (Figure 3.8). Consistent with Figure 3.9, larger warming anomalies are found in EXP-H during the developing phase when the enhancement of the LC is stronger. In

October-November 2010, the temperature anomaly in EXP-H is about 0.2°C (40 %) warmer than in EXP-L. The difference in temperature anomaly between EXP-L and EXP-H becomes smaller around the peak phase because of the small difference in the LC. But the warmer ocean temperature is observed for the entire developing and peak phase in EXP-H, which highlights the significant influence of the model resolution on the Ningaloo Niño simulation.

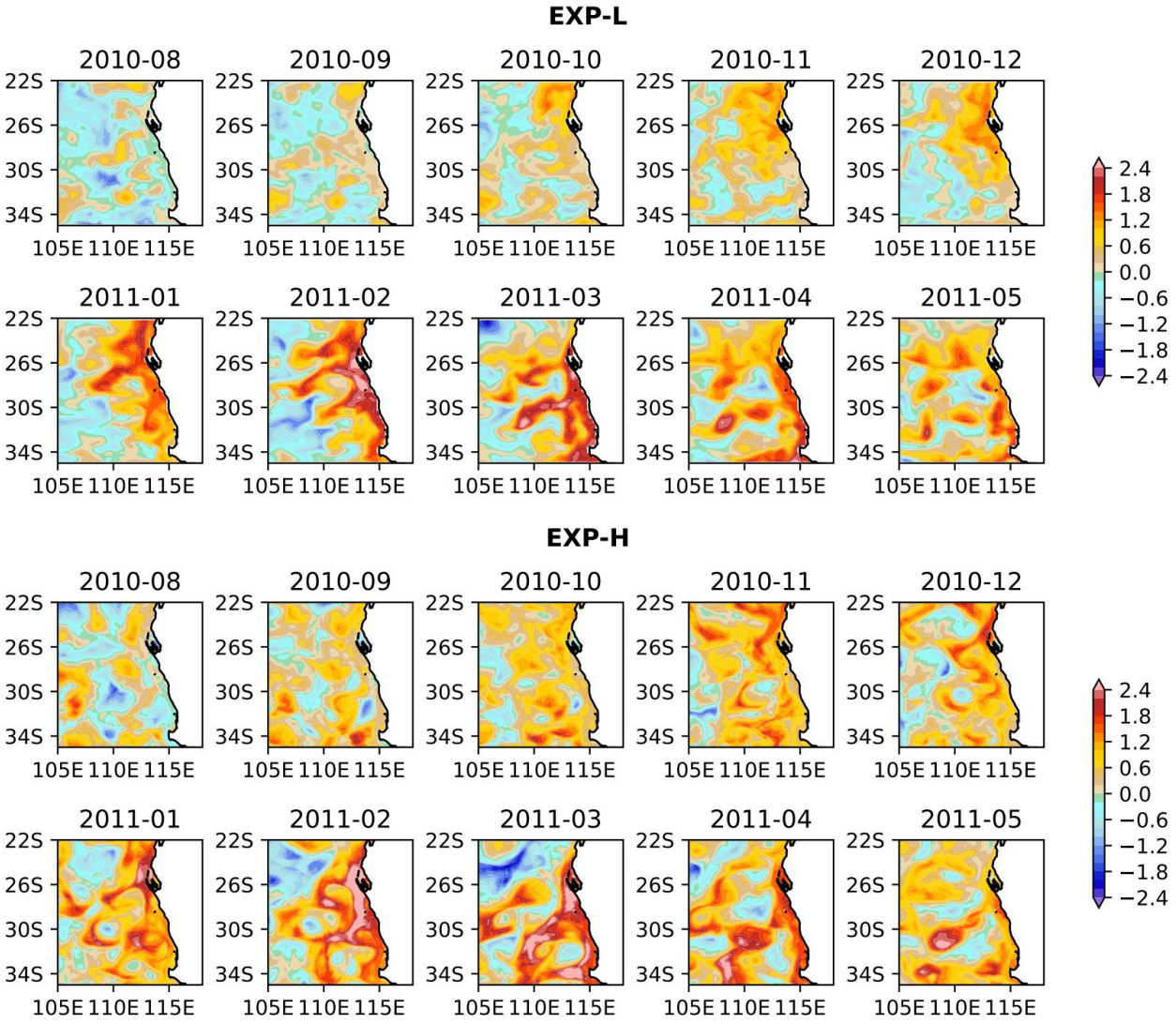

Figure 3.9. Monthly SST anomalies (°C) during the 2010-2011 Ningaloo Niño from EXP-L (upper panel) and EXP-H (lower panel).

3.4 Summary and discussion

In this study, the performance of an eddy-permitting (1/4°) and eddy-resolving (1/12°) Indo-Pacific domain OGCM in simulating the LC are evaluated. By comparing the outputs from the low-resolution model experiment (EXP-L) and the high-resolution model experiment (EXP-H), the impact of the model resolution on the LC and 2010-2011 Ningaloo Niño is quantified.

The mean and seasonal variability of the LC can be reproduced reasonably well in EXP-L, but EXP-H shows significant improvements in the magnitude and spatial structure of the annual mean LC due to the increased resolution. In addition, the zonal scale of the LC is better represented in EXP-H, and the current is well separated from the continental shelf and offshore circulation.

The seasonal variation of LC is simulated well in EXP-L and EXP-H. In EXP-H, the LC is stronger than in EXP-L in all seasons. The annual cycle of the LC transport is further investigated by integrating the southward velocity in the upper 300 m across the LC section defined in two methods. Results show that the difference in LC transport between EXP-L and EXP-H depends on the zonal scale over which the meridional velocity is integrated. There is no significant difference between EXP-L and EXP-H when a large zonal scale is used because of the recirculation outside of the LC region, while larger LC transport is found in EXP-H when a smaller zonal scale is used.

During the 2010-2011 Ningaloo Niño, a stronger enhancement of the LC is found in EXP-H than in EXP-L, and the magnitude of the regional average velocity anomaly is larger in

EXP-H than in EXP-L around September 2010 and January 2011. Because of the heat advection by the LC, EXP-H generates a warmer SST anomaly off the west coast of Australia for the entire developing and peak period. The results suggest that the high-resolution model simulates the LC variability and the spatial structures of surface warming better during the Ningaloo Niño.

The motivation of this work is to understand how the model resolution influences the simulation of LC and Ningaloo Niño. The results have provided evidence of various improvements in the LC simulation with enhanced resolution especially the increase the magnitude. The stronger LC in the eddy-resolving model could be due to multiple factors, including the resolved narrow width of the LC, the improved offshore and tropical inflows, and better-represented bottom topography. The recent ORAS5 reanalysis increased the ocean model resolution to 0.25°, but the strength of the LC is only weakly increased (not shown). Since the continental shelf and slope is important for generating realistic LC (Furue et al. 2013; Benthuysen et al. 2014b), unrealistic bottom topography near the west coast of Australia in ORAS5 may partly explain the weaker LC, and the impact of the continental shelf and slope on the LC variability and Ningaloo Niño needs to be carefully examined in future research. Lastly, since increasing the ocean model resolution in the ocean-only or coupled climate model require a substantial amount of computing time, the results of this study will provide useful guidance on the optimal allocation of computational resources in future modeling studies of the Ningaloo Niño.

CHAPTER IV: TOPOGRAPHIC TRAPPING OF THE LEEUWIN CURRENT AND ITS IMPACT ON THE NINGALOO NIÑO

4.1 Introduction

The Leeuwin Current (LC) is a narrow eastern boundary current flowing along the west coast of Australia (e.g., Cresswell and Golding 1980; Thompson 1984; Smith et al. 1991). Compared to other eastern boundary currents, it is unique in that the current flows poleward against the prevailing wind (e.g., Godfrey and Ridgway 1985; McCreary et al. 1986; Godfrey and Weaver 1991). Observations show that the average speed of the LC is about 30 cm s^{-1}, and the LC becomes stronger in austral autumn and winter, during which the speed exceeds 55 cm s^{-1} (Smith et al. 1991; Feng et al. 2003). The LC variability largely contributes to the southeast Indian Ocean heat balance because it advects warm waters from the tropics to the west coast of Australia, and thus it strongly impacts regional climate variability such as the Ningaloo Niño (Feng et al. 2013) and local biodiversity and fishery (Wernberg et al. 2013).

A prominent feature of the LC is that the strong current is coastally trapped near the shelf break, and the current is associated with a high sea level at the coast and a strong cross-shore pressure gradient. Hence, to maintain the strong LC, some physical processes must exist to prevent the high sea level along the coast from radiating offshore as Rossby waves. Several mechanisms have been proposed to explain the trapping of the LC along the coast. For example, Kundu and McCreary (1986) suggested that the Rossby waves are damped by vertical diffusion near the coast, and thus the high sea level cannot be radiated too far from the coast. However, the model required an unrealistically large vertical mixing coefficient to generate a coastally trapped LC, with an amplitude weaker than observations. Weaver and Middleton (1989, 1990) demonstrated that the continental shelf can provide a trapping mechanism. In their analytical

model, the ocean was represented by a two-layer system with a linear shelf profile at the eastern boundary. Given a fixed alongshore density gradient, the model generated a trapped current with realistic speed over the continental slope. The alongshore current cannot be formed without a continental slope due to the Rossby wave radiation. However, the speed of the LC largely depended on the bottom friction coefficient, and the assumption of $\beta=0$ in the shelf region eliminates the Rossby wave genesis. Hence the role of the continental shelf in LC trapping is still inconclusive in their study.

Recent studies by Furue et al. (2013) and Benthuysen et al. (2014b) examined the major coastal processes that are responsible for the coastal trapping of the LC in detail and showed that the presence of a continental slope is necessary to generate realistic LC strength and structure. In Furue et al. (2013), the linear model used by Weaver and Middleton (1989, 1990) was modified by including β with more realistic model layer formulations and neglecting mixing, bottom friction, and advection. The results demonstrated that the characteristic curves of Rossby waves bend southward in the coastal region due to the topographic beta effect, and thus the LC is trapped over the slope. Because there is no friction to damp Rossby waves in the model, the main factor that accounts for the trapping of the LC is the sloping bottom topography. Benthuysen et al. (2014b) obtained similar results using an idealized numerical model, which includes all the neglected processes in Furue et al. (2013). Without the shelf-slope topography, the simulated LC at equilibrium was about 2 cm s^{-1}, which is too weak compared with observations. By including the shelf and slope at the eastern boundary, the LC speed increased substantially to about 25 cm s^{-1}, demonstrating the important role of the continental shelf in maintaining the LC strength.

While the theoretical studies described above have provided sufficient evidence that the existence of continental shelf-slope is crucial for trapping and strengthening the LC, their results

are based on models with highly idealized shelf and forcings, Hence, it is difficult to determine to what extent the coastal topography affects the observed LC strength and variability. Accordingly, it is necessary to use models with realistic topography and forcings for isolating the effect of topography on the LC.

Since the LC strongly influences regional and global climate variability through the advection of warm waters from the tropics, the continental shelf and slope may play an important role in climate variability such as the Ningaloo Niño by changing the LC evolution. For example, during the 2010-2011 Ningaloo Niño event, the anomalous surface warming associated with a surge of the LC was observed in the coastal regions of Western Australia. The upper ocean warming peaked in February-March 2011 and the sea surface temperature (SST) in some regions was ~ 5 °C warmer than the climatological mean (Feng et al. 2013; Pearce and Feng 2013). By the end of 2010, large easterly anomalies in the equatorial Pacific Ocean, which is associated with the strong 2010-2011 La Niña, forced positive sea levels anomalies in the western Pacific Ocean. Because the sea level along the west coast of Australia is highly correlated with the western equatorial Pacific Ocean at one month lag (Feng et al. 2013), the remote Pacific forcing could accelerate the LC through oceanic wave propagation. In addition, negative sea level pressure dominated the southeast Indian Ocean during the peak phase. The associated northerly wind anomalies reduced the climatological southeast wind, thereby strengthening the LC. Hence the anomalous poleward heat advection caused by the enhanced LC plays a dominant role in the 2010-2011 Ningaloo Niño (Feng et al. 2013; Benthuysen et al. 2014a; Marshall et al. 2015).

Previous numerical modeling studies on the Ningaloo Niño have focused on the mechanisms for the development of anomalous ocean warming (e.g., Marshall et al. 2015; Kataoka et al. 2017; Zhang et al. 2018). However, detailed physical and dynamical processes that

are responsible for the LC enhancement during the Ningaloo Niño, including the role of the continental slope, are still unclear. Given the importance of remote forcing for Ningaloo Niño development, models with a larger domain that includes the Pacific Ocean basin are required to examine the role of the oceanic processes in the evolution of Ningaloo Niño.

In this study, a high-resolution Indo-Pacific basin Ocean General Circulation Model (OGCM) is used to evaluate and quantify the influences of the shelf-slope on the LC structures and strength. The sensitivity experiment is designed to isolate the effect of the bottom topography on the LC strength and variability. Also, the outputs of these experiments are further analyzed to investigate the role of the continental slope in the evolution of the Ningaloo Niño. While the major processes that cause ocean warming during the Ningaloo Niño vary from event to event (e.g., Marshall et al. 2015; Zhang et al. 2018; Feng and Shinoda 2019), the anomalous surge of LC plays a dominant role in the 2010-2011 extreme event (Feng et al. 2013; Benthuysen et al. 2014a). Hence, this study focuses on discussing the oceanic processes during the 2010-2011 Ningaloo Niño.

The rest of the paper is organized as follows. Section 4.2 introduces the OGCM experiments and data used in this study. Section 4.3 presents the model results including the effects of sloping topography on the LC, the analysis for the 2010-2011 Ningaloo Niño period, and the role of the continental shelf-slope in the evolution of Ningaloo Niño through changes in LC development. Finally, Section 4.4 provides a summary and discussion.

4.2 Model experiments and validation

4.2.1 OGCM experiments

The OGCM used in this study is the HYbrid Coordinate Ocean Model, version 2.2.98 (HYCOM; Bleck 2002). The model is configured on a Mercator grid from 10ºN to 55ºS and

10ºE to 67ºW, which covers the equatorial and south Indian and Pacific Oceans. The horizontal grid spacing is 1/12°. There are 40 layers in the vertical, among which 14 layers are set to hybrid z-sigma layers to better resolve the shelf and mixed layer processes and the layer thickness gradually increases from 1 m (top layer) to 8 m (layer 14). Relaxation boundary conditions are used at the north, south, and west boundaries. A sponge layer with 20 grid points is used, in which the model temperature and salinity are relaxed to Polar science center Hydrographic Climatology (PHC) 3.0 (Steele et al. 2001) with the relaxation time scale varying from 3 to 95 days. The bottom topography is adapted from the 30 second General Bathymetric Chart of the Oceans (GEBCO; Weatherall et al. 2015) with additional hand editing based on a combination of navigational charts and scientific literature (Metzger et al. 2010). Model experiment with these realistic bottom topographies is referred to as "*control*" experiment hereafter.

In addition to the *control* experiment, a sensitivity experiment with modified bottom topography has been conducted to isolate the effect of the continental shelf along the west coast of Australia on upper ocean processes. In the sensitivity experiment, the bottom topography near the west coast of Australia between 22ºS and 35ºS was replaced by a flat bottom at 2000 m and a vertical wall along the coastline. This experiment is referred to as "*no-shelf*" experiment hereafter. The bottom topography used in the *control* and *no-shelf* experiments is shown in Figure 4.1. The difference between the *control* and *no-shelf* experiments represents the influence of the continental shelf along the west coast of Australia on upper ocean variability, including the LC and its impact on SST near the coast.

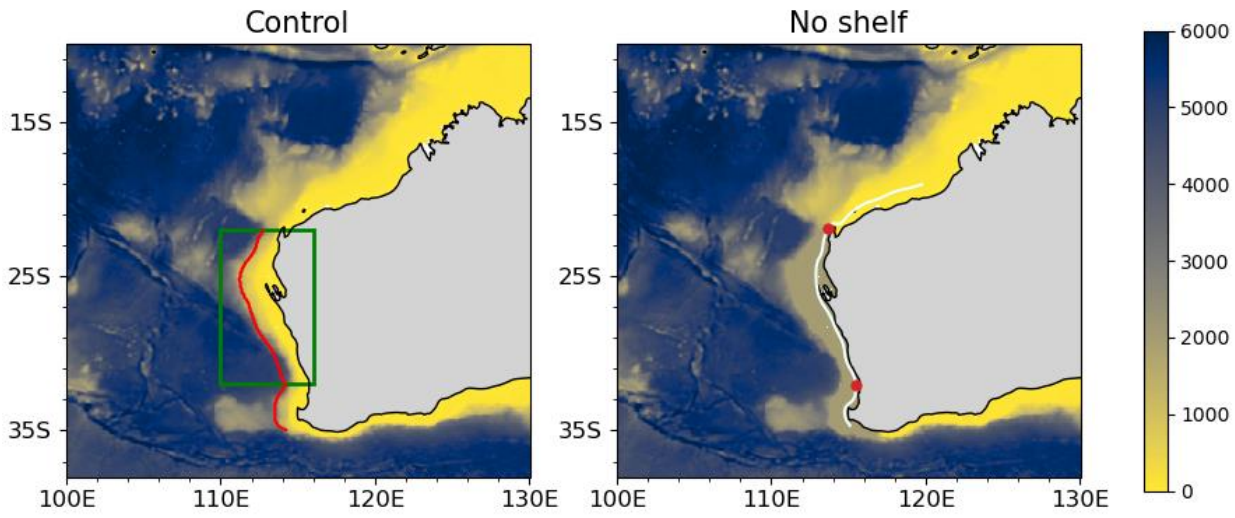

Figure 4.1. Bathymetry (meter) of the *control* and *no-shelf* experiment. The green rectangle indicates the box used for the NNI. The red line denotes the western edge of the LC. The white line shows the coastal waveguide used in Figure 4.11, and the red markers show the location of the reference lines in Figure 4.11.

Surface forcing fields derived from ERA5 reanalysis (Hersbach et al. 2018) are used in both the *control* and *no-shelf* experiments. Surface latent and sensible heat fluxes are computed using the CORE v2 bulk flux algorithm (Large and Yeager 2004). The air temperature (T_a) and specific humidity (q_a) at 2 m used in the bulk flux algorithm are calculated from the model SST using the following empirical formula:

$$T_a = SST - \Delta T$$
$$q_a = Rh * q_s(T_a) \quad (4.1)$$

where ΔT is the difference between SST and T_a, Rh is relativity humidity, and $q_s(T_a)$ is the saturation specific humidity at T_a. Monthly climatological values of ΔT and Rh at each location are estimated using SST, T_a and Rh from the WHOI Objectively Analyzed Ocean-Atmosphere Flux (OAFlux) product (Yu et al. 2008) for the period 1985-2016. In this manner, the SST is

freely evolved in response to the variation of oceanic processes such as the heat advection produced by LC variability. It should be noted that if the observed specific humidity (from reanalysis) is used in OGCM experiments, the model SST is very close to observations, especially in mid-latitudes where the mean winds are stronger than in the tropics (e.g., Seager et al. 1995; Shinoda and Lin 2009). In this case, the impact of LC variations on SST cannot be properly simulated and quantified by OGCM experiments.

The method described above was originally developed by Waliser and Graham (1993) in which ΔT and Rh are constant and thus appropriate for the tropics. Because of the spatially varying ΔT and Rh in Eq. (1), the method generates reasonable estimates of latent and sensible heat fluxes for larger domains including the southeast Indian Ocean. Yet the method is much more computationally efficient compared to other more complex formulations (Seager et al. 1995; Deremble et al. 2013). The reconstructed air humidity using Eq. (4.1) agrees well with those estimated by Deremble et al. (2013).

With the above configurations of surface forcing fields, the model was spun up for 20 years from a state of rest with monthly climatological forcing from ERA5 reanalysis. Then, the model is integrated forward from 2002 to 2015 with daily forcing fields from ERA5. The daily outputs for 2004-2015 are analyzed. The *control* and *no-shelf* experiments use identical surface forcing fields and thus only the difference in bottom topography is responsible for the difference in model results between the two experiments.

4.2.2 Data and analysis

Multiple SST products are used to describe the SST variations during the Ningaloo Niño and to compare with the *control* experiment. These are daily SSTs from the NOAA Optimum Interpolation (OI) Sea Surface Temperature (OISST v2) analysis (Reynolds et al. 2007) with the

0.25° resolution, the Operational Sea Surface Temperature and Sea Ice Analysis (OSTIA) with the 0.05° resolution (Donlon et al. 2012), the Multi-scale Ultra-high Resolution (MUR) product with the 0.01° resolution, the Remote Sensing Systems (REMSS) OI SST product with the 0.25° resolution, and monthly SST from Tropical Rainfall Measuring Mission (TRMM) Microwave Imager (TMI) with the 0.25° resolution.

The satellite altimetry data distributed by Archiving, Validation, and Interpretation of Satellite Oceanographic (AVISO) are used to investigate the sea surface height (SSH) variability in the southeast Indian Ocean. AVISO data with a horizontal resolution of 0.25°×0.25° for the period 2004-2015 are used.

The sea level at Fremantle (32.05ºS and 115.72ºE) measured by tide gauge is used as a proxy for the LC strength (Feng et al. 2003). The data for the period of 2004-2015, which are obtained from the University of Hawaii Sea Level Center, are used to validate the interannual variability of the simulated LC.

4.2.3 Validation

The monthly sea level anomaly at Fremantle from the *control* experiment is compared with observations (Figure 4.2). The simulated Fremantle Sea Level anomaly is highly correlated with the tidal gauge observation with a correlation coefficient of 0.90, indicating that the LC variability is realistically simulated in the *control* experiment.

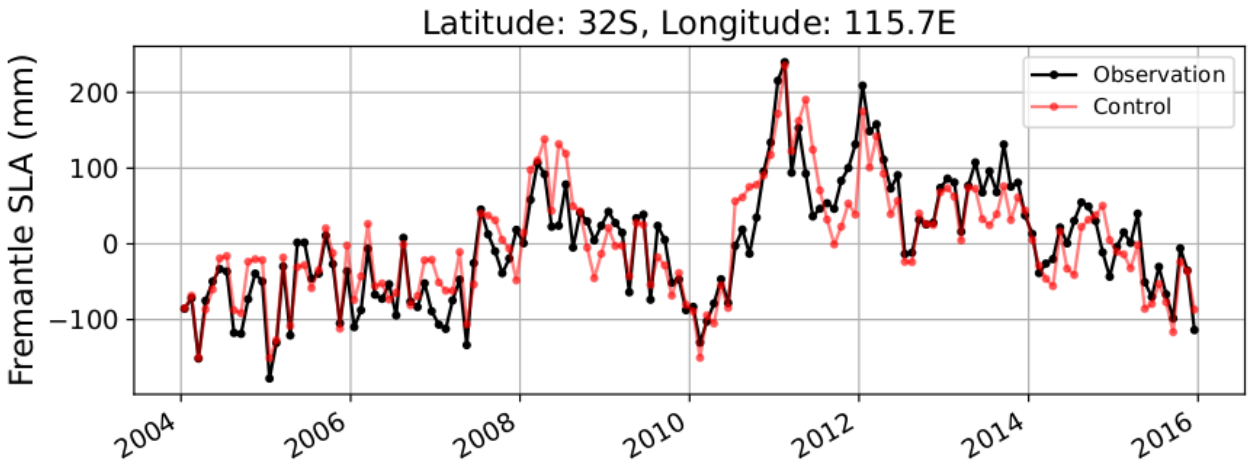

Figure 4.2. Monthly Fremantle Sea Level anomalies from the *control* experiment and the tide gauge observation. Values at the grid point closest to the tide gauge station in the model are used.

To evaluate the evolution of the 2010-2011 Ningaloo Niño in the *control* experiment, the Ningaloo Niño Index (NNI) derived from model outputs is compared with observations. Here the NNI is defined as the SST anomaly over the area 110°-116ºE, 22°-32ºS (box region in Figure 4.1). Figure 4.3 shows that the timing of the development and decay of ocean warming including its peak in the *control* experiment agrees well with observations. However, the SST anomaly around the peak in January-March 2011 is somewhat underestimated. Nevertheless, the substantial SST warming associated with the 2010-2011 Ningaloo Niño is well captured by the model, despite the specific humidity from the reanalysis is not used in the latent heat flux calculation. Note that the range of the peak values in January 2011 in different datasets exceeds 1°C, revealing the uncertainty of the observed SSTs, and the peak value of model SST is very close to one of the datasets (OSTIA, within 0.2 °C).

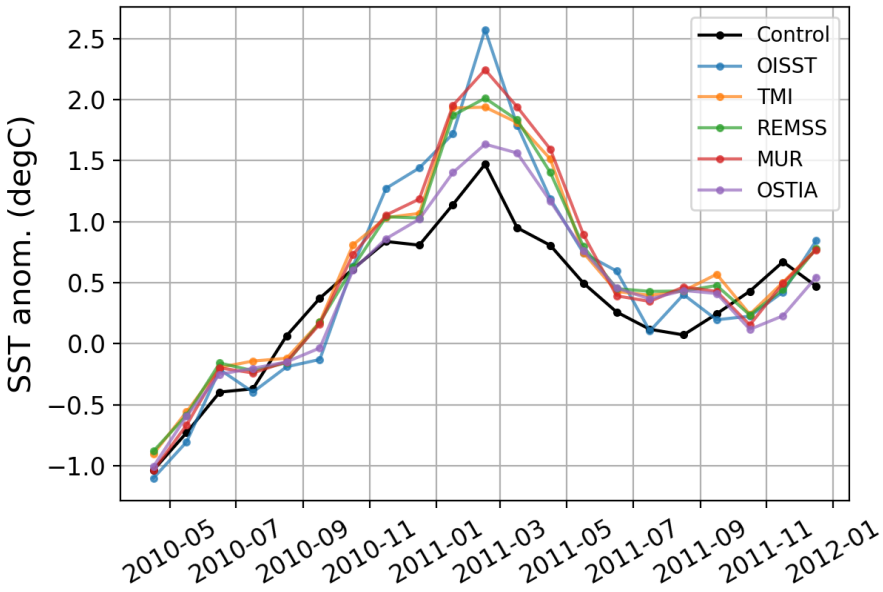

Figure 4.3. Monthly SST anomalies averaged over the NNI region during the 2010-2011 Ningaloo Niño.

4.3 Results

In this section, the mean and variability of the upper ocean including the LC in the *control* and *no-shelf* experiments are compared. Also, important oceanic processes, which cause the differences in the two experiments during the 2010-2011 Ningaloo Niño, are identified and discussed.

4.3.1 Structure of the Leeuwin Current

Figure 4.4 shows the average horizontal velocity over the upper 50 m for the period 2004-2015. Many features of the LC in the *control* experiment (Figure 4.4a) agree very well with observations (Feng et al. 2003; Furue et al. 2017). For example, the strong LC with the maximum southward velocity of about 20-30 cm s^{-1} is evident around 32°S and the core of the LC is aligned with the shelf break. The LC accelerates towards the south and turns eastward after passing Cape Leeuwin, extending along the south coast of Australia. Note that because of the

seasonal reversal of the current direction in the continental shelf region, the shelf current is not found in the annual mean in Figure 4.4a.

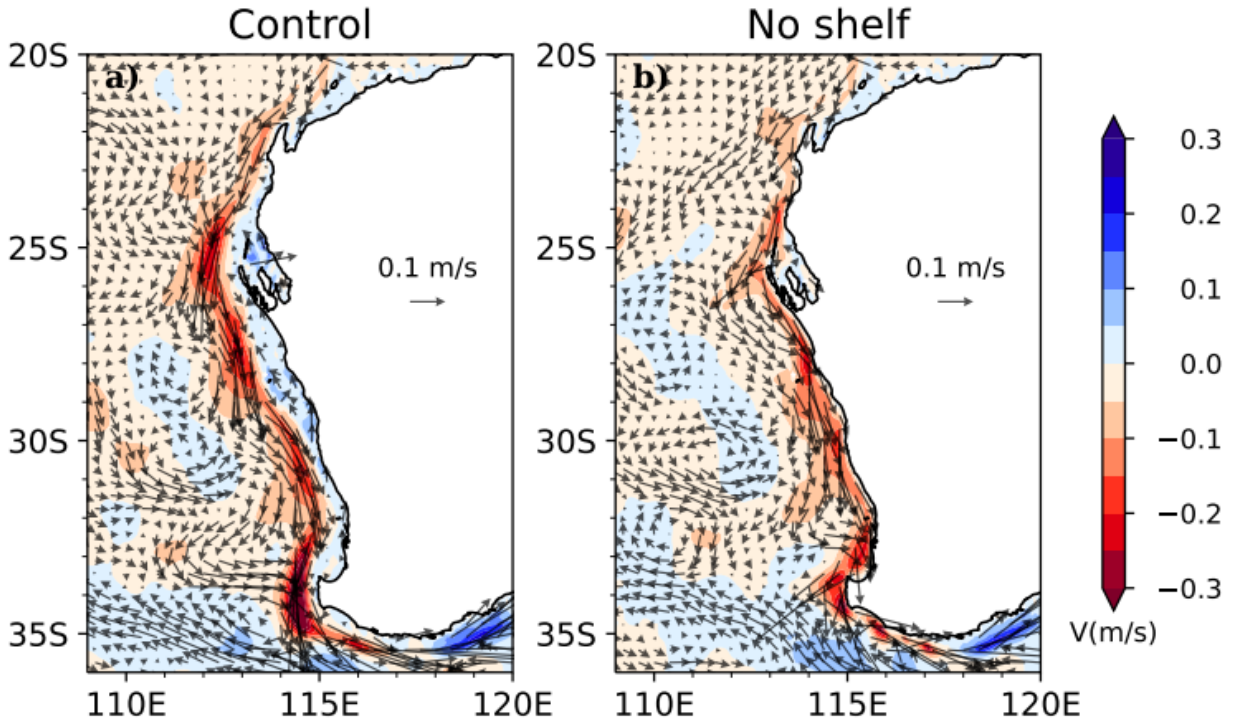

Figure 4.4. Mean current in the upper 50 m averaged for the period 2004-2015: (a) *Control*, (b) *No-shelf* experiment. Shading indicates the magnitude of meridional velocity.

In the *no-shelf* experiment (Figure 4.4b), the LC is much weaker and located closer to the coastline than in the *control* experiment. To further quantify the overall influence of the continental shelf on the LC, the average velocity in the large area (LC region) is calculated. Here, the western edge of the LC region is defined as the red line in Figure 4.1, and the meridional velocity at each latitude is shifted zonally so that the western edges at all latitudes coincide. Then the average values are calculated over the latitudinal range 22°-34ºS. The average

core velocity of LC is reduced by about 28% due to the absence of the continental shelf in the *no-shelf* experiment (Figure 4.5).

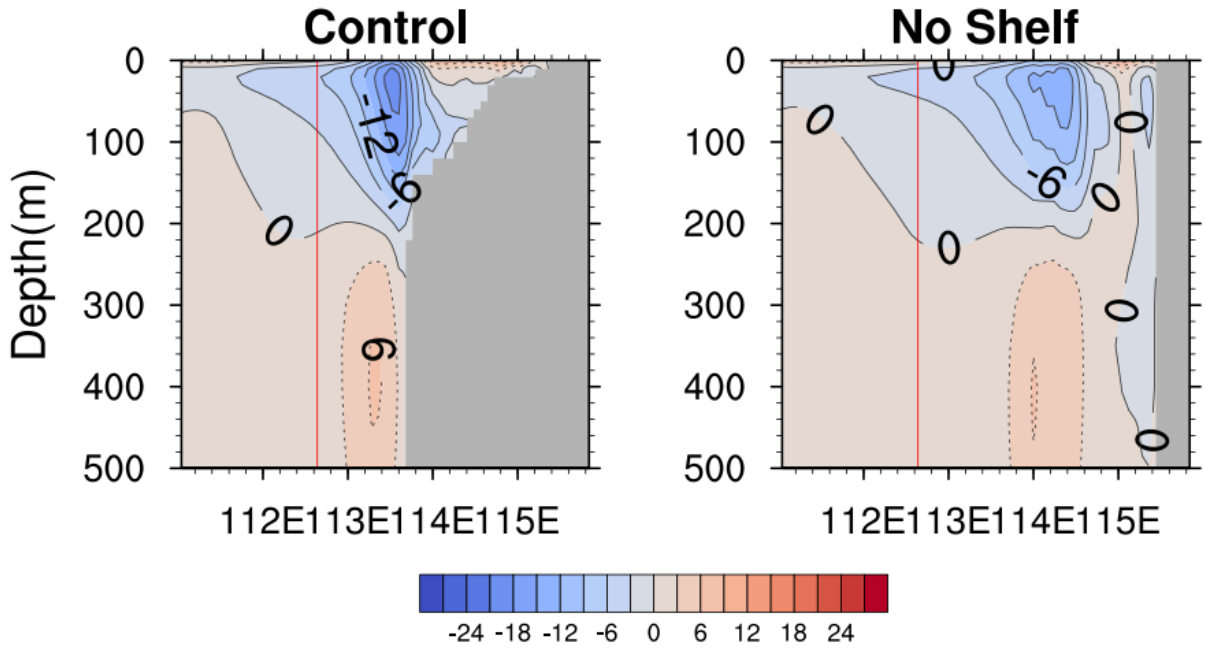

Figure 4.5. The composite of the meridional velocities (cm s^{-1}) averaged over 22°-34°S from the *control* (left panel) and *no-shelf* (right panel) experiments. The red lines denote the western edge of the LC.

Figure 4.6 shows the vertical structure of the LC at 22ºS, 26ºS, 30ºS, and 34ºS from the *control* and *no-shelf* experiments. In both experiments, the LC extends to a depth of 200 to 300 m, but a significant difference in the LC strength is observed, and the difference largely depends on the latitude. For example, the largest difference in the core velocity is found at 34ºS, where the speed is 44 cm s^{-1} in the *control* experiment and is 26 cm s^{-1} (41% weaker) in the *no-shelf* experiment. The core velocity is also significantly different at 22ºS and 26ºS, but the difference is not as large as the one at 34ºS. A reduction of 32% (27%) is found at 22ºS (26ºS) in the *no-shelf* experiment.

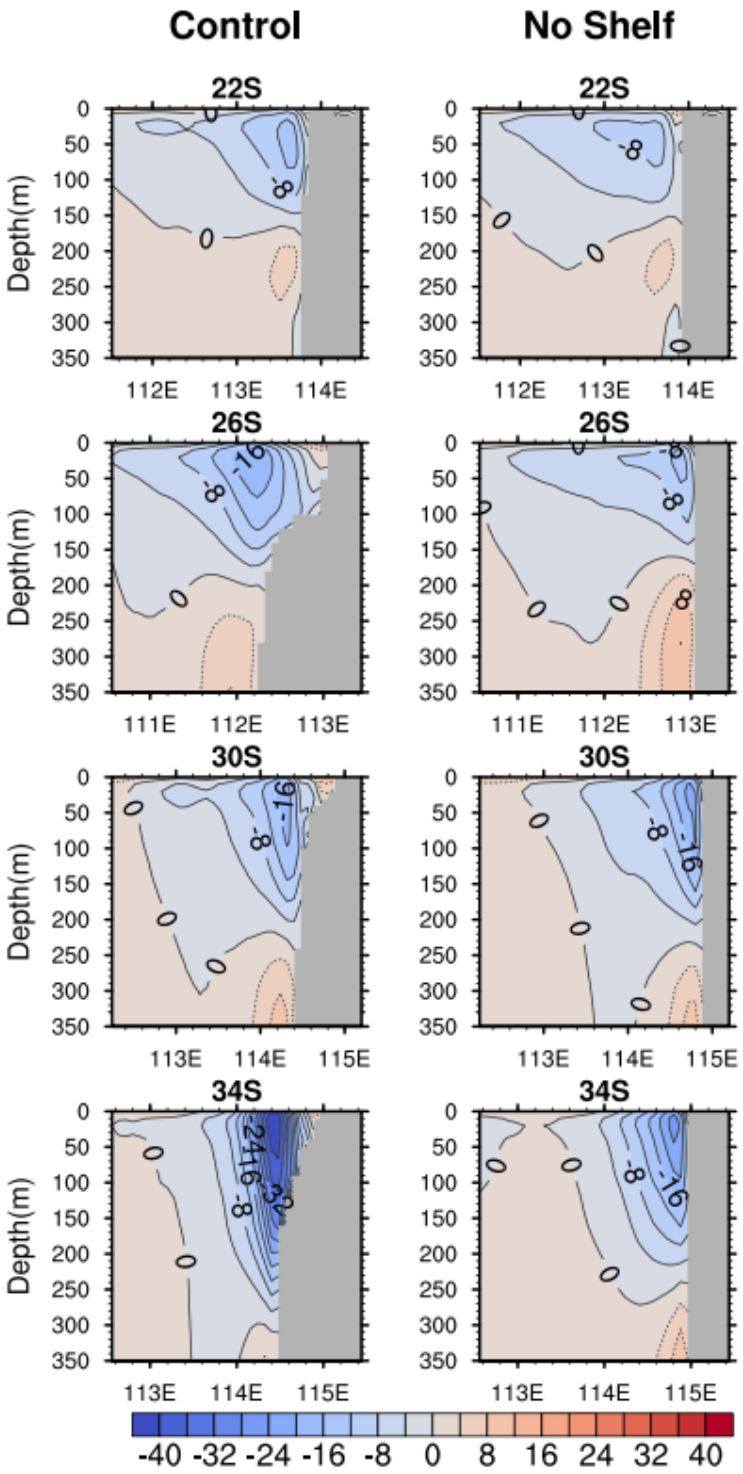

Figure 4.6. Vertical structure of the LC (cm s^{-1}) at different latitudes (22°S, 26°S, 30°S, 34°S) from the *control* (left panel) and *no-shelf* (right panel) experiments.

In summary, while the LC strength and location are well simulated in the *control* experiment, the LC in the *no-shelf* experiment is much weaker due to the lack of shelf-slope topography. The results highlight the importance of the topographic beta effect in the LC dynamics, which is consistent with the results from theoretical studies using idealized models (Furue et al. 2013; Benthuysen et al. 2014b). Yet the LC in our *no-shelf* experiment is much stronger than the no-shelf solution in Benthuysen et al. (2014b), suggesting that a variety of other processes may affect the generation and maintenance of the observed LC.

4.3.2 Evolution of the 2010-2011 Ningaloo Niño

The previous section demonstrates that the strength of the mean LC is largely affected by the continental shelf slope. Hence, large variations of the LC such as those observed during the 2010-2011 Ningaloo Niño may also be influenced by the continental shelf-slope. Since the 2010-2011 Ningaloo Niño is primarily driven by the heat advection associated with the anomalous LC (Feng et al. 2013; Benthuysen et al. 2014a), the sloping coastal topography could provide a prominent influence on the evolution of the extreme warming. In this section, we examine how the LC evolution during the 2010-2011 Ningaloo Niño is affected by the continental shelf-slope and to what extent the LC variability during the event influences the SST warming.

Because of high eddy activities near the west coast of Australia, a large meander of the LC is frequently found, and thus the location of the LC core often deviates from that of the mean LC, which reveals an alongshore jet trapped near the coast (Figure 4.4). Therefore, the LC variability is examined by using the southward velocity anomalies averaged in the NNI region. Figure 4.7 shows the time series of the upper 50 m LC anomaly during 2010-2011. The surge of the LC in mid-2010 occurs in both the *control* and *no-shelf* experiments. While the enhancement of the southward velocity anomaly in the *no-shelf* experiment lasts only about 2-3 months in

May-July 2010, the LC continues to grow in the *control* experiment and reaches its peak in September 2010. The anomalous LC in the *control* experiment during this peak is about three times stronger than that in the *no-shelf* experiment. After a short period of the LC decay in the *control* experiment around October-November, the velocity anomaly increases again in December 2010 and peaks around February 2011. Compared to the *control* experiment, the *no-shelf* experiment cannot produce prominent enhancements of the southward velocity anomaly during August 2010 – February 2011. The anomalous velocity is weaker than that in the *control* experiment during most of the warming period.

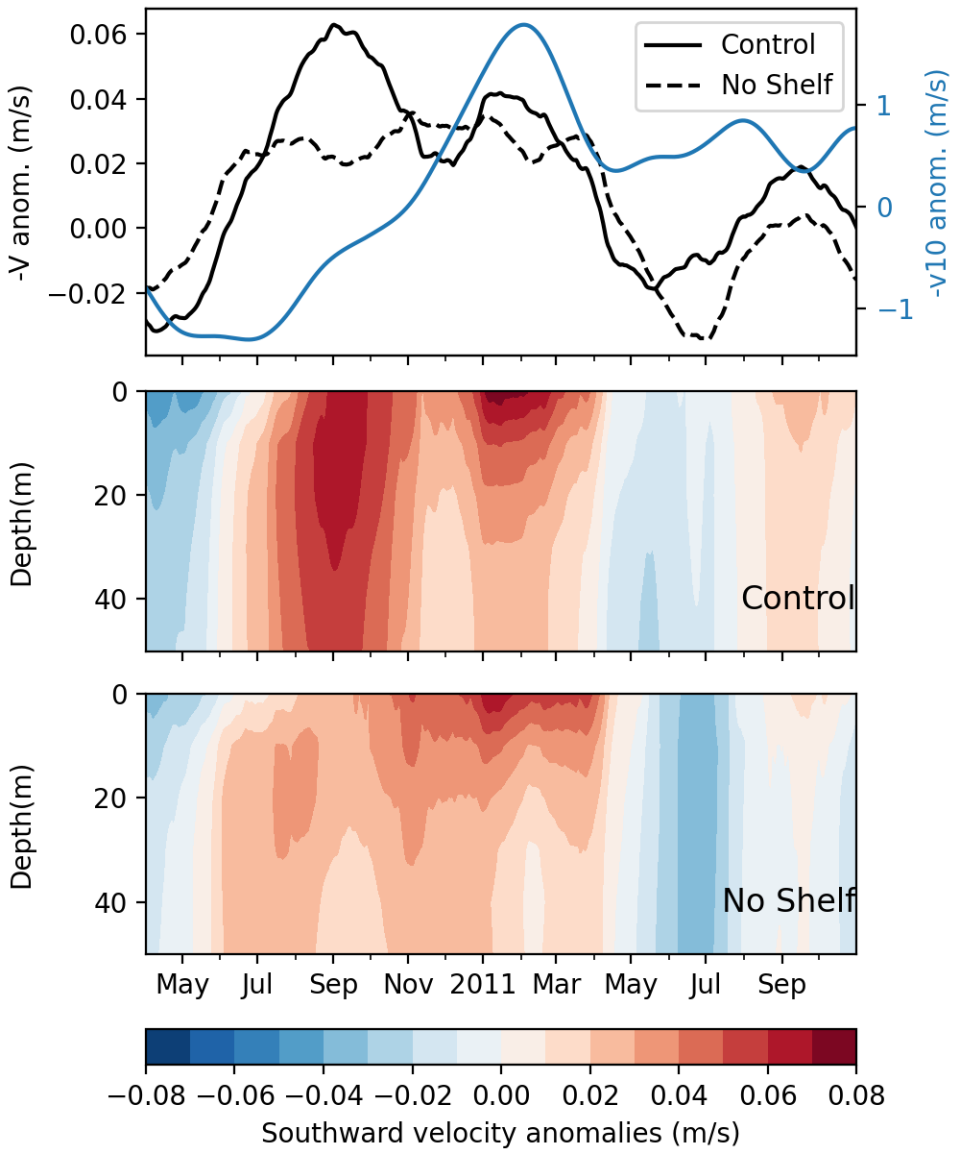

Figure 4.7. Top panel: Time series of average meridional velocity anomalies in the upper 50 m (black lines) from the *control* experiment (solid line) and *no-shelf* experiment (dashed line), and southward wind anomalies at 10 m (blue line). Middle panel: Southward velocity anomalies from the *control* experiment. Bottom panel: Same as the middle panel except for the *no-shelf* experiment. The data have been smoothed with a 100-day lowpass filter. All anomalies are averaged over the NNI box region.

The strengthening of the LC during August-October 2010 is not forced by local winds because southerly wind anomalies are still dominant in the southeast Indian Ocean (Figure 4.7. and Figure 4.8). Therefore, the enhancement of the LC during this period is likely attributed to remotely forced coastal waves. In contrast, the subsequent enhancement of the LC at the peak phase is due to the development of northerly wind anomalies along the coast (Figure 4.8).

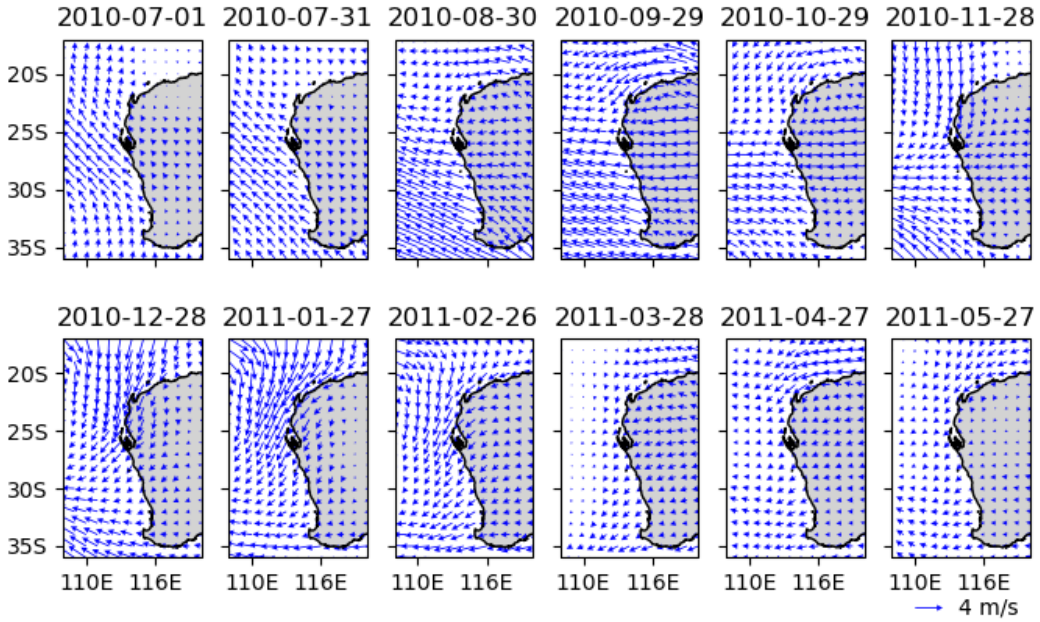

Figure 4.8. Daily wind anomalies at 10 m from ERA5. The data have been smoothed with a 100-day lowpass filter.

The vertical structure of the meridional velocity anomaly shows that the strong southward current in the *control* experiment extends through the upper 50 m, but the current is very weak below 30 m in the *no-shelf* experiment with a core located around 20 m. This suggests that the remotely forced component is very weak near the west coast of Australia when the continental shelf is absent. Because the LC surge at the peak phase is driven by local winds, both the *control*

and *no-shelf* experiments show relatively strong surface currents, but the currents in the *control* experiment are much stronger and extend deeper.

The evolution of simulated NNI from the *control* and *no-shelf* experiments is shown in Figure 4.9. The SST anomaly in the NNI region changes sign in August 2010, during which the LC speed increases sharply by remote oceanic processes. Because the LC is much weaker in the *no-shelf* experiment, the development of the anomalous ocean warming is delayed by about one month. By October 2010, the stronger LC in the *control* experiment causes a difference of about 0.5°C in the SST anomaly between the two experiments. Similarly, during the peak phase from January to March 2011, the anomalous SST in the *control* experiment is about 0.3 °C warmer than that in the *no-shelf* experiment. The close relationship between the LC enhancement and SST warming in the two experiments demonstrates the important role of the continental shelf-slope in SST variability associated with the Ningaloo Niño through the large enhancement of the LC. To further confirm the role of continental shelf and LC in the SST warming, the average SST anomaly for the LC region, which is from the coastline to its western edge (Figure 4.1), from 22ºS to 32ºS is also shown in Figure 4.9 (red lines). The SST anomaly in the *control* experiment is larger than that in the *no-shelf* experiment for almost the entire period of positive anomaly from August 2010 to May 2011.

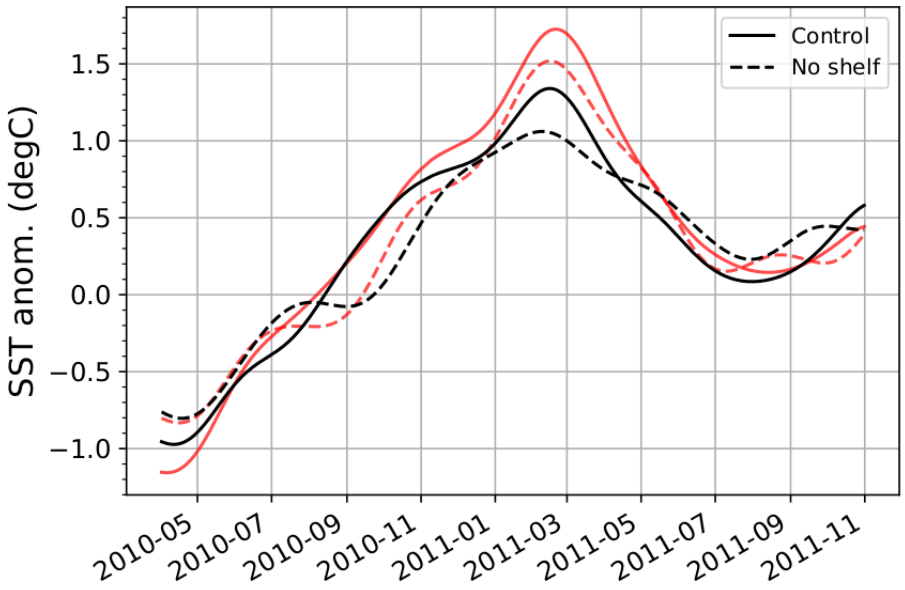

Figure 4.9. Time series of the SST anomalies over the NNI region (black lines) and the LC region between 22°-32°S (red lines). The data have been smoothed with a 100-day lowpass filter.

To explore the impact of the LC strength (and thus continental shelf) on the spatial pattern of ocean warming during the 2010-2011 Ningaloo Niño, maps of SST anomalies at a 30-day interval from September 2010 to April 2011 are shown in Figure 4.10. Here the SST anomalies are smoothed with a 100-day lowpass filter. In the *control* experiment, initial positive SST anomalies appear near the coast in early September. Much of the upper ocean warming is located near the coast during the entire period of the event while a portion of warm anomalies spreads to the interior ocean by eddies and lateral mixings. During the peak phase, warm water extends southward, and the entire LC region is covered by large SST anomalies. In the *no-shelf* experiment, warming anomalies initially develop near the coast, but they tend to propagate westward during the development stage. From January to March 2011, coastal warming is still able to grow due to the wind forced LC surge, but the magnitude of the warming is reduced

because of the offshore propagation. Physical processes associated with the offshore propagation of SST anomalies will be further discussed in Section 4.3.3.

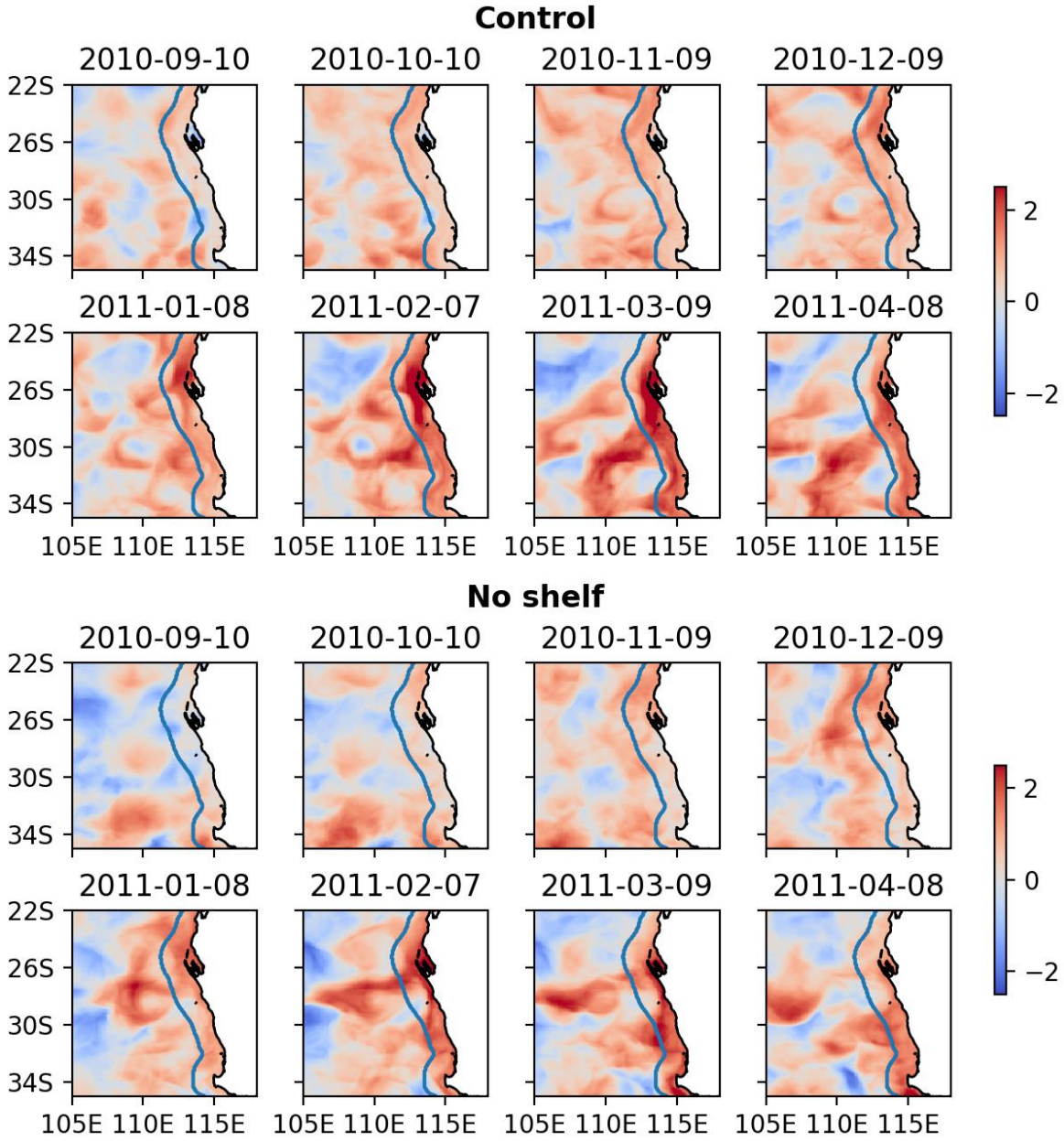

Figure 4.10. SST anomalies (°C) during the 2010-2011 Ningaloo Niño from the *control* (upper panel) and *no-shelf* (lower panel) experiments. The data have been smoothed with a 100-day lowpass filter. Blue lines denote the western edge of the LC (Figure 4.1).

To further quantify the impact of LC enhancement induced by the topography on the Ningaloo Niño development, a heat budget analysis in the upper ocean for the NNI regions is conducted (Figure 4.11). Terms in the temperature equation are integrated from the surface down to 50 m, then integrated for a month by the following equation:

$$\frac{1}{H}\iint_{H}^{0}\frac{\partial T}{\partial t}\,dz\,dt = \int\frac{Q_{net}}{\rho c_p H}\,dt - \frac{1}{H}\iint_{H}^{0}\boldsymbol{V}\cdot\Delta T\,dz\,dt + res \qquad (4.2)$$

where T is temperature, Q_{net} is the net air-sea heat flux, H is 50 m, $\boldsymbol{V}$ is horizontal velocity vector, ρ is the density of seawater, and c_p is the specific heat of seawater. The first and second terms on the right-hand side of Eq. (4.2) represent the change of temperature due to surface heat fluxes and the horizontal heat advection. The residual term includes the contributions from vertical advection, lateral and vertical mixings. All data used in the analysis are smoothed with a 100-day running mean. The anomalies from the monthly climatology are shown in Figure 4.11.

Consistent with previous studies (e.g., Marshall et al. 2015), the anomalous warming in the 2010-2011 Ningaloo Niño is primarily caused by the horizontal heat advection, which is evident in both the *control* and *no-shelf* experiments. The maximum heating rate occurs around September 2010, which is about 0.5 °C month^{-1} in the *control* experiment, and it is weaker in the *no-shelf* experiment, ~0.4 °C month^{-1} (Figure 4.11c). Large differences are found in the meridional heat advection. In the *control* experiment, positive meridional heat advection gradually increases since July, peaks in December 2010, and becomes negative in March 2011 (Figure 4.11d). In the *no-shelf* experiment, it stays positive for only three months (October-December 2010). The zonal heat advection, in contrast, stays positive during the entire warming event (Figure 4.11e), partly compensating the reduced meridional heat advection. Figure 4.11f shows that the anomalous warming due to zonal heat advection in the *no-shelf* experiment is

mainly caused by $u'T'_x$, which includes the contribution from the Rossby waves and mesoscale eddies. Since the zonal heat advection in the *control* experiment is smaller than that in the *no-shelf* experiment, the warmer upper ocean temperature (Figure 4.11a) is largely due to the difference in meridional heat advection. From September 2010 to March 2011, the average temperature anomaly is 0.79 °C for the *control* experiment and 0.58°C for the *no-shelf* experiment, which is about a 26% reduction.

The net surface heat flux anomaly is negative in both experiments (Figure 4.11b), and thus it does not contribute to the warming. Some previous studies suggest that the air-sea heat flux could partly contribute to the warming at the peak phase of the 2010-2011 Ningaloo Niño (e.g., Feng et al., 2013; Marshall et al., 2015). However, the air-sea flux estimates in this region vary substantially with different datasets (Feng and Shinoda 2019), and thus the relative contributions of air-sea flux and LC-induced heat advection have uncertainties. The errors stemming from the air-sea flux formulation in the experiments might be partly responsible for the discrepancies between this study and previous estimates.

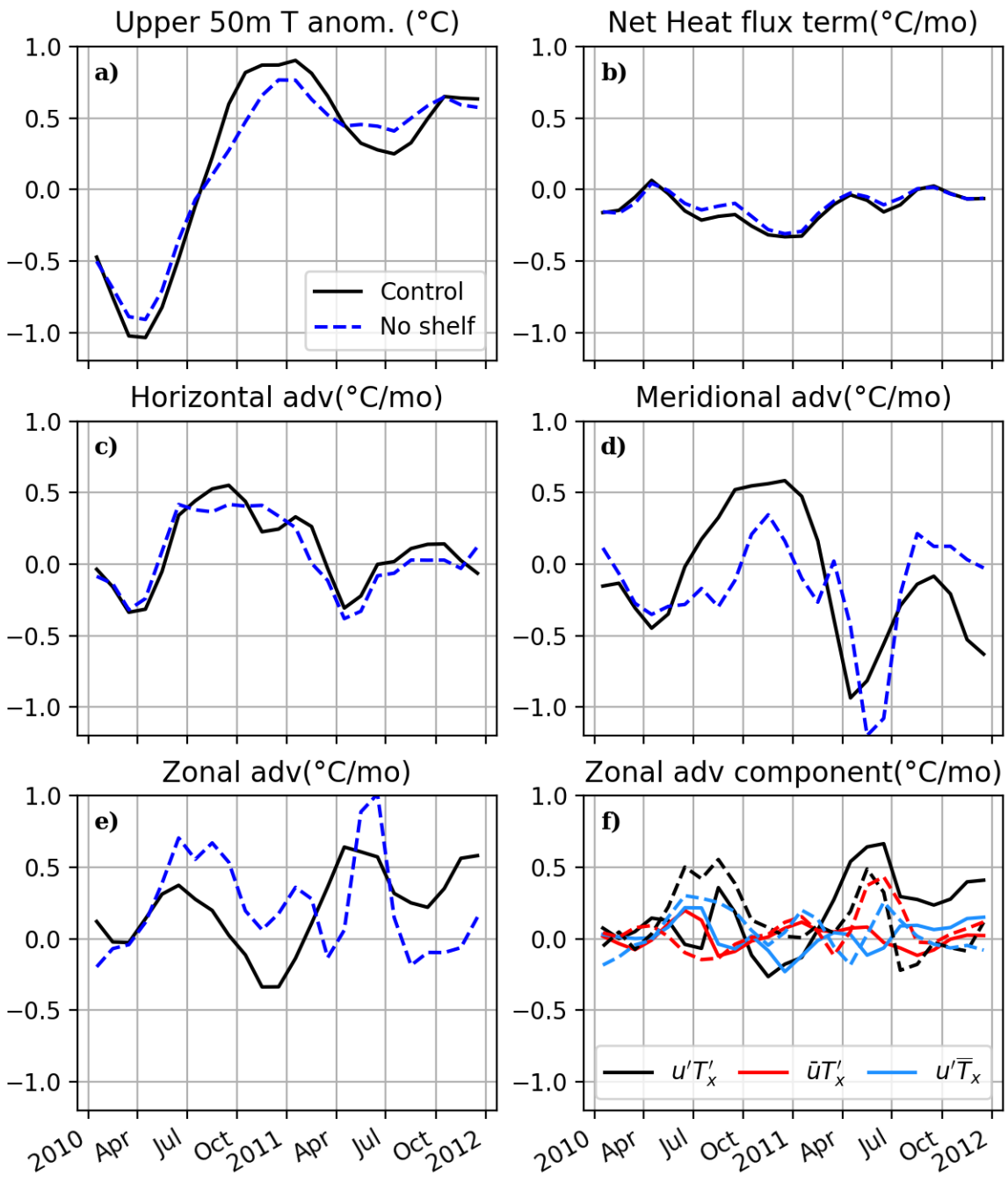

Figure 4.11. Anomalous heat budget terms averaged over the NNI region. The data have been smoothed with a 100-day running mean filter. The solid lines represent the *control* experiment and dashed lines represent the *no-shelf* experiment.

4.3.3 Physical processes: Role of the continental shelf on the Ningaloo Niño development

The oceanic processes relevant to the role of the continental shelf-slope on the LC variability and their impact on Ningaloo Niño development are discussed in this section. The analysis in Section 4.3.2 suggests that the strengthening of the LC in July-October 2010 is likely caused by the coastal trapped waves which are originated from the remote region. To detect the coastal trapped waves, SSH anomalies along the coast in the two experiments are analyzed.

Figure 4.12 shows SSH anomalies along the west coast of Australia during the 2010-2011 Ningaloo Niño. The SSH anomalies are smoothed with a 100-day lowpass filter to remove the subseasonal and shorter time scale variability. In the *control* experiment, positive SSH anomalies propagate from the northwest to the west coast of Australia in July-October 2010 (Figure 4.12a), in which the phase speed is consistent with the coastal trapped wave theory (Wang and Mooers 1976; Huthnance 1978; Brink 1991). Note that the local wind anomalies near the coast during this period change from southeasterlies to easterlies, and thus they cannot generate coastal sea level rise (Figure 4.8). Following these sea level rise events along the coast, coastal trapped waves are detected during the peak phase in January-February 2011 (Figure 4.12b). During this period, northerly wind anomalies dominate the west coast of Australia (Figure 4.8). Such wind anomalies cause Ekman convergence at the boundary, thereby initiating subsequent coastal trapped waves. Accordingly, the positive SSH anomalies are further enhanced and extended southward in association with the propagation of coastal trapped waves. It should be noted that from late August to early October, coastal trapped waves with higher frequencies, which are not shown in the filtered anomalies, are evident and they may also impact the longer time scale variability (not shown).

In the *no-shelf* experiment, the propagation of SSH anomalies along the coast is also evident. However, the amplitude and the propagation speed are different from those in the *control* experiment. During the developing period in July-October 2010, positive sea level anomalies at the northwest shelf propagate southward as coastal Kelvin waves, with the amplitude decaying quickly at the west coast. During the peak phase in January-February 2011, positive SSH anomalies generated by local winds are present along the coast, but the amplitude is smaller than that in the *control* experiment. The presence of continental shelf in the *control* experiment allows the SSH fluctuation along the coast to be effectively trapped over the continental slope through the propagation of coastal trapped waves. Without such sloping bottom topography, coastal Kelvin waves are not able to trap the anomalous sea level at the coast and thus the SSH anomalies along the coast are weaker in the *no-shelf* experiment.

(a)

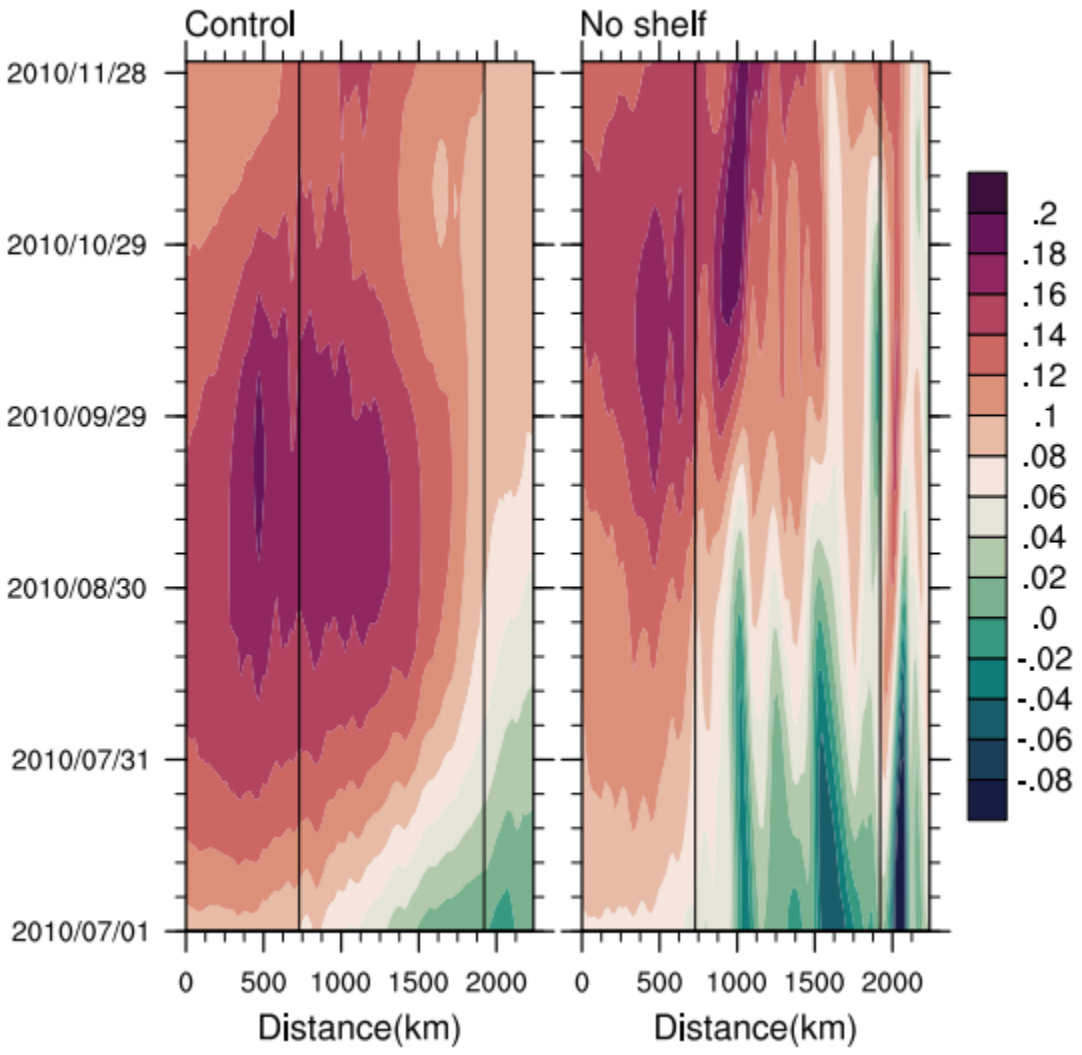
Control
No shelf
2010/11/28
2010/10/29
2010/09/29
2010/08/30
2010/07/31
2010/07/01
0
500
1000
1500
2000
Distance(km)
.2
.18
.16
.14
.12
.1
.08
.06
.04
.02
.0
-.02
-.04
-.06
-.08

(b)

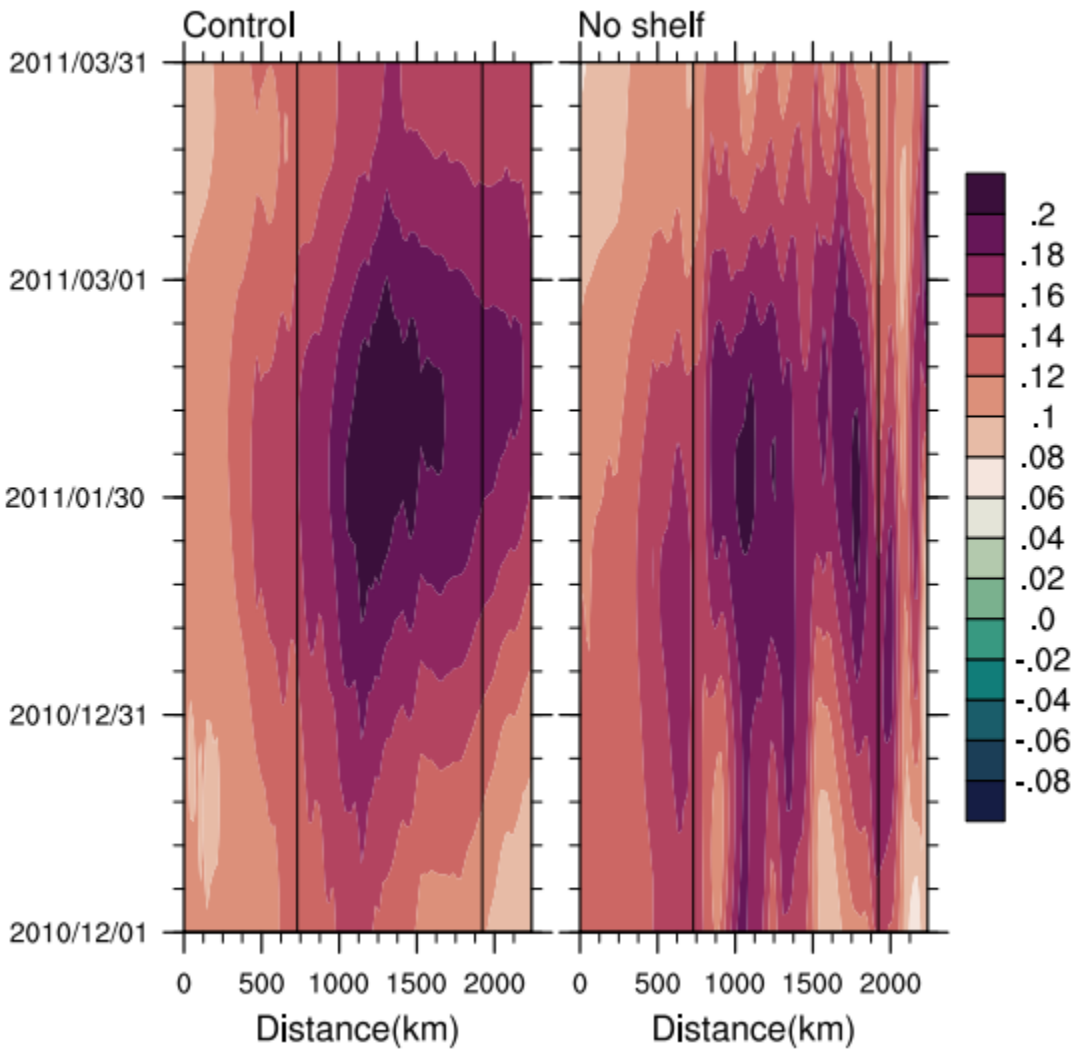

Figure 4.12. Lowpass filtered SSH anomalies (m) along the coastal waveguide (see Figure 4.1) from the *control* and *no-shelf* experiments during (a) July-November 2010, (b) December 2010-March 2011. The black lines indicate the locations of 22°S and 32°S.

The analysis described above clearly demonstrates that the continental shelf-slope plays an essential role in trapping the high sea level at the coast. Without a continental shelf-slope, the high sea level signals will radiate offshore as Rossby waves. To detect the Rossby wave

radiation, daily SSH anomalies from the *control* and *no-shelf* experiments are compared and shown in Figure 4.13. Because mesoscale eddies are active off the western Australian coast (Morrow et al. 2004; Feng et al. 2005), the signal of eddies is removed by a spatial filter to isolate large-scale ocean circulation and variability including Rossby waves. Following Delman et al. (2018), an error function based spatial lowpass filter is applied to the daily SSH anomaly. The filter with the cutoff wavenumber of 7° wavelength is applied in the wavenumber domain in both zonal and meridional directions. Then, the same filter with the cutoff frequency of 100 days is applied in the time domain to remove shorter time scale signals. The resulting SSH anomaly is shown in Figure 4.13 at an interval of 30 days.

Consistent with Figure 4.12a, the southward propagation of the high sea level anomalies associated with coastal trapped waves during the developing period (August-November 2010) is evident in the *control* experiment (Figure 4.13). Note that the high SSH anomalies along the coast are found in wider areas than the LC scale because of the use of the spatial filter. The high sea level along the coast generates a large cross-shore pressure gradient associated with the strong LC. In the *no-shelf* experiment, the spatial distribution of SSH anomaly reveals a smaller sea level rise in the nearshore region and more pronounced westward propagation from the coast. Because of the absence of trapping mechanism due to the continental shelf-slope in the *no-shelf* experiment, the signals of SSH anomaly at the coast radiate offshore as Rossby waves. Hence a lack of continental shelf-slope leads to a smaller sea level anomaly along the west coast and a weaker LC in the *no-shelf* experiment (Figure 4.7).

In January 2011, the relatively high coastal sea level anomalies in response to the northerly wind anomalies are present in both experiments. While SSH anomalies in the *control* experiment remain trapped near the coast from February to March 2011, they radiate offshore as

Rossby waves in the *no-shelf* experiment, resulting in smaller SSH anomalies at the coast. Therefore, the surge of the LC during the peak phase is weaker in the *no-shelf* experiment.

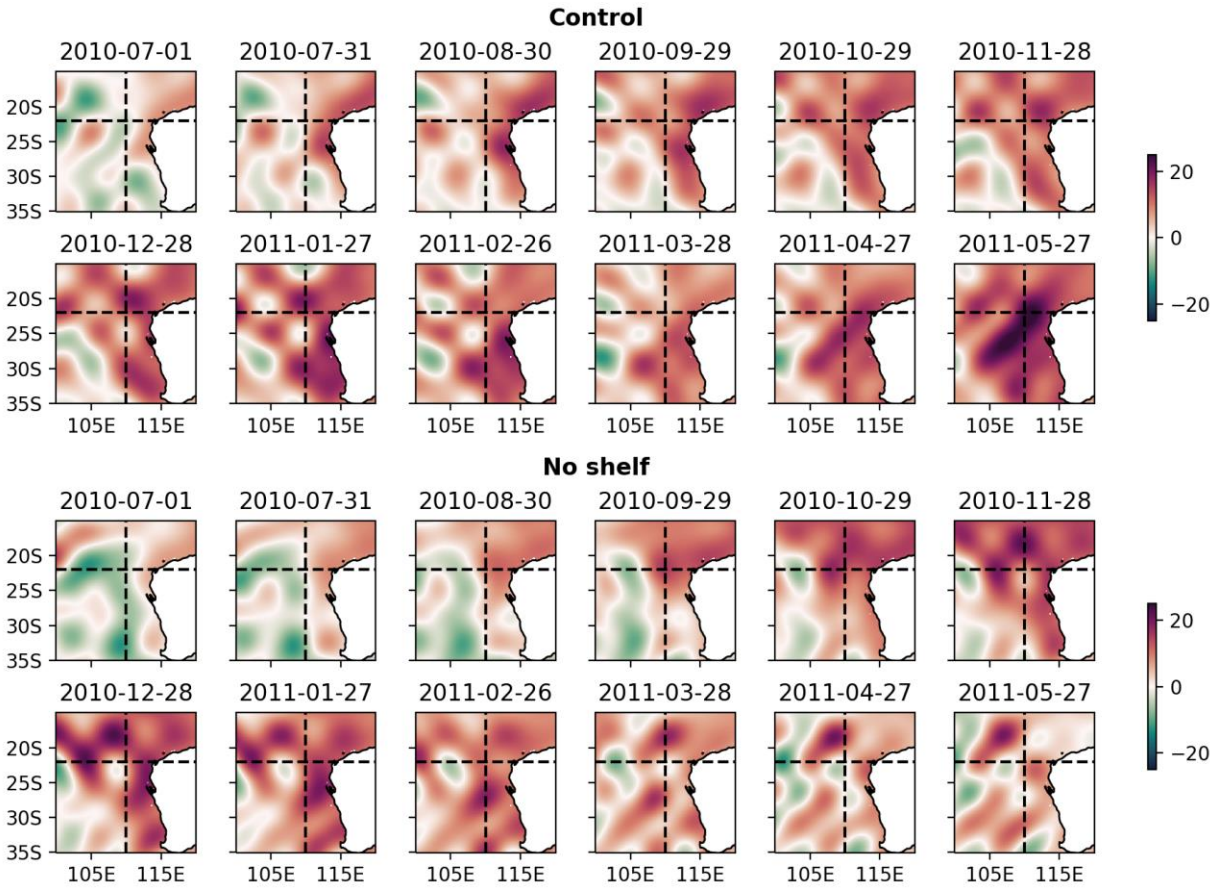

Figure 4.13. SSH anomalies (cm) from the *control* (upper panel) and *no-shelf* (lower panel) experiments. The data have been spatially and temporally filtered. Horizontal dashed lines denote 22°S and vertical dashed lines denote 110°E.

Hovmöller diagrams of SSH anomalies between 22°-32ºS from the model experiments and observations for the period 2011-2014 are shown in Figure 4.14 to further examine the westward propagation of the Rossby waves from the coast. During the 2010-2011 Ningaloo Niño, SSH anomalies in the *control* experiment and observations are trapped near the coast, and

positive SSH anomalies are mostly confined east of 110ºE. On the other hand, the westward propagation of SSH disturbances with a phase speed of about 5 cm s^{-1} is evident west of 110ºE in the *no-shelf* experiment, which is consistent with the first baroclinic Rossby wave speed around these latitudes (Chelton and Schlax 1996).

Similar differences in SSH anomalies are also found during the 2011-2012 Ningaloo Niño. For the 2012-2013 Ningaloo Niño, however, the sea level rise along the west coast of Australia is smaller and the trapping of positive SSH anomalies is less obvious. This is because the maximum warming occurred near northwestern Australia north of 22ºS in this event (Xu et al. 2018), and the LC enhancement is smaller than in the previous two warming events. Nevertheless, the westward propagation of Rossby waves is evident in the *no-shelf* experiment throughout the year, suggesting the considerable influence of continental shelf-slope on the overall ocean variability around Western Australia for a longer period.

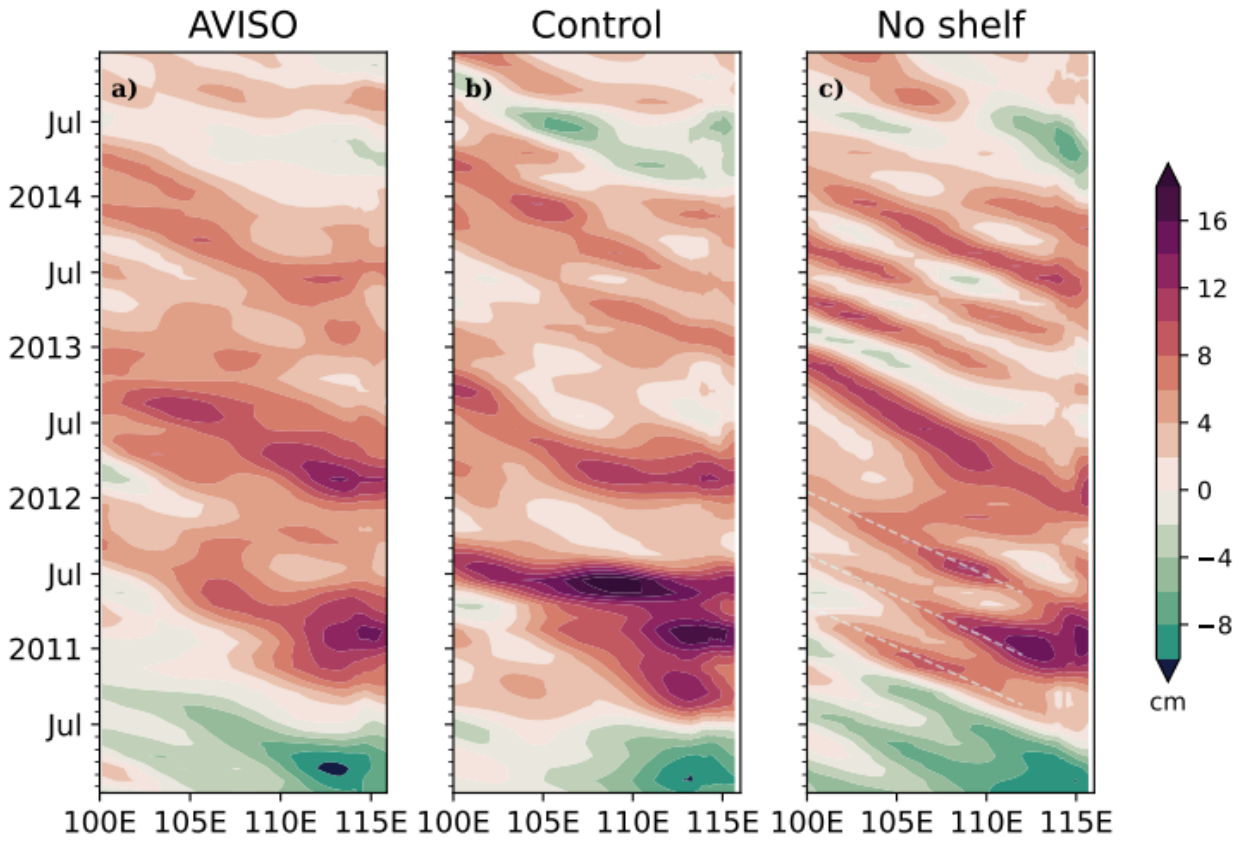

Figure 4.14. Hovmöller diagram for SSH anomalies (cm) averaged over 22°-32°S from (a)AVISO, (b) *control*, and (c) *no-shelf* experiment. White dashed lines are estimates for a zonal phase speed of 5.6 cm s^{-1}.

To further quantify to what extent the topography near the west coast of Australia can effectively trap the Rossby wave energy at the coast, the standard deviation of SSH anomalies for the period from 2010 to 2014 is calculated (Figure 4.15). The spatial pattern of the standard deviation in the *control* experiment agrees with observations reasonably well, although the magnitude is somewhat larger than the observation. While strong SSH variability near the coast rapidly weakens towards the open ocean in both the observation and the *control* experiment, it is much weaker in the nearshore region and stronger in the offshore region in the *no-shelf*

experiment. The results further confirm the essential role of the continental shelf-slope in maintaining the coastal ocean variability by suppressing the radiation of Rossby waves.

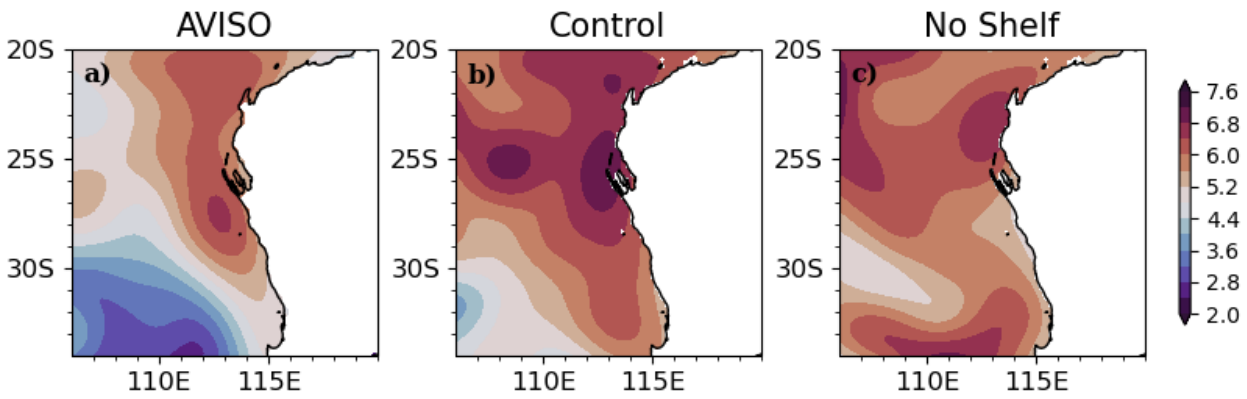

Figure 4.15. The standard deviation of the low pass filtered SSH anomalies (cm) from (a) AVISO, (b) *control* (c) *no-shelf* experiment.

4.4 Summary and Discussion

Previous theoretical studies based on idealized model experiments suggest that the presence of continental shelf-slope along the west coast of Australia plays a key role in generating a realistic LC. Using high-resolution Indo-Pacific basin OGCM experiments, this study investigates the effect of the topography on the LC and Ningaloo Niño. Two model experiments are designed to isolate the impact of continental shelf-slope on the generation and strengthening of the LC. The *control* experiment uses realistic bottom topography, and the sensitivity experiment (*no-shelf* experiment) employs a modified topography in which the flat bottom (and thus no continental shelf and slope) is used near the coast.

The mean and variability of the LC are realistically simulated in the *control* experiment. While the vertical extent of the LC simulated by the *no-shelf* experiment is realistic, the

magnitude and location are notably different from those in the *control* experiment. The composite of the LC between 22°-34ºS indicates that the core velocity in the *no-shelf* experiment is reduced by 28% on average over this latitudinal range. The reduction varies substantially with latitude, and the LC in the *no-shelf* experiment is about 40% weaker in the southern part around 34ºS. Furthermore, the LC is located closer to the coast when the shelf-slope topography is absent. The comparison of the two experiments suggests that the continental shelf-slope is an essential part of the LC dynamics as the topographic beta provides a trapping mechanism of the LC by suppressing the Rossby wave radiation from the coast, which is consistent with previous theoretical studies (Furue et al. 2013; Benthuysen et al. 2014b).

The significant influence of continental shelf-slope on LC variability is also evident during the 2010-2011 Ningaloo Niño, which is associated with the surge of the LC. During this event, the enhancement of the LC begins in mid-2010, and peaks around September 2010 and February 2011, which is simulated well in the *control* experiment. In contrast, the enhancement of the LC is much weaker in the *no-shelf* experiment especially after July 2010, and the anomalous southward current is substantially weaker during August-October 2010 and January-February 2011 due to the absence of continental shelf and slope.

The surface warming in the *control* and *no-shelf* experiments also shows large differences during these two periods. The SST anomaly in the *control* experiment is about 0.5 °C and 0.3 °C warmer than the *no-shelf* experiment in October 2010 and February 2011. The upper ocean heat budget analysis confirms that the temperature difference between the two experiments is primarily caused by the horizontal heat advection. A stronger LC is generated in the *control* experiment due to the sloping bottom topography, resulting in larger meridional heat advection.

The upper 50 m ocean temperature in the *control* experiment is 26% warmer than the *no-shelf* experiment during September 2010 - March 2011.

Ocean dynamical processes during the 2010-2011 Ningaloo Niño event are further examined by the analysis of SSH variations in the two experiments. The SSH evolution along the west coast of Australia during the event is realistically simulated in the *control* experiment. In the developing period from July to October 2010, the positive SSH anomalies along the west coast are associated with the propagation of remotely forced coastal trapped waves. At the peak phase, the SSH anomalies are further amplified by the Ekman convergence generated by anomalous northerly winds. Then the SSH anomalies are extended to the southern coast through the propagation of coastal trapped waves. The presence of the continental shelf-slope allows the SSH fluctuations to be trapped at the coast, and thus the positive SSH anomalies associated with the strong LC are sustained for a longer period. In contrast, positive SSH anomalies along the coast are much smaller in the *no-shelf* experiment because of the offshore radiation of Rossby waves from the coast. As a result, the anomalous LC in the *no-shelf* experiment is much weaker during most of the periods in the 2010-2011 Ningaloo Niño.

This study demonstrates the important role of the continental shelf-slope in strengthening and trapping the LC and in the development of Ningaloo Niño. Since coarse-resolution ocean models generally underestimate the LC due to the inability to resolve its narrow width, they often underestimate the surface warming during the Ningaloo Niño (Doi et al. 2013; Zhang et al. 2018). The simulation of LC is substantially improved by the use of high-resolution ocean models (Furue 2019). While this is partly because models can resolve the narrow LC, mesoscale eddies, and bottom topography in key regions such as the Indonesian archipelago, this study suggests that the better representation of the bottom topography near the west coast of Australia

in models is partly responsible for the realistic LC simulation. Hence the accurate representation of the continental shelf-slope near Western Australia is crucial for reducing the model's bias and for the prediction of major Ningaloo Niño such as the 2010-2011 event, during which the LC enhancement plays a dominant role. Although the importance of the strengthening of LC by bottom topography for the development of the 2010-2011 Ningaloo Niño is demonstrated in this study, it is likely that the effect largely depends on the event as processes that control the SST warming vary substantially from event to event (e.g., Marshall et al. 2015, Zhang et al. 2018). Careful evaluation and examination of ocean dynamical processes including the role of topographic trapping of LC in other Ningaloo Niño events are necessary for further improvement of simulation and prediction of LC and Ningaloo Niño.

CHAPTER V: CONCLUSION

Previous studies have investigated the processes responsible for the warm SST anomalies associated with the Ningaloo Niño extensively in recent years. The key processes such as the anomalous air-sea fluxes and enhanced Leeuwin Current heat transport have been identified as major contributions to the generation of the Ningaloo Niño. However, the relative importance of air-sea fluxes and heat advection caused by anomalous Leeuwin Current on the Ningaloo Niño development is still not well understood. Hence, questions about the role of air-sea heat flux and oceanic processes in the evolution of the Ningaloo Niño remain unclear and need to be better addressed. This dissertation aims to answer some of the major questions about the air-sea flux variability in the southeast Indian Ocean, the Leeuwin Current simulation, and the Leeuwin Current dynamics relevant to Ningaloo Nino.

Chapter 2 investigates air-sea flux variability associated with the Ningaloo Niño using multiple datasets of surface fluxes. The climatological net surface heat flux off the west coast of Australia from six major air-sea flux products shows large uncertainties, which exceeds 80 W m^{-2}, especially in the austral summer when the Ningaloo Niño develops. These uncertainties stem mainly from those in shortwave radiation and latent heat flux. The use of different bulk flux algorithms and uncertainties of bulk atmospheric variables (wind speed and air specific humidity) are mostly responsible for the difference in latent heat flux climatology between the datasets. The composite evolution of air-sea heat fluxes over the life cycle of Ningaloo Niño indicates that the anomalous latent heat flux is dominant for the net surface heat flux variations and that the uncertainties in latent heat flux anomaly largely depend on the phase of the Ningaloo Niño. During the recovery period of Ningaloo Niño, large negative latent heat flux anomalies (cooling the ocean) are evident in all datasets and thus significantly contribute to the SST

cooling. Because the recovery of winds occurs earlier than SST, high SST and strong winds favor large evaporative cooling during the recovery phase. In contrast, the role of latent heat flux during the developing phase is not clear, because the sign of the anomalies depends on the datasets in this period. The use of high-resolution SST data, which can adequately represent SST variations produced by the anomalous Leeuwin Current, could largely reduce the errors in latent heat flux anomalies during the onset and peak phases.

Chapter 3 is dedicated to understanding the impact of ocean model resolution on the simulated Leeuwin Current. Two OGCM experiments with different horizontal resolutions are conducted. The analysis of model outputs indicates that increasing model resolution from eddy-permitting (1/4°) to eddy-resolving (1/12°) could affect the Leeuwin Current substantially. Firstly, the Leeuwin Current is much stronger in the eddy-resolving experiment (EXP-H) for both the annual and seasonal mean. The enhancement of the Leeuwin Current is evident in the entire latitudinal range between 22° and 34°S, and at around 34°S the core speed of the Leeuwin Current is almost twice as strong as that simulated in the low-resolution experiment (EXP-L). Secondly, the width of the Leeuwin current is better represented in the high-resolution model. The increase in resolution also improves the zonal structures of the Leeuwin Current which intensified near the shelf break. Moreover, the colder shelf waters are simulated well in the EXP-H but not in EXP-L. Lastly, the increase in the horizontal resolution could lead to a substantial increase in the magnitude of the meridional velocity anomaly during the 2010-2011 Ningaloo Niño. The LC variability further influences the development of upper ocean warming, and the strong LC in EXP-H could lead to an increase in upper ocean temperature by up to 40%. Accordingly, results from these model simulations provide valuable information on choosing an

optimal horizontal resolution for the standalone ocean model or ocean component of the climate model for the representation of the Leeuwin Current and thus the Ningaloo Niño prediction.

In Chapter 4, the effect of the continental shelf and slope on the Leeuwin Current is quantified and the physical and dynamical processes which lead to the Leeuwin Current enhancement during the Ningaloo Niño are identified. Two high-resolution (1/12°) OGCM experiments with different bottom topographies are performed to isolate and quantify the effect of the continental shelf and slope on the Leeuwin Current and Ningaloo Niño. The "*control*" experiment uses a realistic bottom topography along the west coast of Australia, whereas the sensitivity ("*no-shelf*") experiment uses a modified topography with no continental shelf and slope near the coast. The mean and variability of Leeuwin Current are realistically simulated in the *control* experiment. The Leeuwin Current in the *no-shelf* experiment is located closer to the coast, and the strength is decreased by about 28% compared to the control experiment. The continental shelf influences the development of the 2010-2011 Ningaloo Niño through modulating the Leeuwin Current variability. In August-October 2010 and January-February 2011, the Leeuwin Current in the *control* experiment is enhanced much more than that in the *no-shelf* experiment. As a result, the upper 50 m ocean in the control experiment is about 26% warmer than the *no-shelf* experiment from September 2010 to March 2011. Different evolution of SST warming is also found in the two experiments. Comparisons of oceanic processes in the two experiments show that the shelf-slope topography can effectively trap the positive sea level anomaly at the coast in the *control* experiment while more Rossby waves radiate from the coast in the *no-shelf* experiment, resulting in a weaker Leeuwin Current.

The results of this study contribute to an improved understanding of the Leeuwin Current dynamics and generation mechanisms of Ningaloo Niño. Since climate variability at the low

latitudes such as Indian Ocean Dipole (IOD) and Madden-Julian Oscillation (MJO) could influence the Southern Indian Ocean, understanding the impact of these climate variabilities on the generation, frequency, and strength of Ningaloo Niño is one of the goals of future researches. In recent years, there are significant progress in understanding the interaction between the climate variabilities in the Pacific Ocean and Ningaloo Niño, including ENSO and Interdecadal Pacific Oscillation (IPO), and thus the improved understanding of key processes in the Southern Indian Ocean is important for providing reliable global climate projections.

REFERENCES

Balmaseda MA, Mogensen K, Weaver AT (2013) Evaluation of the ECMWF ocean reanalysis system ORAS4. Q J R Meteorol Soc 139:1132–1161. https://doi.org/https://doi.org/10.1002/qj.2063

Banzon V, Smith TM, Chin TM, et al (2016) A long-term record of blended satellite and in situ sea-surface temperature for climate monitoring, modeling and environmental studies. Earth Syst Sci Data 8:165–176. https://doi.org/10.5194/essd-8-165-2016

Benthuysen J, Feng M, Zhong L (2014a) Spatial patterns of warming off Western Australia during the 2011 Ningaloo Niño: Quantifying impacts of remote and local forcing. Cont Shelf Res 91:232–246. https://doi.org/10.1016/j.csr.2014.09.014

Benthuysen J, Furue R, McCreary JPJ, et al (2014b) Dynamics of the Leeuwin Current: Part 2. Impacts of mixing, friction, and advection on a buoyancy-driven eastern boundary current over a shelf. Dyn Atmos Ocean 65:39–63. https://doi.org/10.1016/j.dynatmoce.2013.10.004

Bleck R (2002) An oceanic general circulation model framed in hybrid isopycnic-Cartesian coordinates. Ocean Model 4:55–88. https://doi.org/10.1016/S1463-5003(01)00012-9

Brink K (1991) Coastal-Trapped Waves And Wind-Driven Currents Over The Continental Shelf. Annu Rev Fluid Mech 23:389–412. https://doi.org/10.1146/annurev.fluid.23.1.389

Brunke MA, Zeng X, Anderson S (2002) Uncertainties in sea surface turbulent flux algorithms and data sets. J Geophys Res 107:. https://doi.org/10.1029/2001JC000992

Caputi N, Gary J, Pearce A (2014) The marine heat wave off Western Australia during the summer of 2010/11 – 2 years on. Fisheries Research Report No. 250. Department of Fisheries, Western Australia. 40pp

Carton JA, Chepurin GA, Chen L (2018) SODA3: A New Ocean Climate Reanalysis. J Clim

31:6967–6983. https://doi.org/10.1175/JCLI-D-18-0149.1

Chelton DB, Schlax MG (1996) Global observations of oceanic Rossby Waves. Science (80-) 272:234–238. https://doi.org/10.13053/CyS-18-3-2043

Chin TM, Vazquez-Cuervo J, Armstrong EM (2017) A multi-scale high-resolution analysis of global sea surface temperature. Remote Sens Environ 200:154–169. https://doi.org/https://doi.org/10.1016/j.rse.2017.07.029

Cresswell GR, Golding TJ (1980) Observations of a south-flowing current in the southeastern Indian Ocean. Deep Sea Res Part A, Oceanogr Res Pap 27:449–466. https://doi.org/10.1016/0198-0149(80)90055-2

Dee DP, Uppala SM, Simmons AJ, et al (2011) The ERA-Interim reanalysis: configuration and performance of the data assimilation system. Q J R Meteorol Soc 137:553–597. https://doi.org/10.1002/qj.828

Delman AS, Lee T, Qiu B (2018) Interannual to Multidecadal Forcing of Mesoscale Eddy Kinetic Energy in the Subtropical Southern Indian Ocean. J Geophys Res Ocean 123:8180–8202. https://doi.org/10.1029/2018JC013945

Deremble B, Wienders N, Dewar WK (2013) Cheapaml: A simple, atmospheric boundary layer model for use in ocean-only model calculations. Mon Weather Rev 141:809–821. https://doi.org/10.1175/MWR-D-11-00254.1

Doi T, Behera SK, Yamagata T (2013) Predictability of the Ningaloo Nino/Nina. Sci Rep 3:. https://doi.org/10.1038/srep02892

Domingues CM, Maltrud ME, Wijffels SE, et al (2007) Simulated Lagrangian pathways between the Leeuwin Current System and the upper-ocean circulation of the southeast Indian Ocean. Deep Res Part II Top Stud Oceanogr 54:797–817.

https://doi.org/10.1016/j.dsr2.2006.10.003

Fairall CW, Bradley EF, Hare JE, et al (2003) Bulk Parameterization of Air–Sea Fluxes: Updates and Verification for the COARE Algorithm. J Clim 16:571–591. https://doi.org/10.1175/1520-0442(2003)016<0571:BPOASF>2.0.CO;2

Feng M, Biastoch A, Boning C, et al (2008) Seasonal and interannual variations of upper ocean heat balance off the west coast of Australia. J Geophys Res 113:C12025. https://doi.org/10.1029/2008JC004908

Feng M, Hendon HH, Xie SP, et al (2015) Decadal increase in Ningaloo Niño since the late 1990s. Geophys Res Lett 42:104–112. https://doi.org/10.1002/2014GL062509

Feng M, McPhaden MJ, Xie S-P, Hafner J (2013) La Niña forces unprecedented Leeuwin Current warming in 2011. Sci Rep 3:1–9. https://doi.org/10.1038/srep01277

Feng M, Meyers G, Pearce A, Wijffels S (2003) Annual and interannual variations of the Leeuwin Current at 32°S. J Geophys Res 108:3355. https://doi.org/10.1029/2002JC001763

Feng M, Wijffels S, Godfrey S, Meyers G (2005) Do eddies play a role in the momentum balance of the Leeuwin Current? J Phys Oceanogr 35:964–975. https://doi.org/10.1175/JPO2730.1

Feng X, Shinoda T (2019) Air-Sea Heat Flux Variability in the Southeast Indian Ocean and Its Relation With Ningaloo Niño. Front Mar Sci 6:266. https://doi.org/10.3389/fmars.2019.00266

Forget G, Campin JM, Heimbach P, et al (2015) ECCO version 4: An integrated framework for non-linear inverse modeling and global ocean state estimation. Geosci Model Dev 8:3071–3104. https://doi.org/10.5194/GMD-8-3071-2015

Furue R (2019) The three-dimensional structure of the Leeuwin Current System in density

coordinates in an eddy-resolving OGCM. Ocean Model 138:36–50. https://doi.org/10.1016/J.OCEMOD.2019.03.001

Furue R, Guerreiro K, Phillips HE, et al (2017) On the Leeuwin Current System and Its Linkage to Zonal Flows in the South Indian Ocean as Inferred from a Gridded Hydrography. J Phys Oceanogr 47:583–602. https://doi.org/10.1175/JPO-D-16-0170.1

Furue R, McCreary JP, Benthuysen J, et al (2013) Dynamics of the Leeuwin Current: Part 1. Coastal flows in an inviscid, variable-density, layer model. Dyn Atmos Ocean 63:24–59. https://doi.org/10.1016/j.dynatmoce.2013.03.003

Gelaro R, McCarty W, Suárez MJ, et al (2017) The Modern-Era Retrospective Analysis for Research and Applications, Version 2 (MERRA-2). J Clim 30:5419–5454. https://doi.org/10.1175/JCLI-D-16-0758.1

Godfrey JS, Ridgway KR (1985) The Large-Scale Environment of the Poleward-Flowing Leeuwin Current, Western Australia: Longshore Steric Height Gradients, Wind Stresses and Geostrophic Flow. J Phys Oceanogr 15:481–495. https://doi.org/10.1175/1520-0485(1985)015<0481:TLSEOT>2.0.CO;2

Godfrey JS, Weaver AJ (1991) Is the Leeuwin Current driven by Pacific heating and winds? Prog Oceanogr 27:225–272. https://doi.org/10.1016/0079-6611(91)90026-I

Han W, Vialard J, McPhaden MJ, et al (2014) Indian ocean decadal variability: A review. Bull Am Meteorol Soc 95:1679–1703. https://doi.org/10.1175/BAMS-D-13-00028.1

Hersbach, H., and Coauthors (2018) ERA5 hourly data on single levels from 1979 to present. Copernicus Climate Change Service (C3S) Climate Data Store (CDS). (Accessed on 20-JUL-2019), 10.24381/cds.adbb2d47

Huang Z, Feng M (2015) Remotely sensed spatial and temporal variability of the Leeuwin

Current using MODIS data. Remote Sens Environ 166:214–232. https://doi.org/10.1016/j.rse.2015.05.028

Huthnance JM (1978) On coastal trapped waves: analysis and numerical calculation by inverse iteration. J Phys Oceanogr 8:74–92. https://doi.org/10.1175/1520-0485(1978)008<0074:octwaa>2.0.co;2

Kalnay E, Kanamitsu M, Kistler R, et al (1996) The NCEP/NCAR 40-Year Reanalysis Project. Bull Am Meteorol Soc 77:437–472. https://doi.org/10.1175/1520-0477(1996)077<0437:TNYRP>2.0.CO;2

Kanamitsu M, Ebisuzaki W, Woollen J, et al (2002) NCEP–DOE AMIP-II Reanalysis (R-2). Bull Am Meteorol Soc 83:1631–1644. https://doi.org/10.1175/BAMS-83-11-1631

Kataoka T, Masson S, Izumo T, et al (2018) Can Ningaloo Niño/Niña Develop Without El Niño–Southern Oscillation? Geophys Res Lett 45:7040–7048. https://doi.org/10.1029/2018GL078188

Kataoka T, Tozuka T, Behera S, Yamagata T (2014) On the Ningaloo Niño/Niña. Clim Dyn 43:1463–1482. https://doi.org/10.1007/s00382-013-1961-z

Kataoka T, Tozuka T, Yamagata T (2017) Generation and Decay Mechanisms of Ningaloo Niño/Niña. J Geophys Res Ocean 122:8913–8932. https://doi.org/10.1002/2017JC012966

Kato S, Rose FG, Rutan DA, et al (2018) Surface Irradiances of Edition 4.0 Clouds and the Earth's Radiant Energy System (CERES) Energy Balanced and Filled (EBAF) Data Product. J Clim 31:4501–4527. https://doi.org/10.1175/JCLI-D-17-0523.1

Kubota M, Iwabe N, Cronin MF, Tomita H (2008) Surface heat fluxes from the NCEP/NCAR and NCEP/DOE reanalyses at the Kuroshio Extension Observatory buoy site. J Geophys Res Ocean 113:1–14. https://doi.org/10.1029/2007JC004338

Kundu PK, McCreary JPJ (1986) On the Dynamics of the Throughflow from the Pacific into the Indian Ocean. J Phys Oceanogr 16:2191–2198. https://doi.org/10.1175/1520-0485(1986)016<2191:OTDOTT>2.0.CO;2

Kusunoki H, Kido S, Tozuka T (2020) Contribution of oceanic wave propagation from the tropical Pacific to asymmetry of the Ningaloo Niño/Niña. Clim Dyn. https://doi.org/10.1007/s00382-020-05268-5

Large WG, McWilliams JC, Doney SC (1994) Oceanic vertical mixing: A review and a model with a nonlocal boundary layer parameterization. Rev Geophys 32:363–403. https://doi.org/https://doi.org/10.1029/94RG01872

Large WG, Yeager S (2004) Diurnal to decadal global forcing for ocean and sea-ice models: the data sets and flux climatologies. NCAR Tech Note TN--460+ST:

Marshall AG, Hendon HH, Feng M, Schiller A (2015) Initiation and amplification of the Ningaloo Niño. Clim Dyn 45:2367–2385. https://doi.org/10.1007/s00382-015-2477-5

McCreary JPJ, Shetye SR, Kundu PK (1986) Thermohaline forcing of eastern boundary currents: With application to the circulation off the west coast of Australia. J Mar Res 44:71–92. https://doi.org/10.1357/002224086788460184

McPhaden MJ, Meyers G, Ando K, et al (2009) RAMA: The research moored array for African-Asian-Australian monsoon analysis and prediction. Bull Am Meteorol Soc. https://doi.org/10.1175/2008BAMS2608.1

Menezes V V., Phillips HE, Schiller A, et al (2014) South Indian Countercurrent and associated fronts. J Geophys Res Ocean 119:6763–6791. https://doi.org/10.1002/2014JC010076

Metzger EJ, Hurlburt HE, Xu X, et al (2010) Simulated and observed circulation in the Indonesian Seas: 1/12° global HYCOM and the INSTANT observations. Dyn Atmos Ocean

50:275–300. https://doi.org/https://doi.org/10.1016/j.dynatmoce.2010.04.002

Metzger JE, Smedstad OM, Thoppil PG, et al (2014) Us navy operational global ocean and arctic ice prediction systems. Oceanography 27:32–43. https://doi.org/10.5670/OCEANOG.2014.66

Morrow R, Birol F, Griffin D, Sudre J (2004) Divergent pathways of cyclonic and anti-cyclonic ocean eddies. Geophys Res Lett 31:L24311. https://doi.org/10.1029/2004GL020974

Nicholls N (1979) A simple air-sea interaction model. Q J R Meteorol Soc 105:93–105. https://doi.org/10.1002/qj.49710544307

Pearce A, Lenanton RCJ, Jackson G, et al (2011) The "marine heat wave" off Western Australia during the summer of 2010/11. Fisheries Research Report No. 222. Department of Fisheries, Western Australia

Pearce AF, Feng M (2013) The rise and fall of the "marine heat wave" off Western Australia during the summer of 2010/2011. J Mar Syst 111–112:139–156. https://doi.org/10.1016/j.jmarsys.2012.10.009

Reynolds RW, Smith TM, Liu C, et al (2007) Daily High-Resolution-Blended Analyses for Sea Surface Temperature. J Clim 20:5473–5496. https://doi.org/10.1175/2007JCLI1824.1

Ridgway KR, Condie SA (2004) The 5500-km-long boundary flow off western and southern Australia. J Geophys Res Ocean 109:. https://doi.org/10.1029/2003JC001921

Ridgway KR, Dunn JR, Wilkin JL (2002) Ocean Interpolation by Four-Dimensional Weighted Least Squares—Application to the Waters around Australasia. J Atmos Ocean Technol 19:1357–1375. https://doi.org/10.1175/1520-0426(2002)019<1357:OIBFDW>2.0.CO;2

Ridgway KR, Godfrey JS (2015) The source of the Leeuwin Current seasonality. J Geophys Res Ocean 120:6843–6864. https://doi.org/10.1002/2015JC010969

Saha S, Moorthi S, Pan H-L, et al (2010) The NCEP Climate Forecast System Reanalysis. Bull Am Meteorol Soc 91:1015–1058. https://doi.org/10.1175/2010BAMS3001.1

Saha S, Moorthi S, Wu X, et al (2014) The NCEP Climate Forecast System Version 2. J Clim 27:2185–2208. https://doi.org/10.1175/JCLI-D-12-00823.1

Seager R, Blumenthal MB, Kushnir Y (1995) An Advective Atmospheric Mixed Layer Model for Ocean Modeling Purposes: Global Simulation of Surface Heat Fluxes. J Clim 8:1951–1964

Shinoda T, Lin J (2009) Interannual Variability of the Upper Ocean in the Southeast Pacific Stratus Cloud Region. J Clim 22:5072–5088. https://doi.org/10.1175/2009JCLI2696.1

Smith RL, Huyer A, Godfrey JS, Church J a. (1991) The Leeuwin Current off Western Australia, 1986–1987. J. Phys. Oceanogr. 21:323–345

Steele M, Morley R, Ermold W (2001) PHC: A Global Ocean Hydrography with a High-Quality Arctic Ocean. J Clim 14:2079–2087. https://doi.org/10.1175/1520-0442(2001)014<2079:PAGOHW>2.0.CO;2

Thompson R (1984) Observations of the Leeuwin Current off Western Australia. J Phys Oceanogr 14:623–628. https://doi.org/10.1175/1520-0485(1984)014<0623:OOTLCO>2.0.CO;2

Tozuka T, Kataoka T, Yamagata T (2014) Locally and remotely forced atmospheric circulation anomalies of Ningaloo Niño/Niña. Clim Dyn 43:2197–2205. https://doi.org/10.1007/s00382-013-2044-x

Tozuka T, Oettli P (2018) Asymmetric Cloud-Shortwave Radiation-Sea Surface Temperature Feedback of Ningaloo Niño/Niña. Geophys Res Lett 45:9870–9879. https://doi.org/10.1029/2018GL079869

Valdivieso M, Haines K, Balmaseda M, et al (2017) An assessment of air–sea heat fluxes from ocean and coupled reanalyses. Clim Dyn 49:983–1008. https://doi.org/10.1007/s00382-015-2843-3

Waliser DE, Graham NE (1993) Convective cloud systems and warm-pool sea surface temperatures: Coupled interactions and self-regulation. J Geophys Res 98:12881–12893. https://doi.org/https://doi.org/10.1029/93JD00872

Wang D, Mooers CNK (1976) Coastal-trapped waves in a continuously stratified ocean. 6:853–863

Weatherall P, Marks KM, Jakobsson M, et al (2015) A new digital bathymetric model of the world's oceans. Earth Sp Sci 2:331–345. https://doi.org/10.1002/2015EA000107

Weaver AJ, Middleton JH (1989) On the Dynamics of the Leeuwin Current. J Phys Oceanogr 19:626–648. https://doi.org/10.1175/1520-0485(1989)019<0626:OTDOTL>2.0.CO;2

Weaver AJ, Middleton JH (1990) An analytic model for the Leeuwin Current off western Australia. Cont Shelf Res 10:105–122. https://doi.org/10.1016/0278-4343(90)90025-H

Wernberg T, Smale DA, Tuya F, et al (2013) An extreme climatic event alters marine ecosystem structure in a global biodiversity hotspot. Nat Clim Chang 3:78–82. https://doi.org/10.1038/nclimate1627

Wu R, Kirtman BP, Pegion K (2006) Local air-sea relationship in observations and model simulations. J Clim 19:4914–4932. https://doi.org/10.1175/JCLI3904.1

Xu J, Lowe RJ, Ivey GN, et al (2018) Contrasting Heat Budget Dynamics During Two La Niña Marine Heat Wave Events Along Northwestern Australia. J Geophys Res Ocean 123:1563–1581. https://doi.org/10.1002/2017JC013426

Yu L, Jin X, Weller RA (2008) Multidecade Global Flux Datasets from the Objectively

Analyzed Air-sea Fluxes (OAFlux) Project: Latent and sensible heat fluxes, ocean evaporation, and related surface meteorological variables. Woods Hole. Massachusetts.

Zeng X, Zhao M, Dickinson R (1998) Intercomparison of bulk aerodynamic for the computation of sea surface fluxes using TOGA COARSE and TAO data. J Clim 11:2628–2644

Zhang D, Cronin MF, Wen C, et al (2016) Assessing surface heat fluxes in atmospheric reanalyses with a decade of data from the NOAA Kuroshio Extension Observatory. J Geophys Res Ocean 121:6874–6890. https://doi.org/10.1002/2016JC011905

Zhang L, Han W (2018) Impact of Ningaloo Niño on Tropical Pacific and an Interbasin Coupling Mechanism. Geophys Res Lett 45:11300–11309. https://doi.org/10.1029/2018GL078579

Zhang L, Han W, Li Y, Shinoda T (2018) Mechanisms for Generation and Development of Ningaloo Niño. J Clim 31:9239–9259. https://doi.org/10.1175/JCLI-D-18-0175.1

Zinke J, Hoell A, Lough JM, et al (2015) Coral record of southeast Indian Ocean marine heatwaves with intensified Western Pacific temperature gradient. Nat Commun 6:. https://doi.org/10.1038/ncomms9562

APPENDIX

UNCERTAINTY OF LATENT HEAT FLUX CAUSED BY BULK FLUX ALGORITHM AND ITS SEASONALITY

The bulk flux algorithm calculates latent heat flux by using the mean value of bulk state variables (Yu et al. 2008):

$$Q_{LH} = \rho L C_e U(q_s - q_a)$$

where ρ is the density of air, L is the latent heat of vaporization, $C_e$is the transfer coefficient for moisture, U is surface wind speed relative to surface current, q_s is sea surface saturated specific humidity estimated from SST and q_a is air specific humidity. The direction of the latent heat flux calculated with this equation is from the ocean to the atmosphere for the positive values. While latent heat flux is directly proportional to wind speed and humidity gradient, the transfer coefficient for moisture, which represents the physical processes involved in the heat transfer at the air-sea interface, can change with wind speed and atmosphere stability. The transfer coefficient is calculated differently in different algorithms.

Figure A1 shows the uncertainties of latent heat flux caused by the algorithms used in reanalysis products. While latent heat flux based on the algorithm in NCEP1 and NCEP2 have a larger difference compared to that from COARE3.5, CFSR and ERA-Interim indicate a better agreement with COARE3.5. The uncertainties also depend on the magnitude of latent heat flux and larger latent heat flux usually has larger uncertainties. However, results from NCEP1 and CFSR show the uncertainty is larger in summer than in winter, although latent heat flux is higher in winter. This difference between summer and winter is likely due to the difference in wind speed. Zeng et al. (1998) showed that the neutral exchange coefficient for latent heat flux from different algorithms diverges at higher wind speed. During summer, winds are stronger although

the latent heat flux is relatively smaller. The wind effect on the transfer coefficient is likely to account for the larger uncertainty during summer.

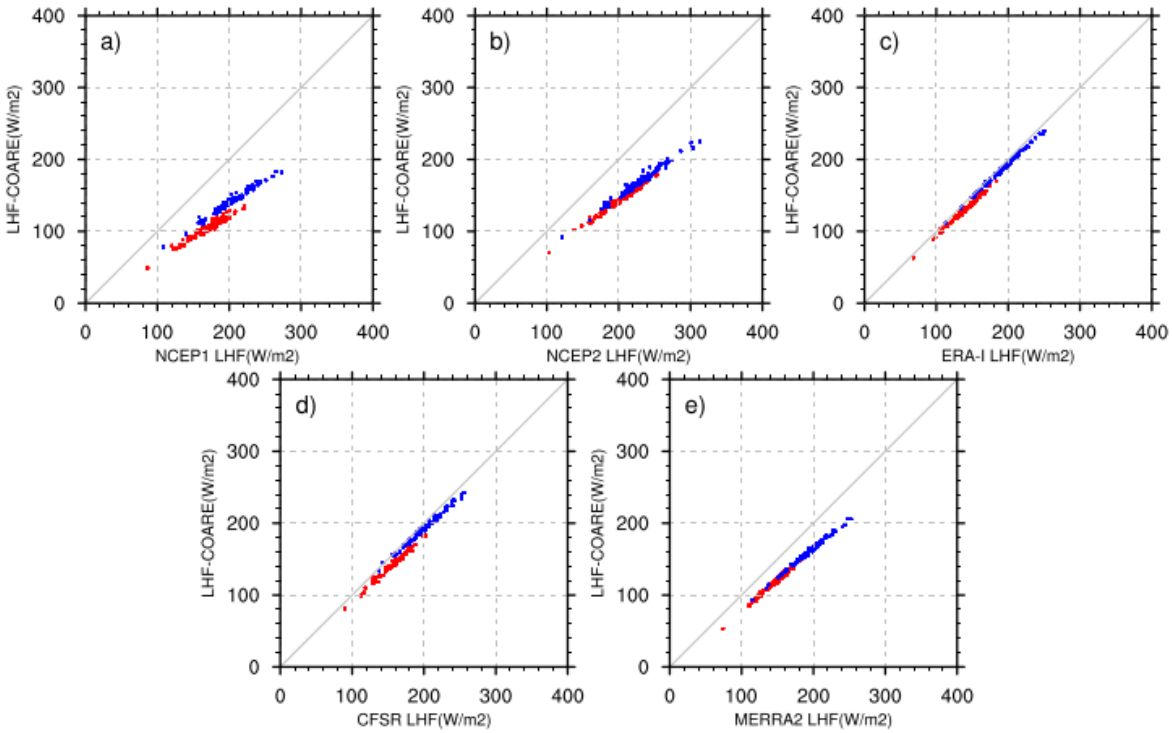

Figure A1. Comparisons of monthly latent heat fluxes (LHF) from EX-alg (vertical axis) with those (horizontal axis) obtained from (a) NCEP1, (b) NCEP2, (c) ERA-Interim, (d) CFSR, and (f) MERRA2. JJA (DJF) data points are shown in blue (red).

SUPPLEMENTARY MATERIAL

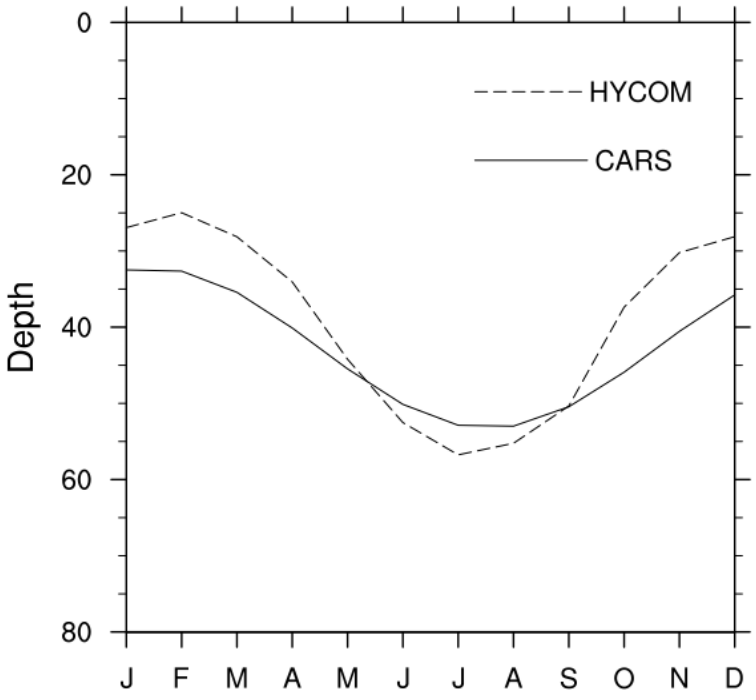

Figure S1**.** Climatological monthly MLD from the HYCOM reanalysis and the CSIRO Atlas of Regional Seas (CARS)-2009 (Ridgway et al. 2002) over the region (110°E-116°E, 22°S-32°S).